THE EFFECTS OF THE EARTH'S MAGNETIC FIELD ON CHEREKOV LIGHT IMAGE PARAMETERS

by

Jose Osmaro Cardoza

A thesis submitted to the faculty of
The University of Utah
in partial fulfillment of the requirements for the degree of

Master of Science

in

Physics

Department of Physics and Astronomy

The University of Utah

August 2012

THE UNIVERSITY OF UTAH GRADUATE SCHOOL

STATEMENT OF THESIS APPROVAL

The thesis of **Jose Osmaro Cardoza**
has been approved by the following supervisory committee members:

David Kieda , Chair		**04/20/2012**
		Date Approved
Stephan LeBohec , Member		**04/27/2012**
		Date Approved
Christoph Boehme , Member		**04/27/2012**
		Date Approved

and by **David Kieda** , Chair of

the Department of **Physics and Astronomy**

and by Charles A. Wight, Dean of The Graduate School.

ABSTRACT

The Very Energetic Radiation Imaging Telescope Array System (VERITAS) detects Cerenkov radiation from extended air showers (EAS) produced by $\gamma - rays$ that interact with the earth's atmosphere. The earth's magnetic field effects the development of EAS by interacting with secondary charge particles in the shower. In this thesis, we present the results of Monte Carlo simulations of primary $\gamma - rays$ with kinetic energies between 400 GeV and 6.4 TeV and the effects that the earth's magnetic field has on the image parameters width and length. Simulation results are compared to Crab Nebula data from the 2007-2008 observation season.

I dedicate this work to my amazing mother and to my wonderful mentor VC Newton.

CONTENTS

LIST OF FIGURES

LIST OF TABLES

CHAPTER 1

INTRODUCTION

Astronomy is an old branch of science that studies cosmic objects. Astronomers gather information by collecting the electromagnetic radiation from these astrophysical objects. This task is made difficult by the lack of control of external conditions and parameters. Detailed understanding of objects is achieved by making observations over a variety of wavelengths. The development of new techniques and more sophisticated instruments have led to a new field called astro-particle physics. Astro-particle physics is a combination of astronomy and particle physics. Thus, data are collected passively, analyzed and interpreted by techniques commonly used in particle physics. In gathering this information we seek to understand the process that produced the electromagnetic radiation from the different possible systems and the nature of the spectrum corresponding to each individual system.

1.1 Cosmic Rays

Cosmic rays (CRs), energetic particles from outer space, were discovered first during manned balloon flights in 1912 by Viktor F. Hess [1]. Hess found that the averaged ionization increased with respect to height, with 1.4×10^6 ion pairs per m^3 at sea level and 16.9×10^6 ion pairs per m^3 at 5km above sea level [2]. Thus showing that the source of ionization radiation must be originating outside of the earth. We know now that cosmic rays are composed of about 98% of protons and nuclei and about 2% electrons. In addition, the nucleonic components can broken down to about 87% protons, 12% helium nuclei and about 1% heavier nuclei [2].

An interesting feature of cosmic rays is the fact that their energy spectrum spans a wide range of energies, from $\sim 10^3$ eV to more than 10^{20} eV. In this energy range the intensity drops by more than 30 orders of magnitude, Figure 1.1. Their energy spectrum is characterized by a power law $dN/dE \propto E^{-\gamma}$, where the spectral index is a function of the energy. The spectral index is about -2.7 at energies up to 4 PeV (4×10^{15}), where a steeping occurs at the "knee" and the spectral index changes to -3.1. A further steepening known as the "second knee", occurs at about 4×10^{17}eV. The spectrum then flattens out at about 4×10^{18}eV. The cosmic ray flux decreases from about
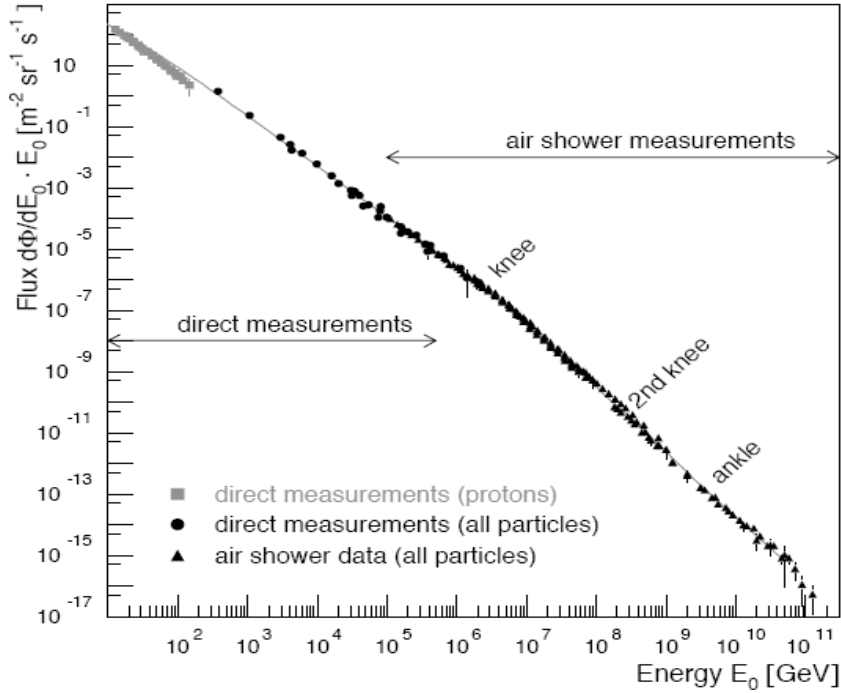
Figure 1.1: Cosmic ray spectrum obtained using both space borne and ground base detectors. [3].

1000 particles-$s^{-1}m^{-2}$ at GeV energies (10^9 eV) to about one particle per square meter and year at PeV energies [3]. This particle flux has made it difficult to investigate the origins of cosmic rays. Currently, space borne detectors and weather balloons are used to look at sub GeV energies while land based detectors with large detection areas are required to explore the TeV (10^{12}eV) and above regime.

As cosmic-ray particles propagate through space we assume interactions with intergalactic, irregular magnetic fields that cause them to appear isotropically distributed over the sky. At very high energies, energies above 10^{19}eV, where the interaction with the magnetic field becomes weak, large arrays have used charged CRs as tracers to point back to within a few degrees of their source [4], [5]. All the different experiments done have significantly increased our understanding of cosmic rays, but their origin still remains an open question.

1.2 Gamma-Rays

The electromagnetic spectrum of observed radiation spans more than 20 orders of magnitude in wavelength, ranging from the long wavelength regime of radio waves to the extremely short wavelengths of gamma-rays, see Figure 1.2. Gamma-rays are produced by non-thermal mechanisms and the study of gamma-rays was first motivated by the search for the origin of cosmic rays. The
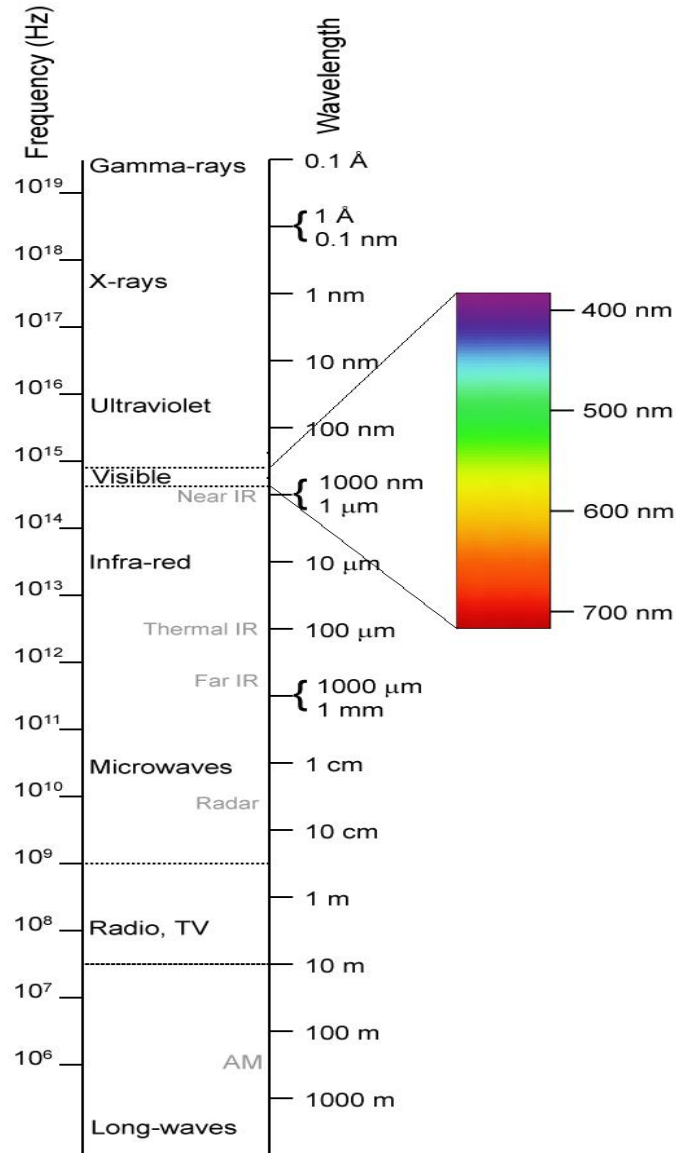
Figure 1.2: The bands of electromagnetic spectrum expressed in terms of wavelength and frequency [6].

term gamma-rays is used to describe high energy photons with energies ranging from 10^6 eV to 10^{20} eV, but theoretically there is no energy limitation for gamma-rays. This wide range of 15 orders of magnitude is more than the combined emission from all remaining wavebands and establishing the divisions and their corresponding names was challenging.

A classification scheme was developed by Weekes in 1988 based primarily on observation techniques and the interaction phenomena of gamma-rays. For example, detectors in the VHE (very high energy) regime are used to detect the cascade of particles resulting from the interaction of primary gamma-rays with the atmosphere or to collect the Cherenkov light emitted from the

relativistic charged particles. An important aspect of each regime is their production mechanism. Table 1.1 shows a more recent nomenclature introduced by Hoffman et al in 1999 with the corresponding detection techniques. This nomenclature reflects the changes in energy range over which a given detection technique is used.

Unlike cosmic rays, gamma-rays are not deflected by magnetic fields on their way to earth so they have the important feature of pointing back to their source. Due to their high energy, it is expected that powerful and intriguing sources are responsible for emitting gamma-ray photons. The discovery of new and different types of sources, existing under extreme environments where new physical laws may be required, has made gamma-ray astronomy an exciting field of study. More on the milestones, future and importance of VHE gamma-ray astronomy can be found in [8].

Table 1.1: The nomenclature used for describing the different gamma-ray regimes and various detection techniques, adopted from [7].

Energy Range [eV]	Nomenclature	Traditional detection technique
$10^7 - 3\times10^7$ 10 - 30 MeV	Medium Energy	Satellite based Compton Telescope
$3\times10^7 - 3\times10^{10}$ 30 - 30 GeV	High Energy (HE)	Satellite based Tracting detector
$3\times10^{10} - 3\times10^{13}$ 30 - 30 TeV	Very high energy (VHE)	Ground based Cherenkov or air shower detector
$3\times10^{13} - 3\times10^{16}$ 30 - 30 PeV	Ultra high energy (UHE)	Ground based Air shower detector
3×10^{16} and up 30 PeV and up	Extremely high energy (EHE)	Ground based Air shower or fluorescence detector

1.3 Gamma-Ray Production Mechanisms

In the most general sense gamma-rays can be produced through thermal and non-thermal emissions. Thermal (Blackbody) radiation can emitted by any body with a non zero temperature. The spectrum of thermal emission follows the Planck distribution function. The number of density of photons per unit energy is given by

$$n_{BB}(E_\gamma) = \frac{(E_\gamma/m_e c^2)^2}{m_e c^2 (\pi^2 \lambda_c^3)} \left[\frac{1}{\exp(E_\gamma/kT) - 1}\right] \tag{1.1}$$

The average energy of the photons can then be calculated to be $\langle E_\gamma \rangle = 2.7kT$, where k is the Boltzmann constant. Thus photons with energies of 1GeV would need temperatures of about $10^{13}K$. Such high temperatures cannot be found in steady astrophysical objects. The photon density of the 1GeV photon with a temperature $10^{13}K$ would be about 3×10^{34} cm^{-3} which would give us a self absorbed source due to photon photon pair creation. Nonthermal processes for gamma-ray sources are thus much more typical.

1.3.1 Nonthermal Gamma-ray Production Mechanisms

- *Synchrotron radiation*: When relativistic charged particles spiral in a magnetic field, it emits radiation called synchrotron radiation. This radiation is characterized by three attributes. The rotation frequency decreases as $\gamma = (1 - \frac{v}{c})^{\frac{1}{2}}$, where v is the speed of the particle. Second the radiation gets confined to a cone with an opening angle $\Delta\theta \simeq \gamma$. Finally, higher harmonics of the cyclotron frequency significantly contribute to the spectrum and tend to be closely spaced thus appearing as a continuous spectrum [9]. In such a scenario gamma-ray photons are produced only for extremely energetic particles and strong magnetic fields.

- *Curvature Radiation*: This radiation is similar to synchrotron radiation except that magnetic fields are strong *and* nonuniform.

- *Inverse Compton Scattering* : The process by which a photon is scattered by an electron and gains energy. If the electron is relativistic then the scattering of the electron on the photon can produce gamma-rays, change the original spectrum of the photon and cool the electron. Such a situation is found in relativistic plasma.

- *Bremsstrahlung Radiation*: Such radiation (also called "braking radiation") is produced when a charged particle is accelerated or decelerated by the electromagnetic field of a nucleus or other charged particle. In the case of accelerated relativistic electrons the energy of the emitted photons is similar to the energy of the relativistic electrons and gamma-rays can be emitted.

- $\pi^0 decay$: Pions can be produced from proton-proton interactions or proton-antiproton annihilation and subsequently decay to produced gamma-rays.

1.4 Gamma- Ray Sources

There are a variety of candidate sources for VHE gamma-ray emission. Source candidates include Supernova Remnants (SNR), Active Galactic Nuclei (AGN), Pulsars, binary systems, Gamma-Ray Bursts (GRBs), quasars and microquasars. Some of these are illustrated in Figure 1.3.

1.4.1 Galactic Sources

1.4.1.1 Supernova Remnants

The expanding material ejected from a supernova plus the shock wave that drives it into the interstellar medium is known as a supernova remnant (SNR). There are three types of SNRs, shell type, plerion type and composite type. Shell type SNRs are thought to be the sources of galactic cosmic rays with energies up to $\sim 10^{15}$ eV (the knee region) [10]. The plerion type contain pulsars (rapidly rotating neutron stars) whose intense magnetic fields accelerate energetic particles which collide with the stellar ejecta to produce VHE gamma-rays. Of all the known SNRs, the Crab Nebula, a plerion type, is regarded as a "standard" candle in gamma-ray astronomy and is used to calibrate VHE instruments and optimize the analysis.

1.4.1.2 Microquasars

Microquasars are binary systems containing a compact object, such as a neutron star or a stellar mass black hole, accreting matter from a companion star. They also have relativistic jets, resulting from the accretion onto the compact object, in which particles can be accelerated to extreme energies. For example, radio emission from microquasars is generally attributed to synchrotron radiation of relativistic electrons spiraling around magnetic fields in the jets [11]. Microquasars are named after quasars, since they share some common characteristics such as strong and variable radio emission, jets, and an accretion disk surrounding a compact object. Microquasars are essentially a smaller galactic version of the extragalactic quasars.

VHE gamma-rays can be produced by microquasars by inverse Compton scattering of the stellar photons with relativistic particles or by hadronic processes such as the neutral pion decay resulting from the interactions of accelerated protons with nonrelativistic ions from the stellar wind of the companion star. To date three microquasars have been detected in the VHE regime LS 5039, LS I +61 303 and Cygnus X-1 [12].
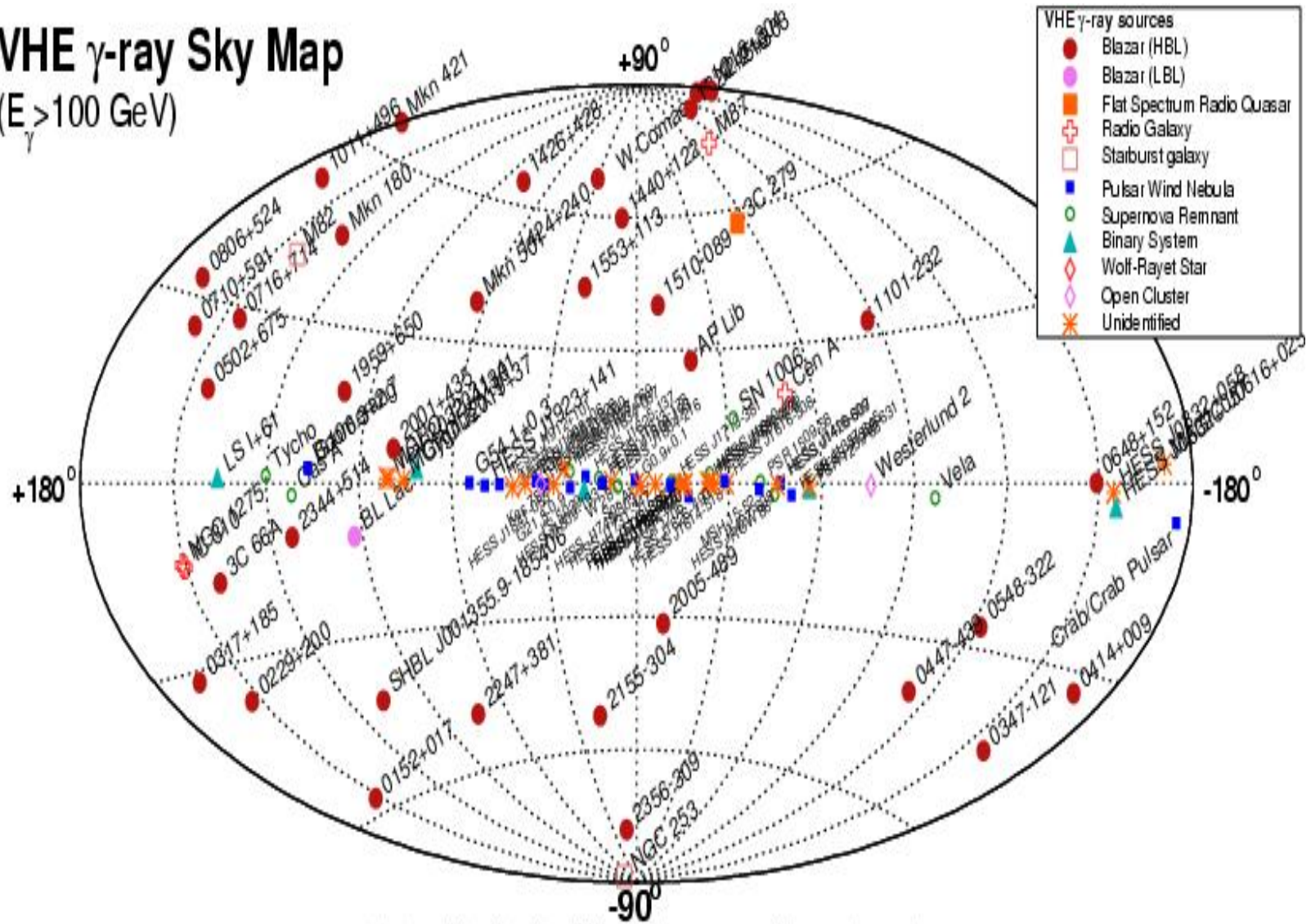
Figure 1.3: A current map of the VHE gamma-ray sky in galactic coordinates. As of 01-05-2011 there have been 46 extra galactic sources and 61 galactic sources catalogued, courtesy of [13].

1.4.2   Extragalactic Sources

1.4.2.1   Active Galactic Nuclei

Active Galactic Nuclei (AGNs) are galaxies whose emission comes largely from a bright central core believed to be harboring a super massive black hole. The total Balometric luminosity of AGNs can span about 10 orders of magnitude, from about 10^{38} $ergs/s$ to about 10^{48} $ergs/s$ which can approach 10^4 times the amount of a typical galaxy [14]. AGNs like microquasars can have relativistic jets, resulting from the accretion super massive black hole, that emanate perpendicularly away from the planes of the galaxies and are though to be responsible for accelerating particles. However, the mechanism responsible for forming the jets is not well understood. The nature of the nonthermal emission from the jets is also uncertain as it can be explain by synchrotron and inverse Compton (IC) processes as well as by hadronic models. The are several types of AGN. They exhibit a wide range of observable properties, see [14] for more details.

1.4.2.2   Gamma-Ray Bursts

Gamma-ray bursts (GRBs) are the most intense and powerful flashes of gamma-rays in the universe. They are categorized into two types depending on their duration as either long GRBs (lasting more than 2 seconds) or short GRBs (lasting fewer than 2 seconds). Long duration GRBs are thought to be produced by the core collapse of massive stars while short duration GRBs have been associated with both early and late type host galaxies. The latter of which tend to lie in star forming regions of low mass, irregular galaxies. The short duration GRBs are thought to be produced in merger events of compact binary systems, two neutron stars or a neutron star/black hole pair, and thus would tend to lie in older stellar populations [15]. Metzge et al. [16] show that many of the GRB properties can be explained by peculiar compact objects with extremely high magnetic fields called magnetstars.

CHAPTER 2

DETECTION METHODS OF VHE
GAMMA- RAYS

Both ground based and satellite based detectors can be used to detect γ-rays. For energies above $\sim 300\text{GeV}$, ground-based instruments are employed due to the low flux of γ-rays, which mandate large detection areas. VHE γ-rays are not detected directly by ground instruments since they are absorbed by the atmosphere. This is a fortunate situation, since such energetic photons are hazardous to life on earth. Instead ground-based detectors use indirect methods, such as the optical light from extended air showers (EAS) induced by γ-rays. This radiation is know as Cherenkov radiation and was discovered in 1937 by Russian scientist Pavel Alekseyevich Cherenkov. The technique of detecting Atmospheric Cherenkov light has been developed over the past 50 years. The difficulty in using the Cherenkov technique lies in efficiently distinguishing the gamma-ray signal,which makes less than 0.01% of signal, from the overwhelming noise of background cosmic rays. Such difficulty can be resolved by using the Atmospheric Cherenkov imaging technique, which we will discuss later in the chapter.

2.1   Extensive Air Showers
2.1.1   Gamma Ray Induced Air Showers

The mean free path of VHE γ-ray when they enter the Earth's atmosphere is about $37.7g/cm^2$ as they interact with atmospheric nuclei to produce an EAS. This interaction occurs about 25 km above sea level via three main processes: pair production, Bremsstrahlung, and photo production. For pair production to occur, gamma-rays have to have an energy greater than $2m_ec^2$ and a third body such as a nucleus needs to be present in order to conserve both energy and momentum. In pair production, a γ-ray encounters the Coulomb field of an atmospheric nucleus and after about one radiation length, the γ-ray is transformed into an electron-positron pair $(\gamma \to e^+ + e^-)$. The resulting electron-positron pair shares the energy of the primary γ-ray, is emitted in the forward direction and goes on to interact with atmospheric nuclei to produce more gamma-rays via Bremsstrahlung. The electron and positron lose most of their energy via Bremsstrahlung

radiation, with a small loss due to ionization. After about one radiation length lower gamma-ray photons are produced, which can also pair produce, and the process repeats itself. The shower maximum is reached when the averaged energy of the secondary particles is such that ionization losses are approximately equal to radiation losses. Once the shower maximum is passed and the critical energy is reached, the EAS will attenuate quickly through the ionization of air molecules by electrons and positrons. As a result the EAS is no longer self-propagating and dies out. Although there is a chance for muon production in γ-ray cascades through photo-nuclear interactions, the probability of this is 10^4 times that of electron/positron pair production. Thus we can conclude that γ-ray induced cascades are mainly electromagnetic in nature. An illustration of this process is shown in Figure 2.1.

2.1.2   Hadronic Showers

When a cosmic ray enters the atmosphere it can interact with the upper atmosphere and initiate an EAS similar to the one produced by γ-rays, see Figure 2.2. Despite the similarities between the two EAS production mechanisms, there are major differences between the two that enable us to differentiate one from the other.
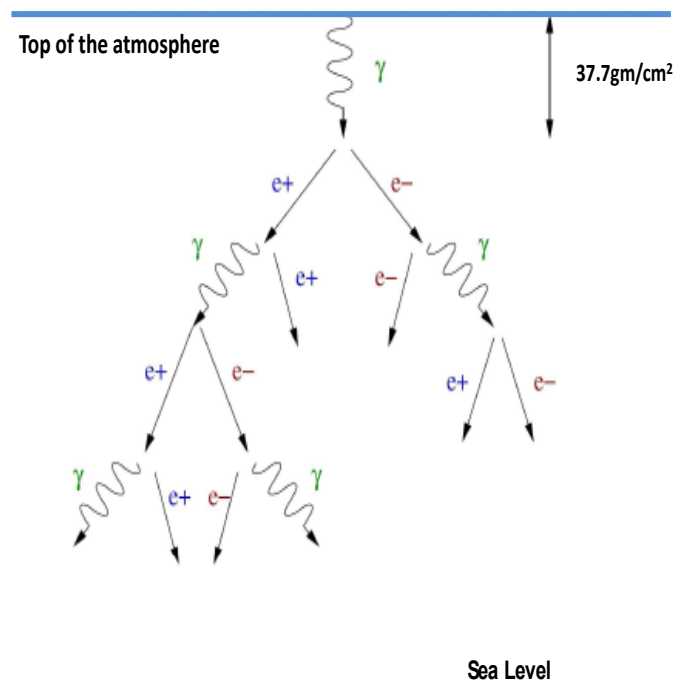
Figure 2.1: An illustration of a γ-ray induced EAS modified from [17].
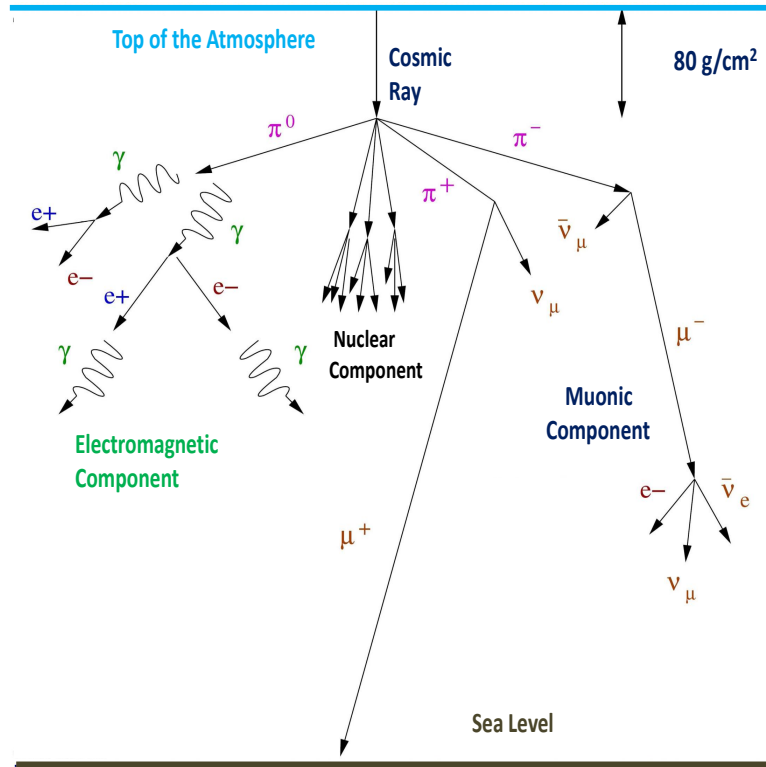
Figure 2.2: An illustration of a cosmic ray induced EAS modified from [17].

When a primary cosmic ray nucleus or proton collides with matter in the Earth's atmosphere, it produces a variety of secondary particles most of which are pions $(\pi^0, \pi^\pm)$. In the first interaction about 90% of particles produced are pions, of which about a third are neutral pions and the other two thirds are charged pions. The other 10% are kaons and other particles. The neutral pions decay almost instantly (0.83×10^{-16} s) into two gamma-rays and initiate electromagnetic sub-showers as discussed in the previous section. The charged pions decay into muons (2.6×10^{-8} s) which eventually decay into electrons. However due to their relatively long lifetimes, the charged muons sometimes remain in the shower until they reach ground level and generate an image that may appear in the camera as a full ring or a partial ring. This image represents another form of background to the gamma-ray showers that must be addressed, especially with single ground-based detectors. The EAS continues to evolve as long as the secondary particles have energies greater than around 1GeV, they interact again with the atmosphere and the hadron induced EAS evolves. Once the secondary particles have energies below about 1 GeV, ionization processes dominate and the EAS starts to die out.

The main difference between these two shower production mechanisms is the higher lateral spread and more irregular shape of hadronic showers. The high transverse momentum of the secondary pions and kaons for cosmic rays and large opening angles of the pion interactions lead

to an increase in fluctuations of the Cherenkov light distribution on ground. Another difference is seen in the mean free path, which is about 80 g/cm^2 for a 1 TeV proton and is about 37.7 g/cm^2 for a 1 TeV gamma-ray. This means that gamma-ray showers are initialized at higher altitudes than cosmic-ray showers. Another important difference is that for the same initial energy an EAS initiated by a gamma-ray has more Cherenkov light than a shower initiated by a cosmic ray. This is so because for a gamma-ray EAS, all of the primary particle energy goes into the secondary electron-positron pairs, all of which produce Cherenkov light. However, for cosmic ray showers a portion of the energy from the primary particle goes into producing secondary particles such as muons and neutrinos which contribute much less to the production of Cherenkov light than the electron-positron pairs. This also results in hadronic showers having a much higher muonic component than gamma-ray showers.

2.2　Cherenkov Light from Extensive Air Showers

When a charged particle travels though a dielectric medium it polarizes the air nuclei in its path. The polarized nuclei oscillate as they return to their equilibrium position. In the case of low particle velocities the electromagnetic fields generated by this process interfere destructively and produce no radiation. However, as seen in the majority of secondary particles produce by EAS, when the charged particles traversing the dielectric medium travels with speeds greater than the speed of light in that medium the polarized nuclei oscillate in phase and emit Cherenkov radiation. As seen in Figure 2.3, as the particle passes through the medium with $v > c_{medium}$ a shock wave is created behind the particle that results in energy lost by the particle as radiation. A common analogy use to describe this process is that of a sonic boom produce by supersonic aircraft. Since the aircraft is moving faster than the speed of sound, sound waves created by the aircraft do not move fast enough to get out of the way of the aircraft. As a result the waves stack up and create a shock front. In similar fashion, superluminal charged particles generate "photonic" shock waves as they travel through the Earth's atmosphere that manifest themselves as brief flashes of blue light.

The angle of emission of Cherenkov radiation (θ) is fixed with respect to the velocity vector of the particle. It is in this direction that the electromagnetic waves add up coherently according to Huygens' principle. The refractive index of the atmosphere decreases with height which according to equation 2.1 causes the Cherenkov angle to decrease with increasing height. We can also see that in time t the particle travels a distance given by βct while the radiation emitted by the medium travels a distance $\frac{c}{n}$t. Thus, the Cherenkov angle can be determined from geometrical arguments:

$$\cos\theta = \frac{\frac{ct}{n}}{\beta ct} = \frac{1}{\beta n} \tag{2.1}$$
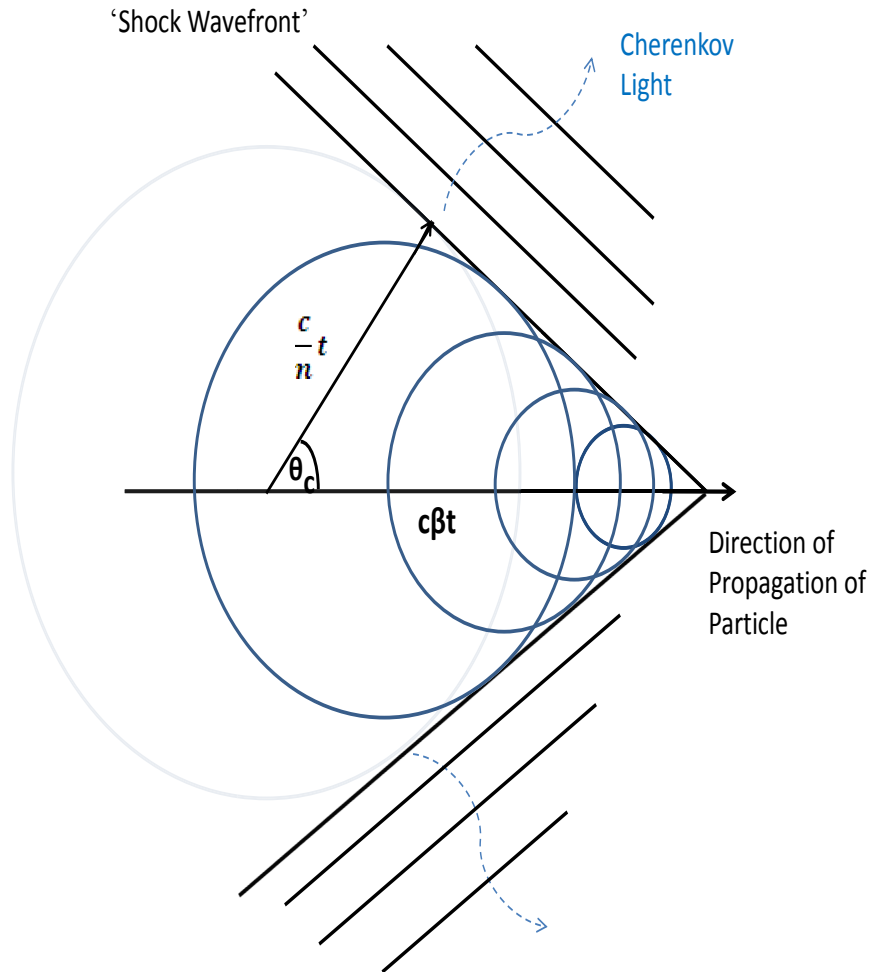
Figure 2.3: An illustration of a shock wave and Cherenkov light produced by charged particles when they pass through a medium with $v > c_{medium}$

If θ is set to zero then the threshold velocity below which no emission of Cherenkov light can occur is given by [18]:

$$v_t = \frac{c}{n(\omega)} = \frac{c}{\sqrt{\varepsilon(\omega)}} \tag{2.2}$$

where ω is the angular frequency of the Cherenkov radiation, c the speed of light in vacuum, ε the dielectric constant, n(ω) the index of refraction of the dielectric medium. Using the threshold velocity we can then see that the threshold energy a particle needs to have in order to emit Cherenkov radiation is given by:

$$E_t = \frac{m_o c^2}{\sqrt{1 - (v/c)^2}} \tag{2.3}$$

Where m_o is the rest mass of the particle. In the case of an electron moving through the atmosphere with a an index of refraction of 1.00029 at (sea level) the energy threshold is ~ 21 MeV and Cherenkov angle is $\sim 1.38°$.

Classically the energy per path length, in ergs per centimeter, emitted by a particle of charge e was derived by Frank-Tamm [19]

$$\frac{dE}{dl} = (2\pi e)^2 \int\limits_{(\beta n > 1)} (1 - \frac{1}{\beta^2 n^2(\lambda)}) \frac{d\lambda}{\lambda^3}. \tag{2.4}$$

It can bee seen from this equation that the λ^{-3} dependence contributes largely to the integral which means that shorter wavelengths are emitted more. For a real medium that is always dispersive, the emitted radiation is restricted to certain wavebands that satisfy the condition given by equation 2.2. Thus, Cherenkov emission in the atmosphere peaks in the ultra-violet (UV) and blue range. Shorter wavelengths are emitted, but are scattered and absorbed by the atmosphere.

2.2.1 Properties of Cherenkov Light in Extensive Air Showers

As mentioned above, hadronic nuclear collisions can generate pions with large transverse momentum which in turn create independent subshowers of various energies that cause multicored and overlapping rings of Cherenkov light on the ground. Furthermore, some of the charged pions make it to the ground before the light emitted by the secondary particles and produce a double peaked structure for the light arriving from hadronic air showers. In gamma-ray showers the energy of the primary photon is distributed evenly among all of the secondary particles and secondary particles don't acquire such large transverse momentum. Thus the resulting Cherenkov light on the ground is more uniform, circular, and centered about the shower core. In other words, a gamma-ray initiated shower remains compact and uniform about the shower axis whereas a cosmic-ray shower shows greater spread and irregularity.

The Cherenkov light produced by an EAS as seen at the detector level can be viewed as having three contributions. The most important contribution ($\sim 50\%$) comes from the particles (mostly electrons and positrons) at the shower maximum, where the largest fraction of the particles are produced. The second contribution comes from the tail of the shower, those particles that are closer to the ground. The third contribution comes from local particles (muons) that make it all the way to the ground causing an intense local peak of Cherenkov light [20]. For example, a 1 TeV gamma-ray initiated shower would have a shower maximum located about 8.1 km and produce a "light pool" on the ground with an impact radius of about 125 m. In this scenario we require that all particles in the extensive air shower travel along the shower axis. Given such an impact radius, the detector can have an effective collection area in the order of 10^4 m^2, which is much higher

than for typical satellite-born instruments. However, the EAS has a larger lateral extend mainly due to multiple Coulomb scattering of the electrons and positrons.

According to [18] the number of Cherenkov photons emitted by electrons between wavelengths λ_1 and λ_2 over a distance l given by:

$$N = (2\pi\alpha l)(\frac{1}{\lambda_2} - \frac{1}{\lambda_1})(1 - \frac{1}{\beta^2 n^2(\lambda)}) \tag{2.5}$$

where α is the fine structure constant and $n(\lambda)$ is the frequency-dependent index of refraction. As seen in equation 2.5, matters are complicated since the amount of light emitted depends on the index of refraction which is a function of pressure, temperature, water content and wavelength. Therefore, different atmospheric profiles result in different indices of refraction throughout the development of the shower and thus, in different amounts of Cherenkov light emitted. Fortunately, for the wavelength range 300 nm - 600 nm, the wavelengths relevant for Cherenkov radiation, the index of refraction changes only by about 5% [21]. One true concern is that most of the Cherenkov light produced is $\sim$ 10 km above ground (shower maximum) meaning the light stills has a long distance left to travel before reaching the detector. In traveling this distance the Cherenkov light encounters an atmosphere that attenuates it.

2.2.2   The Attenuation of Cherenkov Light in the Atmosphere

Most of the Cherenkov photons coming from an EAS are produced about 10 km above sea level (a.s.l) and as they journey down to the detectors are attenuated by different molecules in the Earths atmosphere. The extinction of Cherenkov light in the atmosphere comes from ozone absorption, aerosol scattering and molecular scattering. Ozone (O_3) is distributed in the atmosphere from about $10 - 50$ km a.s.l. in a region know as the stratosphere. This distribution region overlaps well with the heights of the shower maximums and so becomes a factor in the attenuation of Chernkov light. The disassociation of ozone, $\gamma + O_3 \rightarrow O_2 + O$, is an important process for absorbtion of wavelengths below 340 nm both in the ozone layer and near the ground [21]. Fortunately, this range covers two absorption bands, the Hartley band (200-310 nm) and a much weaker band the Huggins band (310 -360 nm) in which the large majority of Cherenkov light is emitted [22]. The second and most important process in the extinction of Cherenkov light comes from Rayleigh (molecular) scattering. Rayleigh scattering occurs when the wavelength of incoming radiation is much greater than the particles size. An important property of Rayleigh scattering is that the scattering cross section is proportional to λ^{-4} which tells us that shorter wavelengths are preferentially scattered. Mie scattering by aerosols also attenuates Cherenkov light, but it has the smallest impact. Mie scattering describes the scattering the of electromagnetic waves on spherical

molecules whose diameters are larger than the wavelength of the light. This occurs in the part of the atmosphere known as the boundary layer which ranges from 1 to 2.5 km. While ozone absorption and Mie scattering are site-dependent and variable, molecular (Rayleigh) scattering is predictable and almost constant at any site [21].

2.2.3   Detecting Cherenkov Radiation with the Imaging Atmospheric Cherenkov Technique

Ground based Imaging Atmospheric Cherenkov Technique (IACT) telescopes work by taking a snapshot of Cherenkov light from an EAS using a high resolution camera. The big reflector of the telescope collects a sample of the Cherenkov light from an EAS and focuses it onto the camera located on the optical axis of the telescope, at the focal plane of the reflector. The photomultiplier tubes (PMTs) in the camera convert the Cherenkov light into electrical signals that are then processed by the pulse counting electronics to be analyzed later. The Cherenkov light from an EAS last for a short burst of a few nanoseconds. Thus by matching the integration time of the detector to the duration of the short burst we can separate our signal from the noise dominated night sky background (NSB). The NSB comes from star light, fluorescent light from the ionosphere, local muons, moonlight and light from terrestrial sources.

As we mention before the camera is located on the focal point of the reflector pointing directly at the source. Recall that Cherenkov light is emitted along a small cone about the shower axis. The point of the cone that intersects with the ground is at a large distance from the detector, so the Cherenkov cone projects as an elliptical image in the focal plane of the detector. Thus for gamma-rays originating from a point source located at the center of the telescope FOV, the image of the Cherenkov light in the camera will be oriented so as to point radially to its center. In contrast, cosmic-ray arrive isotropically from every direction so their images do not point in any preferred direction.

In addition, due to the difference in the shower development we can use shape parameters such as the width and length of the elliptical image to differentiate between cosmic rays and gamma-ray showers. This was first done by Hillas [23] in 1985 and demonstrated in 1989 by the Whipple detection of the Crab nebula [24]. The selection criteria based on the Hillas parameterizations of the images recorded by the camera is the primary method of extracting the signal from the background.

2.2.4   Hillas Parametrization

As previously stated, the flux of cosmic rays is several orders of magnitude higher than the gamma-ray flux and thus it is crucial to be able to distinguish between images arising from gamma-

rays and those arising from cosmic rays. A method for doing this was developed by Hillas that consists of using a moment based analysis to fit a recorded image of a shower to an ellipse. This allows us to define six independent image parameters that reflect the physical characteristics of the shower. This technique is based on the fact that gamma-ray images appear as compact ellipses on the camera plane while cosmic rays are less define and have more of a spherical shape. The Hillas parameters contain information about the primary particle type, its energy and its arrival direction. The parameters considered (see Figure 2.4) are the following:

Width: The RMS of the angular length (in degrees) of the semiminor axis of the fitted ellipse. It corresponds to the spread of image pixel along the minor axis and represents the lateral size of the shower as viewed from the ground. The cut is referred to as MSW.

Length: The RMS of the angular length (in degrees) of the semimajor axis of the fitted ellipse. It corresponds to the the spread of the image along the major axis and represents the vertical size of the shower as viewed from the ground.

Distance: The angular distance (in degrees) between the center of the camera and the fitted image centroid.

Alpha: The angle (in degrees) between the fitted major axis and the direction to the center of the field of view.

Miss: The perpendicular (angular) distance between the fitted major axis and the center of the camera.

Size: Total integrated charge of all charge in all of the pixels in the image (not shown in Figure 2.4). It corresponds to the size of the shower (measured either in digital counts or photo-electrons) and thus relates to the energy of the incoming particle.
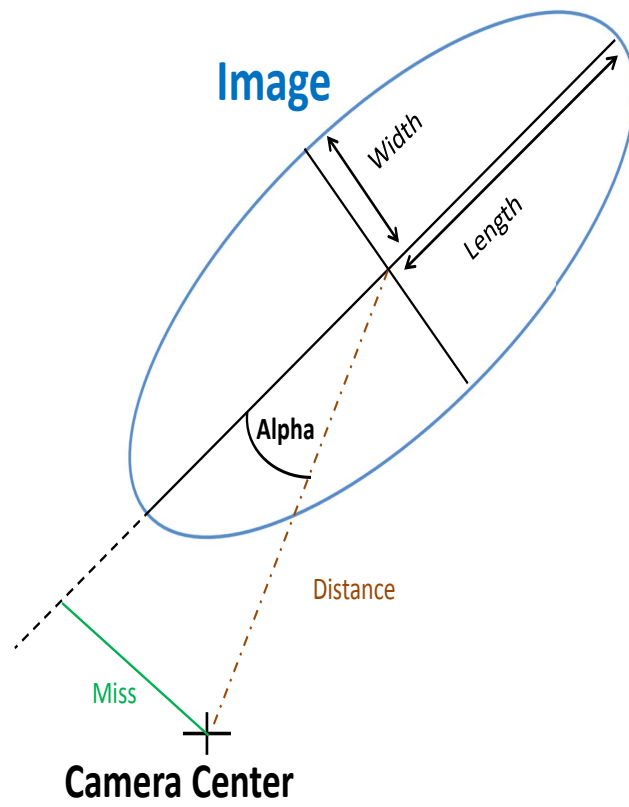
Figure 2.4: Schematic of the Hillas parameters of an image fitted by an ellipse.

CHAPTER 3

THE VERITAS OBSERVATORY

The VERITAS (Very Energetic Radiation Imaging Telescope Array System) collaboration is an international research effort to study and detect GeV-TeV gamma-rays from galactic and extragalactic sources. The collaboration involves institutions in Ireland,England and the United States of America. The VERITAS array consists of four, 12 m diameter imaging atmospheric Cherenkov telescopes (IACT) located on Mt. Hopkins south of Tucson, Arizona, USA., 1268 m above sea level. The array of four telescopes was completed in June 2007. It can detect photons from astrophysical sources at energies between 100 GeV and 30 TeV. Each telescope is equipped with a 499-photomultiplier tube (PMT) camera, spanning a field of view of $3.5°$ in diameter.

As part of an ongoing upgrade program, Telescope 1 was move in the summer of 2009 to improve the sensitivity of the array. The old array layout gives telescope baselines varying from 35 m to 127 m while the new layout distances range from 81 m to 127 m. Figure 3.1 shows a schematic representation of the array viewed from above with the separation distances between the telescopes and the corresponding telescope's names. Regular observations with the new layout of the four-telescope array started in September 2009. This and other improvements [25] have allowed us to use the approximately 1000 h per year of observation time more effectively.

The VERITAS array is one of a number of new generation of IACT projects worldwide for the study of VHE gamma-ray astronomy. Other such projects include international collaborations by MAGIC, HESS, and CANGAROO III. The MAGIC (Major Atmospheric Gamma Imaging Cherenkov) telescopes are located in Roque de los Muchachos observatory, Canary Islands 2200m a.s.l. and consists of two 17 m diameter reflectors. The High Energy Stereoscopic System (H.E.S.S.) collaboration is located in the Khomas Highlands of Namibia and is composed of an array of four telescopes 13 m in diameter and 1800 m a.s.l.. CANGAROO (Collaboration of Australia and Nippon for a GAmma Ray Observatory in the Outback) III is located 165 m a.s.l in Woomera (Australia) and has four 10 m diameter telescopes. In this chapter we will discuss the different components of the VERITAS telescopes.

Figure 3.1: An illustration of the old telescope layout (blue) and the new telescope layout (red). The difference being that Telescope 1 was moved 200 m eastward from its initial position.

3.1 The Reflector

3.1.1 Davies-Cotton Design

The spherical reflector is composed of 350 separate hexagonal mirror facets mounted on a steel space frame, the optical support structure (OSS), together act like a single spherical mirror focusing the reflected rays to a single focal point, see Figure 3.2. The reflector has a radius of curvature of 12 m, exactly half that of the individual mirror facets that make up its tessellated structure. Four quadrapod arms are attached at the sides of the OSS to hold a camera at the focal plane of each reflector at a distance of 12 m from the mirrors. This entire structure is moved by a commercial altitude-azimuth positioner which provides pointing to an accuracy to about $0.01°$ and can be safely operated at wind speeds up to 20 MPH. If more severe conditions exists, the telescope can be move to the parked position, with azimuth and elevation stow pins engaged, where the design can withstand speeds of up to 100 MPH. The slew speed of the positioner is up to $1°\text{s}^{-1}$ in both elevation and azimuth, but it is driven between $0.3°\text{s}^{-1}$ and $0.5°\text{s}^{-1}$ for safety reasons [26]. The entire structure is composed of the OSS, the mirror facets and the camera (which alone weights 350 kg) and is balanced by the use of a set of counterweights located at the back of the OSS. The weight of the structure causes some flexure in the OSS that is elevation dependent and results
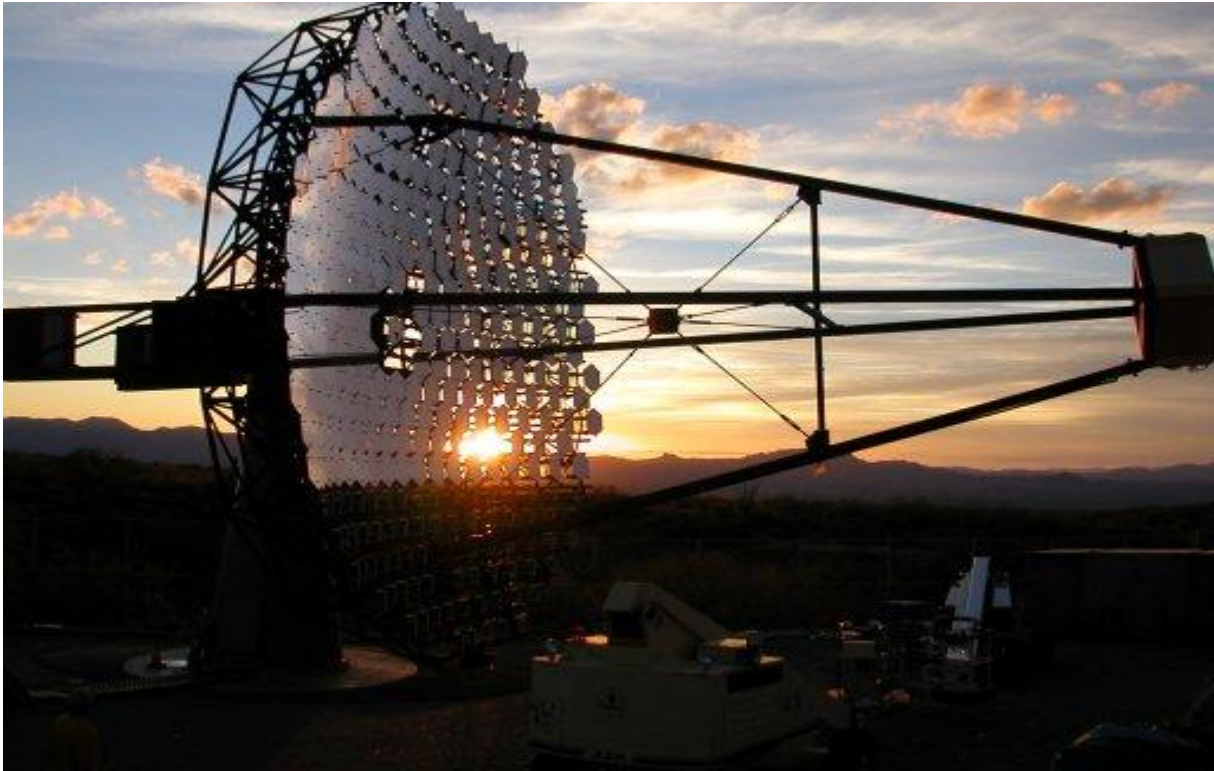
Figure 3.2: An photograph of telescope1 showing the OSS, mirror facets, camera, positioner and quadrapod arms.

in image distortions. There is a blurring of the RMS (root mean square) image width of a point source formed by all the mirror facets. In the next section we will discuss how such distortion is corrected.

Although the original Davies-Cotton design [27] was used as a solar concentrator, many gamma-ray astronomers have used it in the construction of the OSS and mirror facets due to its advantages over other designs. The main advantages of the Davies-Cotton design are that the separate identical facets make them relatively inexpensive to build, the alignment of the optical system is relatively simple, is more resistant to damage (replacing small mirrors versus one large expensive mirror) and as a whole the reflector has a superior off-axis performance when compared to parabolic mirrors. The disadvantage of the design is that it is isochronous meaning that the reflector introduces a temporal broadening spread into the light pulse. This is due to the spherical shape of the reflector. The parallel rays of light reflected by the outer mirror facets reach the focal plane before the rays reflected from the inner portion of the reflector thus creating a broadening of the light pulse. A f-number (ratio of aperture diameter of the optical system to its focal length) of f/1.0 was chosen for VERITAS telescopes. This particular f-number maximizes the optical quality while keeping the optics induced time spread roughly equal to the intrinsic spread of the Cherenkov shower.

3.1.2   The Mirror Facets

The VERITAS telescopes each have a 12 m optical reflector consisting of 350 identical hexagonal mirror facets covering an area of approximately 110 m^2. Each mirror has a radius of curvature of 24 m $\pm 1\%$ and are attached to the OSS using a triangular mounting structure which isolates the mirrors from optical distortions due to the flexure of OSS. The mirrors are attached to the triangular mount via three screws that can be adjusted to correct the exact pointing of the individual mirrors. The mirror facets are also front-aluminized, this adjusts the peak of the mirror reflectivity to about 90%. This makes the reflectivity response curve coincide with the peak of the Cherenkov spectrum from the air showers. The reflected light from the mirrors can then fall within a 10 mm diameter circle located at the radius of curvature.

3.1.3   Mirror Alignment

The mirror alignment is done when the mirror facets are replaced, re-coated or due to the normal wear and the tear of the telescopes that leads to misalignment. The purpose of the alignment is to have the 350 mirror facets positioned so as to act like a single spherical mirror focusing the reflected rays to a single focal point. The alignment is achieved by using the raster method. This is done by placing a CCD camera at the focal point of the reflector and then telescope is to perform a raster scan around a star with a typical observation elevation of about 70 degrees. The CCD camera records how much starlight each facet is contributing to the image at each point of the raster scan. This shows us that well-aligned facets will reflect the maximum amount of light when the telescope is pointing directly at the star. While misaligned facets will reflect the maximum amount of light when the angle between the star and the telescope pointing direction is twice the misalignment angle of the facet [28]. Once the misaligned angle is known for each facet the required adjustments are made. Once all the mirrors are aligned we are still left with correcting for distortions caused by the OSS flexure, which cause a spread in the PSF (point spread function) at different observing elevations. The PSF represents the optical distortion in the form of a blur. Previously this was corrected for by a bias-alignment of the the mirrors but now the raster method is used. In the bias-alignment method a small light weight laser unit is attached to each mirror facet. The laser beam is directed onto a CCD camera at the focal plane of the telescope and a CCD image of the focal plane is then obtained. The telescope is raised to an elevation of 65 degrees,the elevation at which the best focus is achieved, and another CCD image of the focal plane is obtained. The two images are compared and the amount by which the laser spot moves on the focal plane bias is measured. The process is repeated for all mirror facets. Once the bias is know the mirrors are intentional misalignment in the opposite direction of the bias while in the stow position. The misalignment is such that the OSS flexure causes the mirrors to return the correct alignment at the

desired observing elevations, optimized at 65 degrees, see [29] for more details. The raster method is favored over the bias alignment because it is easier to implement and it is more accurate [28].

3.2   Camera

The imaging cameras of the VERITAS telescopes are located at the focal plane of each reflector at a distance of 12 m from the mirrors. Each camera has a field of view of $3.5\,^\circ$ in diameter and an array of 499 photomultiplier tubes (PMTs), see Figure 3.3. Each pixel subtends an angle of $0.125\,^\circ$ in diameter. The camera is installed inside a focus box, a sturdy light-tight, water-tight structure whose shutter is opened and closed using a remote control. The shutter is closed during non observing times to protect the array of photomultiplier tubes (PMTs) from damaged by UV light. In order to increase the amount of light collected by the PMTs, light cones are placed in front of them. In addition the PMTs are packed in a hexagonal grid pattern to minimize the dead space between them. More details about the PMTs and other camera components follow.
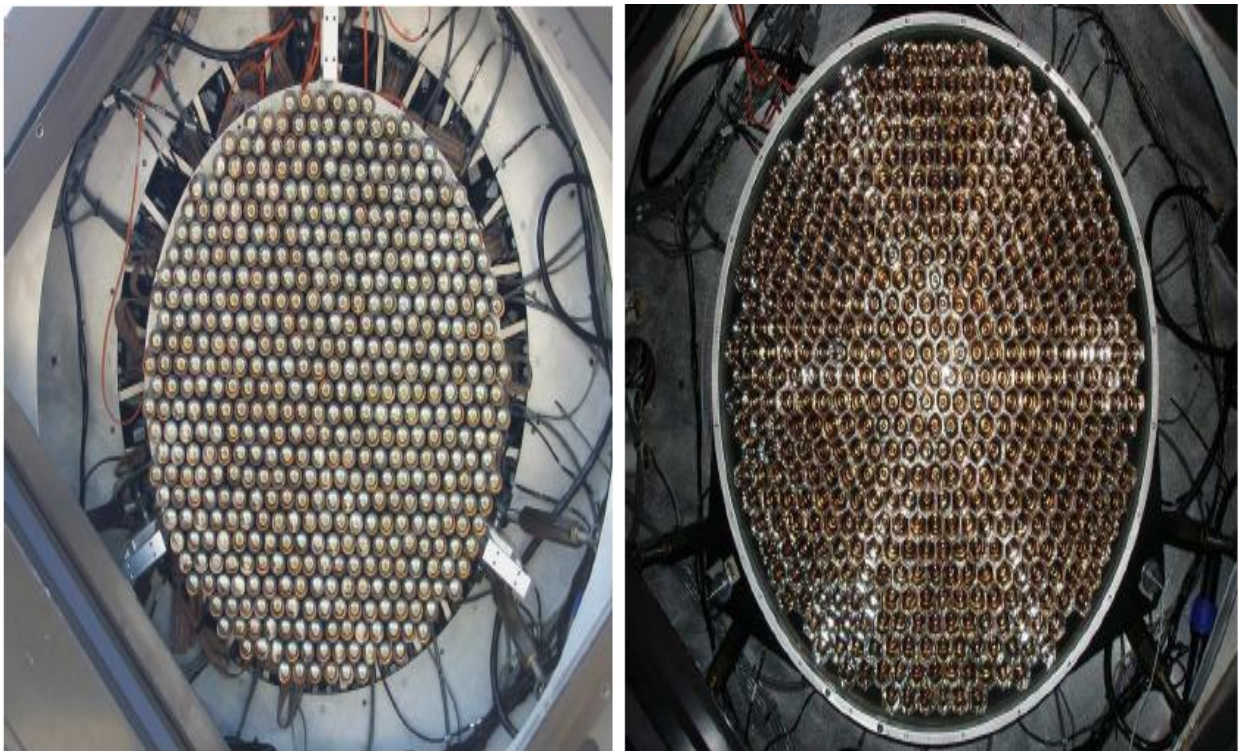
(a) A photograph of T2's camera with its 499 PMTs.

(b) The same as in (a) but with the light cones added.

Figure 3.3: The VERITAS camera [30].

3.2.1   Photomultiplier Tubes

The purpose of the PMTs is to detect the faint and short lived flash of Cherenkov light. Currently, PMTs are the only devices that have the necessary technology to detect such flashes, that is a a low noise, high gain, fast response time [31]. A PMT consists of photocathode, a series of dynodes with a sequentially increasing potential. First, a photon passes through a glass window at the front of the PMT and strikes the photocathode, if it has the necessary energy then it will remove an electron (photoelectron) from the surface of the metal. The quantum efficiency (QE), is the PMT parameter used to describe the probability of a photoelectron being released if the photocathode is struck by a photon. The QE depends on the material of the photocathode and the wavelength of the original photon. The charged electron is then accelerated by the a strong potential and strikes the first dynode and more electrons are emitted. This process is repeated at each of the successive dynodes until all electrons are collected at the anode where a output current is obtained.

The VERITAS PMTs are the Phillips Photonis XP2970/02 model that have 10 dynode stages with a bi-alkali photo-cathode and 29 mm diameter PMTs operated at a gain (ratio of electrons produced at the anode per photoelectron generated at the photocathode) of 2×10^5 [32]. Such gain results in currents between 3 μA and 6 μA at the anodes for dark field and bright field sources respectively. The PMTs have a maximum QE $\sim 25\%$ for wavelengths ~ 400 nm and $\sim 23\%$ for wavelengths relevant for Cherenkov radiation (~ 320 nm). However, as part of the upgrade program, these PMTs will soon be replaced by ones with QE that peak $\sim 35\%$ in the blue as compared to a peak efficiency of 18% for the ones currently used.

3.2.2   High Voltage

The hight voltage (HV) required to operate each PMT is provided by a multichannel modular commercial power supply (model CAEN SY1527/A1932.) The HV is comprised of a pair of crates that hold a total of 11 modules with each module controlling 6 sectors and each sector controlling 8 channels. The voltage of each channel can be individually set to within a 1 Volt precision and up to a max of 1500 V. The HV for each PMT is set by a control program through an Ethernet interface. This program allows the voltages to be set manually from a graphical interface of the program, or the program can set the voltages automatically by reading them from the VERITAS database. In addition, the program continuously monitors the voltage and automatically changes the voltage of each channel depending on the monitored level of the anode current. The program also has a built in safety feature to automatically switch off the PMTs if the anode current exceeds a preset threshold.

During the 2006-2007 season a few threshold conditions were defined. A pixel was immediately

suppressed if the the anode current exceeded 80 μA or if the anode currents of three adjacent pixels surpassed 20 μA. The camera was turned off if at the same time more than 20 pixel' s currents exceeded 80 μA. This threshold is known to be surpassed when bright stars move through the PMT's field of view or when local light sources shine near the telescopes.

In order for the HV program to automatically set the voltages from the VERITAS database, the PMTs must be flat fielded first. This is done at the beginning of the night by a fast pulsing light uniformly illuminating the entire camera and recording the response of each PMT. The relative gain of each PMT is obtained by comparing the integrated charge of each PMT response to the average of all the PMTs. Once this is known, the PMTs's high voltages are adjusted to make the relative gains of all PMTs to be within 10 % of each other. This ensures an even response across the camera [33]. This process is known as flat-fielding.

3.2.3 Preamplifiers

Despite the large gain provided by the PMTs, high bandwidth (300 MHz) preamplifiers are installed at the base of each PMT. This boosts the signal by a factor of 6.6 to reduce the noise acquired during transmission through the $\sim$50 m RG-59 coaxial cable extending from the camera box to the FADCs boards located in an electronics trailer. The $\sim$50 m RG-59 coaxial cable attenuates the pulse by 25% which means the voltage delivered to the front end of the FADCs with a range of 0 V to -1.6 V changes to 0 V to -2.2 V [32]. Another feature of the preamplifier is that it provides a direct DC output for monitoring the anode-current with the current monitor system.

3.2.4 Current Monitor

Each of the four telescope's camera has a built in system that monitors the DC anode currents in the PMTs to prevent them from being damaged. As stated above when bright stars or bright ambient light pass through the field of view of the telescopes, this can cause the anode current to exceed a preset threshold which can permanently damage the PMTs. The monitor currents come from 16 FPGA-controlled circuit boards, with 32 channels on each board, located inside the camera box and connected to the preamplifier DC output. Each of the channels can be used for reading and transmitting PMT anode currents. This current readout gives a precision of 0.5 μA with a dynamic range of 0 μA - 125μA. The currents for all of the PMTs are displayed on a GUI in the control room. An observer can then view the current of any PMT by clicking on any PMT's corresponding pixel on the pixel map display. The current monitor also reports the anode current to the HV control program to use in determining dangerous situations that require suppression of PMTs's voltages. The current monitor program logs the currents to a local file on a disk for

long-term monitoring of the PMTs, to be used in identifying changes in the its performance.

3.2.5   Charge Injection

The charge injection (QI) system, located inside each camera, is a pulse generator that injects pulses of a certain shape, frequency and amplitude selected by the observer to the preamplifiers. It sends pulses directly to the preamplifiers to simulate Cherenkov light that would normally be generated by the PMTs. The QI system is used to calibrate, test and diagnose the full data acquisition (DAQ) electronics following the PMTs. The QI is particularly handy since it can be operated during daytime when the PMTs cannot be used. The QI system consists of a central QI circuit board fanned out to individual PMT channels. It uses a programmable pulse generator (PPG) connected to the fan-out/mask board attached to each of the 16 current monitor boards.

3.3   Trigger System

Since cosmic rays and muons both produce gamma rays and thus Cherenkov light with similar characteristics as those from the sources of interest, the trigger system serves as a way to efficiently select the Cherenkov light caused by very high-energy gamma and reject random PMT noise. In principle, this could be done by using a very low threshold trigger but this would produce large trigger rates. Thus a three level trigger scheme was developed allows efficient selection of gamma-rays events and rejection of noise events. At the first level, the PMTs generate a trigger if at least $\sim$5 pe are detected within about 3 ns. Next at the second level, a pattern-sensitive logic searches for 3 nearest-neighbor PMTs that trigger within a time span of about 7 ns. At the third level, a trigger is produce only if at least two telescopes produced a trigger within 100 ns of each other [34].

3.3.1   Level One Trigger

The level 1 trigger (L1) acts at the single pixel PMT level. In each telescope the L1 trigger is composed of 499 Constant Fraction Discriminators (CFDs), one for each PMT, which work by making three copies of each analog PMT signal. The first copy goes into a simple threshold discriminator that generates a trigger signal if the amplified input pulse from the PMT exceeds a programmable threshold voltage of 50 mV ($\sim$5 photoelectrons) [34] . The second copy is delayed, inverted and fed into a Zero Crossing Discriminator (ZCD). The third copy is attenuated by some factor and then passed to the ZCD. These two pulses are then summed by the ZCD and the zero crossing point is found (the time at which the two pulses exactly cancel each other out). The zero crossing point is routed from the ZCD along with the output of the threshold discriminator to a flip-flop. The output of the flip-flop is used as the CDF trigger time that is then routed to the

Trigger 2 system.

Fluctuations in the night-sky background causes the PMTs to produce small variations in its output current that slightly degrade the calculation of the zero crossing point of the pulse (timing jitter). This jitter can be reduced by adding a constant DC offset to the ZCD which prevents it from triggering on small distorted pulses at the cost of raising the threshold of the telescopes. Adding a constant offset is also not desirable because the night sky background (NSB) can vary by as much as a factor of four. Thus an optimum offset is needed that triggers on small pulses and minimizes the jitter. To accomplish this a novel circuit, the rate feedback (RFB) loop, is added to the standard CFD design. The RFB loop automatically adjusts the ZCD offset as the NSB changes which in turn suppresses the NSB triggers which in turn better adjusts the effective threshold. The CFDs operate at a 50 mV threshold, a 10-12 ns output trigger signal width, a jitter of less than 1 ns and a RFB value of 60 mV/MHz [35].

3.3.2   Level Two Trigger

The L2 trigger is a pattern selection trigger (PST) that is programmed to recognize the gamma-ray like events formed by a certain pattern of L1 pixel triggers. It acts at the telescope level using the 499 L1 triggers from each camera as input. The L2 trigger system is motivated by the idea that NSB will generally only trigger one or two adjacent pixels within the camera. In contrasts, gamma-ray induced Cherenkov showers will trigger three or four adjacent pixels in a narrow coincidence time interval because of their compact nature.

PST is implemented by feeding the outputs of the CFD L1 signals into an ECL signal splitter that copies and routes the pixel signals into 19 separate overlapping pattern selection modules of 59 pixels [35]. These 19 modules come with programable look-up memory chips. If the preset number of pixels trigger within 5 ns of each other, the memory chips search to match this pattern with one of the ones that was loaded into the memory of the PST telescope trigger. If a match is found a PST level 2 trigger is sent to the third level of the trigger system. Since showers that only trigger the outer ring of pixels will be poorly reconstructed due to the truncation of the image, only 463 of the 499 CFDs are used. The timing of the L2 trigger is taken from a delayed copy of the signal from the comparator (device that compares two voltages and determines which one is bigger). The time jitter in the circuit is on the order of 5 ns, that requires an L1 pulse width of at least 10 ns to guarantee 100% L2 trigger decision efficiency [30].

The CFD threshold and number of adjacent pixels required to initiate a telescope trigger are chosen by special type of run that steps through a range of CFD thresholds and records the Level 2 trigger rate. The graph of L2 or L3 trigger rates as a function of the L1 CFDs threshold is known as a bias curve. The curve has two important regions. The part of the graph with a steep decent,

between 0 mV and ~50 mV, is the region dominated by NSB fluctuation triggers. The flatter part of the curve, above ~50 mV, represents the triggers due to cosmic-ray showers. The CFD trigger threshold is chosen to be as close to the inflection point of the curve without being in the regime dominated by NSB.

3.3.3 Level Three Trigger

A third level trigger system (L3) is needed because the L1 and L2 triggers from a single telescope alone could not be used to differentiate between images of Cherenkov light formed by local muons with large impact parameters from images formed by VHE gamma-ray air showers. Such ambiguity would be prevalent since at low energies the background is dominated by the night-sky fluctuations and local muons. Fortunately, local muons generally produce Cherenkov light over an area small enough to only trigger a single telescope. Therefore, the L3 trigger requires that the shower image be seen by more than one telescope to eliminate the muon background noise. This reduces the CFD thresholds and therefore provides a significant increase in the sensitivity of the detector, especially at low energies.

The main components of the L3 hardware consists of two custom built VME modules, a Pulse Delay Module (PDM), a Sub-Array Trigger Board (SAT) and a commercial GPS clock. The Digital Asynchronous Transceiver (DAT) modules consist of two 6U high, single width VME modules. One of them is the transmitter unit, DAT-TX, and the other one is the receiver unit, DAT-RX, the two are connected by fiber optic link over a distance of up to 150 m [30].

The L2 triggers signals are passed from each individual telescope to a central control trailer via optical fibers that link a transmitter-receiver pair of DAT modules at each side. The DAT modules with the fiber optic link are chosen over coaxial cables because of their low time jitter. However, using the DAT modules does have a disadvantage. It is not possible to send asynchronous signals directly through that connection since the lasers that would be used with them have a safety feature that forces the DAT to shut off if no data are transmitted every microsecond or so [36]. The safety feature is bypassed by having the DA-TX module combine the L2 triggers with a 25 MHz clock in XOR logic and also by transmitting the signal over a fibre optic line via a pulsed laser signal to be decoded at the receiving module (DAT-RX). A copy of the clock signal is also sent to the DAT-RX receiver is similar fashion. The DAT-RX receives the optical signal and matches it using XOR logic to the copy of the original 25 MHz clock signal and the original input signal is recovered.

The PDM unit is responsible for applying a couple of delays to the L2 triggers arriving at the central control trailer. Since each telescope is found at a different location in the site, a delay is needed to compensate for the different fiber optic cable lengths carrying the L2 signal to the

central control trailer. This delay can be compensated exactly by the PDM delay lines using precise measurements of the optical fiber length. A second delay is needed to account for the different arrival times of the Cherenkov wavefront to individual telescope reflectors. The second delay is continuously updated every five seconds since it depends on the pointing direction of the telescopes which is constantly changing as the telescope tracks a source across the sky. The PDM is composed of 32 independently programmable digital delay lines, each with a 2ns step size and a 100ns-16μs range [35].

The SAT module is used to determine whether a pre-determined array trigger condition occurs if a multiple of these delay adjusted L2 signals falls in a certain coincidence gate. If so, it issues the array trigger to command the Data Acquisition (DAQ) to record the event. An event is clusters of pixels in the camera that lit up.

3.4   Data Acquisition

The VERITAS data acquisition (DAQ) system also operates in three levels at the VME crate, telescope, and array levels. The VME DAQ (VDAQ for short) guides the control and read out of the Flash Analog-to-Digital Converter (FADC) Board channels. At the telescope level, the Event Builder merges the data from all VME crates into single telescope events. Finally, at the array level Harvester collects single events from each telescope and the array trigger to form the final array data product [37].

3.4.1   FADC Boards

Each of the 50 custom built FADC boards has 10 input channels with each PMT signal cable connected directly to one channel at the front end of the FADC boards. The FADCs measure time-varying voltages from the PMTs, digitizes them and buffer them continuously at a 500 MHz sample rate (i.e., each sample has 2ns time width) into a circular memory depth of 8 μs. When an array trigger occurs the FADCs stop digitization. At this point the Virtual Machine Environment (VME) acquisition asks the FADC boards to look back in their 8 μs circular memory buffer to extract a 48 ns or equivalently 24 samples segment (the settings for the 2006-2007 season) that contains the pulses that caused the system to trigger and records the FADC memory. The look back time for each channel is approximately the time between signal digitization and trigger decision plus the time of propagation of the signal [38].

Each FADC channel has an 8-bit dynamic range corresponding to 0-255 digital counts if the signal traces follow a high gain path to the FADC channel. However, if the dynamic range is exceeded, an analog switch connects the FADC to a delayed low gain path which effectively increases

the digital counts from 256 to 1500 (each digital count is equivalent to ~ 0.19 photoelectrons at the nominal PMT gain) [33].

3.4.2   VME Data Acquisition

The VME Data Acquisition System (VDAQ) serves as the interface between the five VME crates that control the digitization of the PMT signals and the Event Builder system that merges the event fragments from those separate VME crates. Four of the (VME) crates hold the FADC boards and the fifth one holds the Clock Trigger Board (CTB) and the Global Positioning System (GPS) clock. Once a crate's clock-trigger board receives a trigger, each FADC channel locates the appropriate buffer range and the VME CPU initiates an A32/D32 chained block transfer (CBLT) of the clock trigger and FADC ring buffer memory into the VDAQ buffer. During the CBLT, each VME crate raises a busy flag. The CTB combines the busy levels from each crate into a single telescope busy level to indicate that it is incapable of receiving anymore L3 triggers. The VDAQ program buffers the event fragments and passes them to the Event Builder via a Scaleable Coherent Interface (SCI) (a high-speed computer bus). After the CBLT is complete the telescope busy is unset and the telescope is ready to receive the next L3 trigger.

The VDAQ is also responsible for CFD settings such as threshold, output width, delays and rate feedback. It also programs the FADC when a pedestal trigger occurs to override zero-suppression [38]. In addition to receiving L3 triggers, the VDAQ also receives a serialized signal (event mask) that contains a unique event number for the event and the type of trigger. This information is copied to each crate and encoded into the event fragments from each crate to allow the synchronization of the data by the Event Builder program.

3.4.3   Event-Builder

The Event Builder performs a data quality control by looking for incomplete or fragmented events and combining them into telescope-level event information which it then copies to a local disk and then sends to Harvester. The Event-Builder is a multi-threaded C++ program, typically containing five threads: Communications, SCI Buffer Acquisition and Parsing, Event Building, Disk Writer, Network Writer [37].

The event building process begins with the transfer of the event fragment buffers from the VDAQ via the SCI Buffer Acquisition Thread. The SCI Buffer Parser parses the buffer and event fragments are organized into a structure which indexes the data by event number. Once all the fragments from all the crates for an event have arrived, the Event Building thread combines all fragments to produce a complete single telescope event. When $\sim$160 kBytes of telescope events

have been accumulated, the Event Building thread sends this buffer to the Disk Writer and Network Writer to have the buffer saved to a local file and also sends it to the Harvester via GBit Ethernet.

3.4.4   Harvester

The Harvester is a single 8 core computer that assembles the telescope files into a single array file. It combines events from all telescopes with information from the L3 trigger system and another GPS times stamp into a single array event. The Harvester then saves the merged data buffers to a local RAID disk in real time in a custom format named VERITAS Bank Format (VBF). A customized compression algorithm is then applied to the data file to reduce its size.

CHAPTER 4

CRAB OBSERVATIONS AT VARIOUS
ZENITH AND AZIMUTH ANGLES

4.1   The Crab Nebula and Pulsar

The Crab Nebula is one of the most studied celestial objects because of its strong and fairly persistent emission. The Crab Nebula is the remnant of a supernova (SN) explosion whose appearance was noted by Chinese and other astronomers in 1054 A.D. [39]. The SN explosion left behind a pulsar (a rotating neutron star) and a nebulae. The Crab pulsar, PSR J0534+220, was formed from the core collapse of the progenitor star while the outer material of the progenitor star that is thrown off forms the nebula part which is located around the pulsar. The pulsar rotates with a period of 33 ms and has a spin-down luminosity of $\approx 10^{38}$ergs. The spin-down luminosity is efficiently converted into radiation that powers the surrounding nebula through a relativistic wind of particles and magnetic fields that cause the nebula to radiate in all wavelength bands from radio waves to gamma rays [40]. This system is usually referred to as a prototypical Pulsar wind nebulae (PWNe) system.

Recent detection of the Crab pulsar above 100 GeV by the VERITAS collaboration gives us new picture of the high energy gamma-ray emission from pulsars. With 107 hours of observed Crab pulsar time between September 2007 and March 2011, the VERITAS array detected a pulsed gamma-ray emission (see Figure 4.1) between 100 GeV and 400 GeV. Figure 4.2 clearly shows that a broken power law is a much better parametrization of the spectral shape above 1 GeV than an exponential cut off which makes curvature radiation as the production mechanism for pulsed emission from the Crab pulsar above 100 GeV only possible under extreme assumptions [41]. The assumptions being that the acceleration field be close to the maximum allowed value and the radius of curvature be close to the light cylinder radius. Furthermore, using a gap model in which the accelerating electric field is parallel to the magnetic field [42] show that IC scattering is a much more likely mechanism for the production of gamma-ray pulsed emission for energies > 100 Gev. Thus due to the VERITAS detection of gamma-ray pulsed emission from the Crab pulsar a more
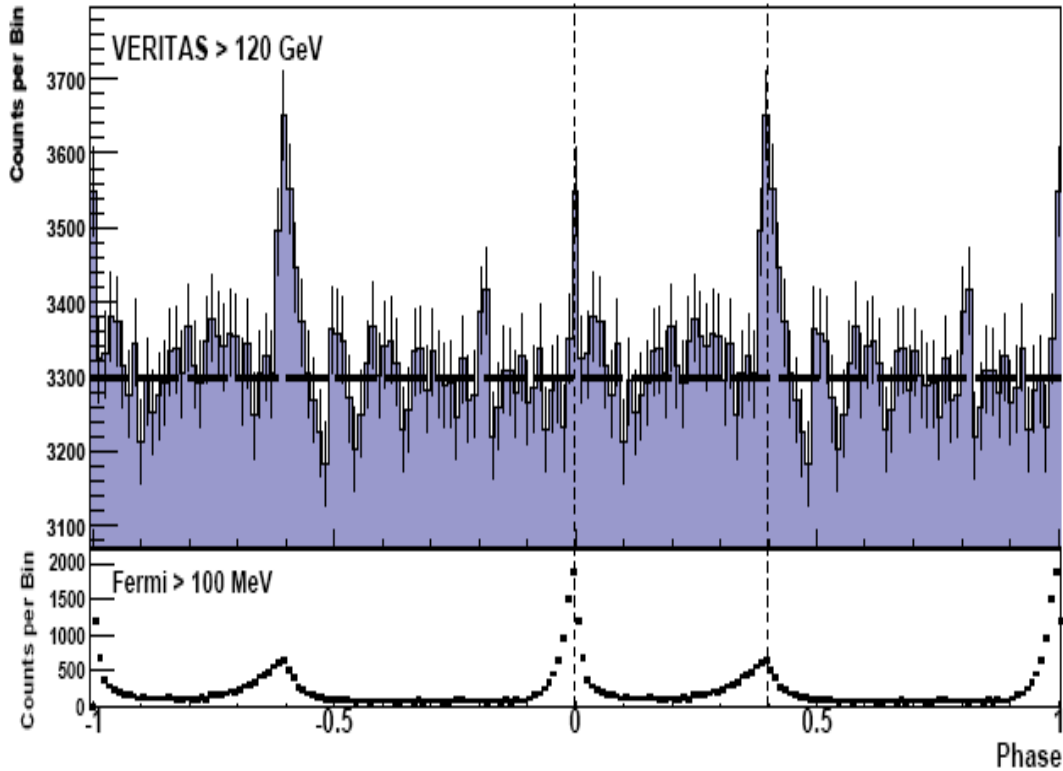
Figure 4.1: A pulse profile of the Crab pulsar showing both VERITAS and Fermi-LAT data. The dashed horizontal line shows the background levels and the vertical dashed lines mark the best-fit peak positions [41].

likely candidate, inverse-Compton scattering, emerges as the favored production mechanism for observed gamma-ray emission above 100 GeV.

The emission mechanisms of the Crab Nebula consist of two nonthermal processes: synchrotron and inverse Compton (IC). The radiation emitted from these two mechanisms generates a continuum of radiation that covers a spectral range from radio to VHE gamma-rays. Synchrotron emission processes can account for spectral radiation from the radio band up to 100 MeV. Inverse Compton scattering can account for emission from 100 MeV-Tev energies [43]. These two processes generate the double peak in the broadband energy spectrum, as illustrated by [43]. Here the first and second peak represent emission coming from synchrotron and inverse Compton scattering processes respectively, see Figure 4.3.

The VHE emission of the Crab Nebula was first detected by the Whipple Collaboration in 1989 using the atmospheric Cherenkov technique [24]. Due to their strong and fairly steady emission, VHE sources are often quoted in Crab units by various observing groups. However, in February of 2009 and in September 2010 the Large Area Telescope (LAT) on board the Fermi Gamma-ray
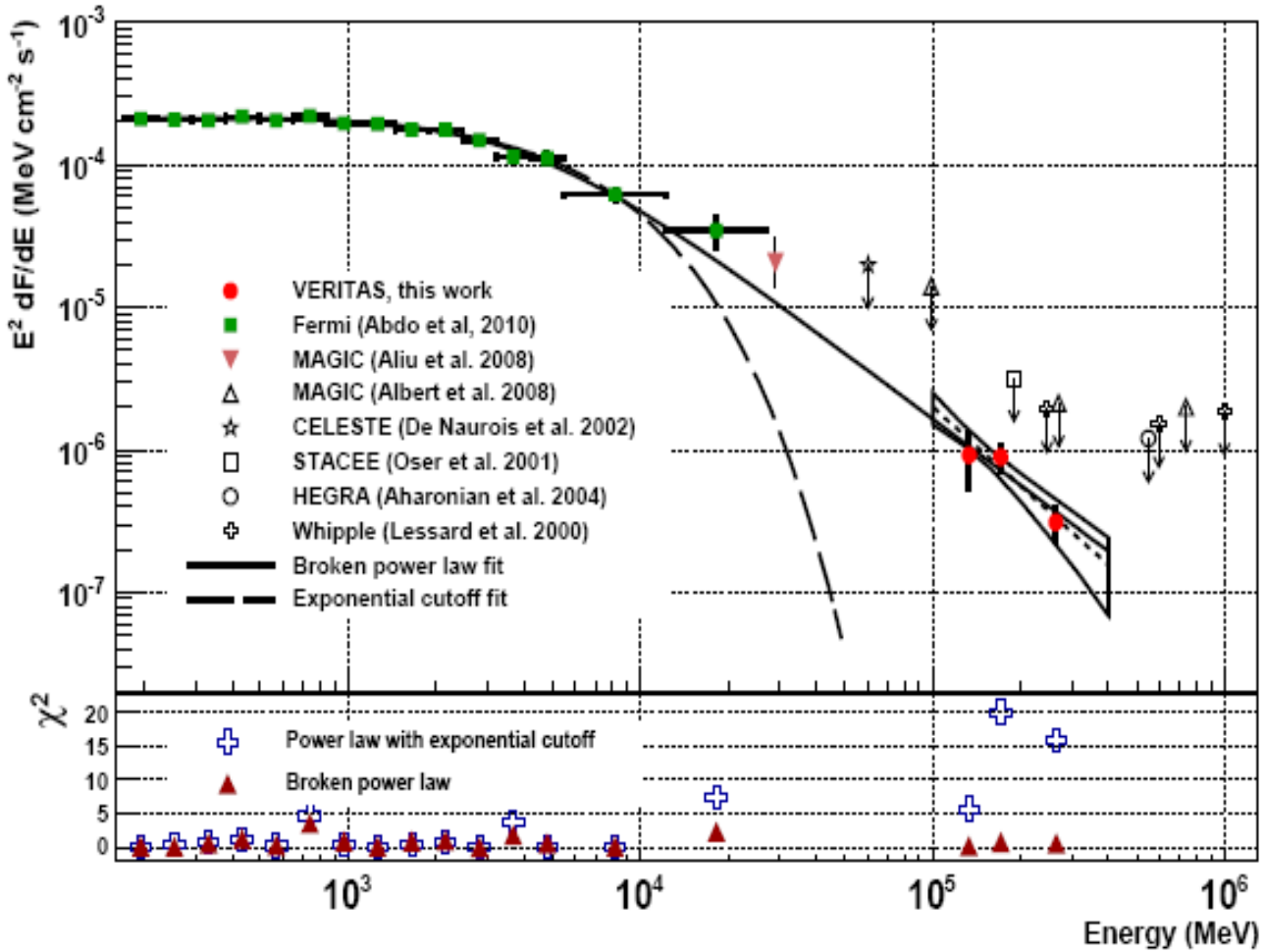
Figure 4.2: Spectral energy distribution of the Crab pulsar in gamma-rays (top portion). The MAGIC, FERMI-LAT and VERITAS data are represented with the filled markers and upper limits set by other experiments are represented by unfilled markers. The χ^2 (bottom portion) for two different parametrization fits of Fermi-LAT and VERITAS flux measurements clearly show that the power law parametrization is the best fit of the Crab pulsar spectrum [41].

Space Telescope detected flares in the gamma-ray flux from the nebula that were four and six times, respectively, higher than normal [44]. The flares were observed in the 100 Mev to 10 Gev energy range. The AGILE (Astrorivelatore Gamma a Immagini Leggero) satellite confirmed the September gamma-ray flare in the direction of the Crab nebula with a gamma-ray flux three to four times bigger than during normal non active times [45]. However, this has not been confirmed by the VERITAS and the MAGIC collaboration in the 100 MeV to 1 TeV energy range neither by INTEGRAL in the 20-400 keV window nor by SWIFT/BAT in the 14-150 keV energy range [46]. Such flaring activity would put into question the Crab's title of "standard candle" in the 100 Mev to 10 Gev energy domain, but recent results and observations at higher resolution have proposed
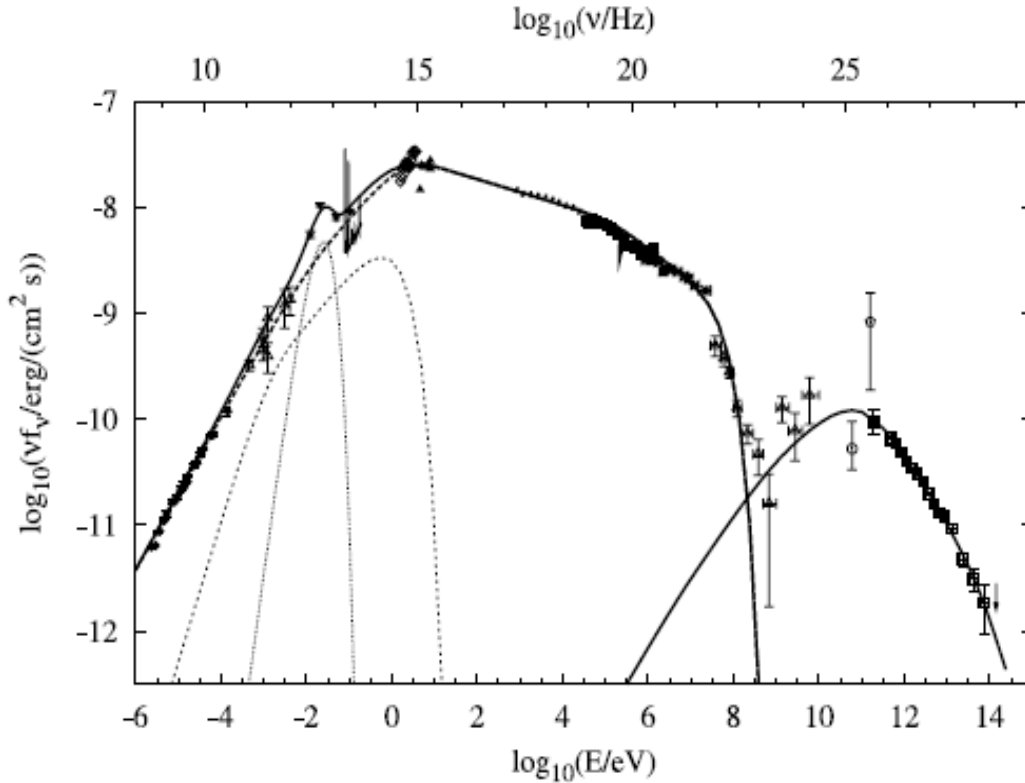
Figure 4.3: This graph of the Crab spectrum covers the energy range from radio to VHE. The two nonthermal emission process synchrotron (thick-dashed line on the left) and IC (solid line on the right) are also illustrated on the graph [43].

that the flares are coming from one of its dynamic structures. Komissarov and Lyutikov suggest that the gamma-ray variability comes from the inner knot as result of a Doppler-boosted shock emission [46].

In this chapter we will investigate previous Crab data sets to look for systematic effects that might create a change in the measured Crab flux at TeV energies. In particular zenith and azimuth pointing directions of the telescopes will effect the observed γ-ray rates of the Crab. Thus we will examine these effects and how well they are understood in the context of the zenith angle and azimuth angle pointing direction. In the next chapter we will examine how well the changes in the gamma-ray rates can be explained by the strength of the geomagnetic field.

4.2   Crab Observations

In an effort to study how varying the zenith and azimuth angles affects the observed gamma-ray rates of the Crab nebula, 47 quality Crab runs were selected under clear atmospheric conditions from the 2007-2008 observation season of VERITAS, see Table 4.1. Poor weather conditions are not desirable since it causes irregular scattering or absorption of the Cherenkov light which results

Table 4.1: Quality selected data for the Crab. The information in the chart was obtained from the summary list produced from running the programm Datareader.

| Zenith	Date	Zenith	γ/min	Read Events	Pass Cuts	σ	Az	Run #	ON	OFF	Excess
	20071010	10.0	6.14	296590	2956.00	15.41	168	37009	143	142	123
	20071014	13.3	6.21	306430	3170.00	14.87	222	37195	150	176	125
	20071015	15.0	7.60	280940	3440.00	16.52	233	37231	165	165	141
	20071016	13.7	7.39	286720	3114.00	17.12	227	37266	171	162	148
	20071017	13.5	8.07	288070	3373.00	17.89	223	37297	188	180	162
	20071114	15.8	7.40	308970	3544.00	16.58	127	37946	176	191	149
	20071114	12.5	8.42	312890	3547.00	18.43	139	37947	195	180	169
	20071114	10.0	6.49	263470	2669.00	16.40	168	37948	149	130	130
	20071114	9.6	7.50	316110	3113.00	18.01	195	37949	170	135	151
	20071114	12.4	8.13	316400	3472.00	18.15	217	37950	188	172	163
	20071117	15.1	6.75	257670	2770.00	16.70	130	38034	155	136	136
	20071117	11.8	7.64	262910	2796.00	18.40	144	38035	172	129	154
	20071118	13.2	8.63	303810	3414.00	19.25	135	38064	196	158	173
7 to 17	20071204	10.3	6.99	325850	3324.00	16.59	160	38200	163	158	140
	20071206	10.2	7.54	322290	3199.00	17.70	164	38273	173	150	152
	20071214	11.2	6.77	287110	2482.00	17.43	145	38362	152	111	136
	20071215	11.1	7.36	314860	2846.00	17.65	156	38405	168	140	148
	20071230	9.8	9.08	313350	2918.00	21.25	162	38523	197	108	182
	20080112	14.6	9.31	292130	3142.00	20.42	231	38764	209	153	187
	20080130	10.0	7.66	304700	2584.00	18.68	167	38957	171	120	154
	20080130	10.4	6.84	304040	2485.00	17.60	201	38958	153	109	137
	20080202	14.3	6.83	302450	2666.00	16.96	127	39035	155	129	137
	20080202	12.1	6.68	247030	2238.00	14.84	146	39036	124	111	108
	20080203	10.2	6.77	300410	2429.00	17.22	181	39072	153	118	136
	20080203	10.8	6.87	300110	2465.00	17.99	205	39073	152	98	138
	20080206	9.8	7.48	306760	2445.00	18.89	182	39109	165	103	150
	20080225	9.4	5.89	186670	2655.00	15.14	172	39459	138	137	118
	20070920	21.3	5.96	312480	3115.00	15.20	113	36634	139	138	119
	20071114	19.3	7.68	303000	3582.00	17.14	114	37945	181	186	154
	20071117	23.5	5.58	261660	3044.00	14.85	108	38032	130	125	112
17 to 27	20071117	18.5	7.45	252590	2934.00	18.11	116	38033	168	128	150
	20071118	25.3	7.75	290770	3851.00	17.17	105	38061	183	190	156
	20071118	21.5	6.63	295010	3672.00	15.24	113	38062	161	194	133
	20071118	17.5	7.22	299360	3701.00	16.23	120	38063	169	184	143
	20080311	23.6	6.84	269760	3921.00	15.89	253	39833	163	179	137
27 to 37	20071117	27.3	6.23	237730	2995.00	15.70	104	38031	145	139	125
	20071009	46.9	1.76	141010	1132.00	6.19	88	36951	28	36	23
37 to 47	20071009	43.0	2.47	148950	1427.00	6.97	91	36952	41	62	32
	20071111	47.6	2.70	233120	1809.00	9.36	87	37828	67	91	54
	20080311	58.7	0.51	159700	1036.00	2.88	277	39842	18	54	10
	20080311	62.5	0.87	142360	975.00	4.33	280	39843	26	60	17
47 to 57	20080328	50.2	1.63	191790	1565.00	7.43	274	40036	40	51	33
	20080328	54.7	1.18	172730	1237.00	5.42	277	40037	33	65	24
	20080401	51.3	1.30	199300	1630.00	5.44	274	40138	38	83	26
	20080403	60.4	0.94	148750	1057.00	4.52	279	40186	28	64	19

in array-trigger rate instabilities. A good quality data set was chosen based on two selection criteria, stable FIR temperatures and stable L3 trigger rates. The FIR (far-infrared) pyrometer is connected to the OSS of one of the telescopes and continuously measures the temperature of sky and the presences of clouds. The presence of clouds is noted by a significant rise in temperature, as clouds are significant warmer than the night sky background. The large fluctuations in L3 trigger rates correlates strongly with varying weather conditions due mostly to the presence of clouds whereas steady L3 rates indicates a stable overall array trigger. In this Crab data set only runs with stable FIR and L3 rates were chosen. Short periods of time where runs had large fluctuations in the FIR and L3 rates were cut out. This resulted in a total of 47 runs corresponding to 924 minutes all taken with four telescopes.

4.3   Crab Analysis

The data collected by the VERITAS collaboration was observed in $0.5°$ offset wobble mode (described below) and analyzed with the June 2008 version of GrISU(tah) using the reflected region background mode as described below. GrISU(tah) is the University of Utah's VERITAS group version of GRISU, an analysis package for simulating the development of atmospheric showers and the response of an array of telescopes with a Davis-Cotton design to atmospheric Cherenkov showers as well as tools for displaying VERITAS data. It reads the data in the VERITAS VBF format, processes and analyzes the data using five major programs, for more information on GrISU(tah) see the University of Utah VERITAS group web page http://www.physics.utah.edu/gammaray/GrISU/. In the reflected region background model (see Figure 4.4), the background is estimated using several background regions at the same angular distance and of the same size, from the source region. The advantage of this background method is that the there is no need to add corrections to the acceptance of the camera. The acceptance of a point in the camera being the relative number of candidate gamma-ray events detected at that point compared to the total number of events detected. In our analysis, the signal from the source (the"ON" region) is the number of events with a reconstructed direction less than $0.14°$ from the source direction. While the background rate (the "OFF" region) is estimated using seven background regions with the same area and at the same distance away $(0.5°)$ from the source position. We now examine the results of the detection of the Crab in more details.

4.3.1   Detection

Gamma-rays are selected by applying a set of cuts to parameters that differentiate the desired gamma-ray images from the background images based on the shape and orientation of the shower. The cuts used in the standard analysis are based on the MSL (mean scaled length), MSW (mean
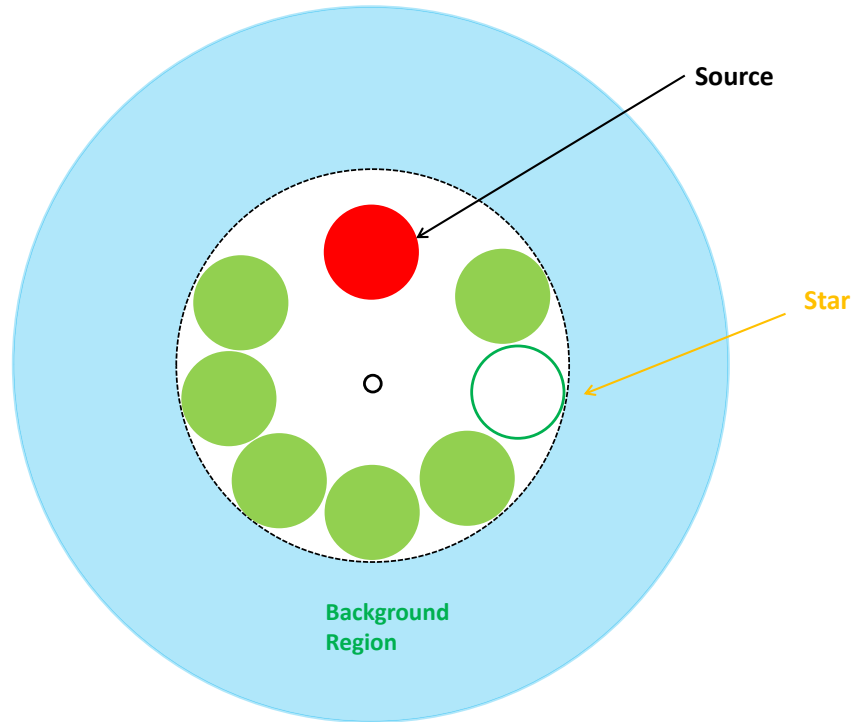
Figure 4.4: An illustration of the reflected background region. The red and green circles represent the source and background regions respectively all located at the same offset from the pointing position (black circle in the middle). The unfilled green circle is an exclusion region around a star not used in the estimation of the background.

scaled width) and theta squared θ^2. These parameters select events that likely came from gamma-rays and originated from a point source and reject background events such as cosmic rays. They involve the characterization of multiple Cherenkov images of the same event seen by different cameras. After these cuts have been applied the next step is to count events which pass the cuts and use statistical tools to examine the statistical significance of any excess events over the background events.

The images of proton showers generally have larger widths and lengths than images due to gamma-ray showers for an equivalent size and distance to shower core values which makes the use of the array image parameters MSL and MSW good for rejecting background events. MSL and MSW are the weighted mean of the image widths and lengths from the four different telescopes. Look up tables produced from Monte Carlo simulations are used in the estimation of MSL and MSW [47]. The mean scaled parameter (MSP) is given by

$$MSP = \frac{1}{N} \sum_{i=1}^{N} \frac{p_i}{\bar{p}_{sim}(\theta, size, r)} \tag{4.1}$$

where N is the number of telescopes, p_i is the parameter of interest, width or length for example, for telescope i and $\bar{p}_{sim}(\theta, size, r)$ is the mean value of the simulation for the given parameter at a given size, impact distance (r) and zenith angle θ [47].

The θ^2 parameter represents the angular distance between the arrival direction of a shower event and the source location. The greater its value the farther away the arrival location is from the source position and so the greater the chance that the shower was not produced by gamma-rays. In Figure 4.5, the red crosses represent the Crab signal and the dashed blue line represents the expected shape of the θ^2 distribution for a point source of that strength. The solid black line represents the estimated background obtained using the reflected region model. The strong signal at small values of θ^2 indicates a γ-ray source. Thus those images whose orientations are consistent with the source location in the sky and are within a region of size θ^2 are classified as "ON" events. As can be seen in the θ^2 plot there is an excess of "ON" events over background evens at lower values of θ^2 indicating the presence of the Crab source.

The excess number of gamma-ray events is define as follows:

$$N_{Excess,\gamma} = N_{on} - \alpha N_{off} \tag{4.2}$$

where N_{on} represents the number of counts in the signal region, N_{off} is the number of background counts and α in this context is a normalization factor between the "ON" and "OFF" regions's
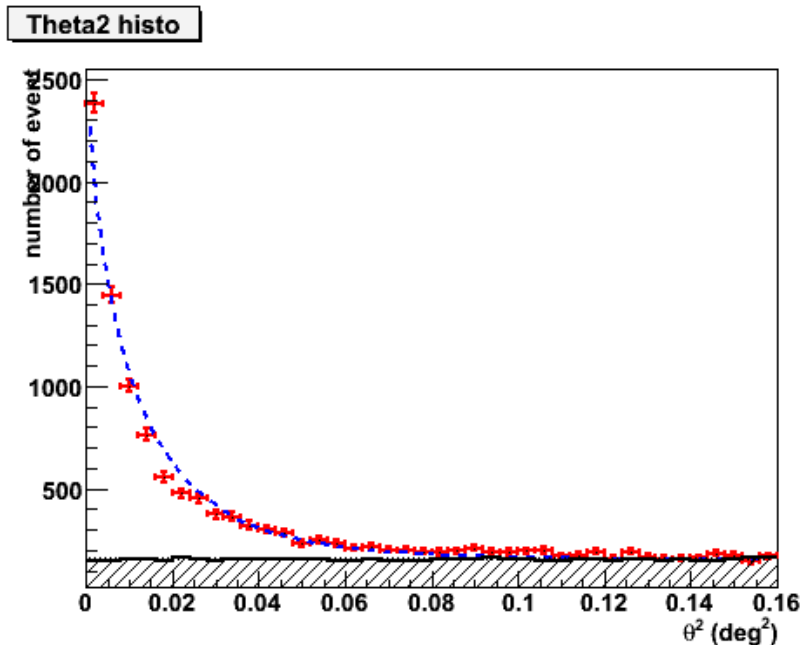
Figure 4.5: A θ^2 plot of Crab data from the 2007-2008 observation season that used the reflected-region background model.

effective exposures that is needed due to the difference in acceptance of these two regions. The alpha factor depends on the observation mode and background estimation model. To first order, the acceptance is a only a function of radial distance from the center of the camera, meaning it is azimuthally symmetric, thus

$$\alpha = \frac{\int_{source} \epsilon(r)dA}{\int_{bg} \epsilon(r)dA} \tag{4.3}$$

where $\epsilon(r)$ is the radial acceptance profile and dA is is the area element in the camera plane. In our case of a reflected background region model we get a simple equation for alpha, $\alpha = \frac{1}{n}$, where n is the number of background regions. This simple relation holds because the acceptance of all the regions is radially symmetric and all regions are observed for an equal amount of time.

After obtaining N_{on}, α and N_{off} we would like to know if $N_{Excess,\gamma}$ is statistically significant and what the rate of gamma rays is for this particular source. The statistical significance (S) of the gamma-ray excess can be calculated according to the Li and Ma equation [48] as follows:

$$S = \sqrt{2}(N_{on} \ln[\frac{(1+\alpha)N_{on}}{\alpha(N_{on} + N_{off})}] + N_{off} \ln[\frac{(1+\alpha)N_{off}}{(N_{on} + N_{off})}])^{1/2} \tag{4.4}$$

It comes from the method of hypotheses testing using the maximum likelihood ratio test. As seen in the 2D significance plot (Figure 4.6), the Crab is detected with a significance of 106 σ. In the field of gamma-ray astronomy it is conventional to require an excess of 5σ for a source to be considered a detection. The significance also tells us how much observation time was required to obtain that particular amount of detection. This can be seen from the significance plot by realizing that the signal and background counts increase linearly with time for a steady source.

Another important measure of the source is the detection rate given in gamma-rays per minute. The gamma-ray emission for the Crab nebula is a quantity that needs to be calculated in order to normalize results of other sources. The gamma-ray rate, R, is calculated as:

$$R_{\gamma} = \frac{N_{on} - \alpha N_{off}}{T} \pm \frac{\sqrt{N_{on} - \alpha^2 N_{off}}}{T} \tag{4.5}$$

Equation 4.4 tell us that the excess of the source is very important in determining the gamma-ray rates which means that determining the background is also a really important component. The larger the background component, the smaller the rate. For our analysis of the Crab Nebula we obtained six gamma-rays per minute. This result can also be seen in the 2d plot showing us a gamma-ray rate for this Crab data set of six gamma-rays per minute (Figure 4.7). Using this same data set we sought out to see how the zenith and azimuth observation angles affect the detection rates for the Crab Nebula.
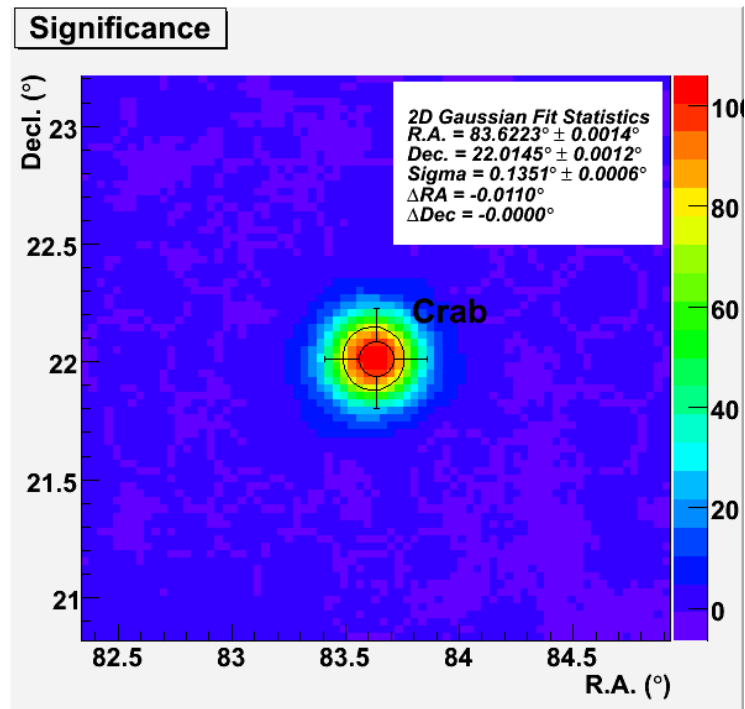
**Figure 4.6**: A 2d significance plot of the Crab Nebula showing a 106 σ detection.
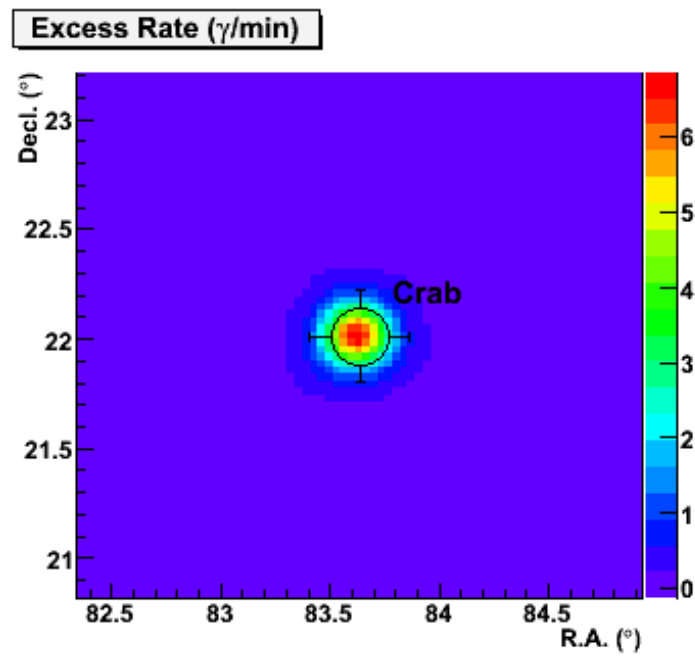
Figure 4.7: A 2d plot of the detection rate for the Crab Nebula showing a rate of 6 γ/min.

4.3.2 The Effects of Zenith and Azimuth Observation Angles
on the Detection of the Crab Nebula

Figure 4.8 and Figure 4.9 illustrate the observed dependence of the gamma-ray detection rate on the zenith and azimuth observation angles. We see that zenith angles that are between $10°$ and $25°$ and azimuth angles are between $110°$ and $230°$ result in the strongest detection rates. Various combinations of azimuth and zenith angles give a large range of observed gamma-ray rates, ranging from as high as 9.3 γs/min to as low as 0.51 γs/min. This is a huge range that strongly affects one's ability to detect a γ-ray source. The highest gamma-ray rate occurs for a zenith angle of $15°$ and azimuth angle equal to $231°$. The lowest rate occurs for zenith angle equal to $59°$ and azimuth angle equal to $277°$. Figure 4.9 tells us that small zenith angles (less than $30°$) give us the highest detection. However, within the small zenith angle range there is about a 3 γs/min range independent of the zenith angle, indicating that there is another variable at play. The higher rates at lower zenith angles can be explained by the fact that observing at larger zenith angles means that the shower development occurred over a longer distance through the atmosphere. This longer distance traveled means that the Cherenkov light is attenuated more and the background rate increases due to an increase in the collection area. As shall be seen in the next chapter, the azimuth observation angle also affects the gamma-ray detection rates because of the Geomagnetic Field (GF). Certain pointing directions align the EAS axis with a stronger GF, which in turn causes the secondary charged particles to be deflected more, thus affecting the cut parameters (width and length) and therefore the gamma-ray rates. Crab data or any other VERITAS data could not be used to study the influence of the GF on the cut parameters width and length because such cut parameters strongly depend on the zenith angle under which observations are carried out. This makes it difficult to separate the GF effect from the evolution of the width and length cuts with different zenith and azimuth angles. In addition we are limited to only those zenith and azimuth angles which the Crab appears in the sky. Furthermore, we seek to know how the energy of the primary-gamma ray affects the cut parameters as well. Therefore, Monte Carlo simulations were used to investigate possible GF effects on the length and width parameters.
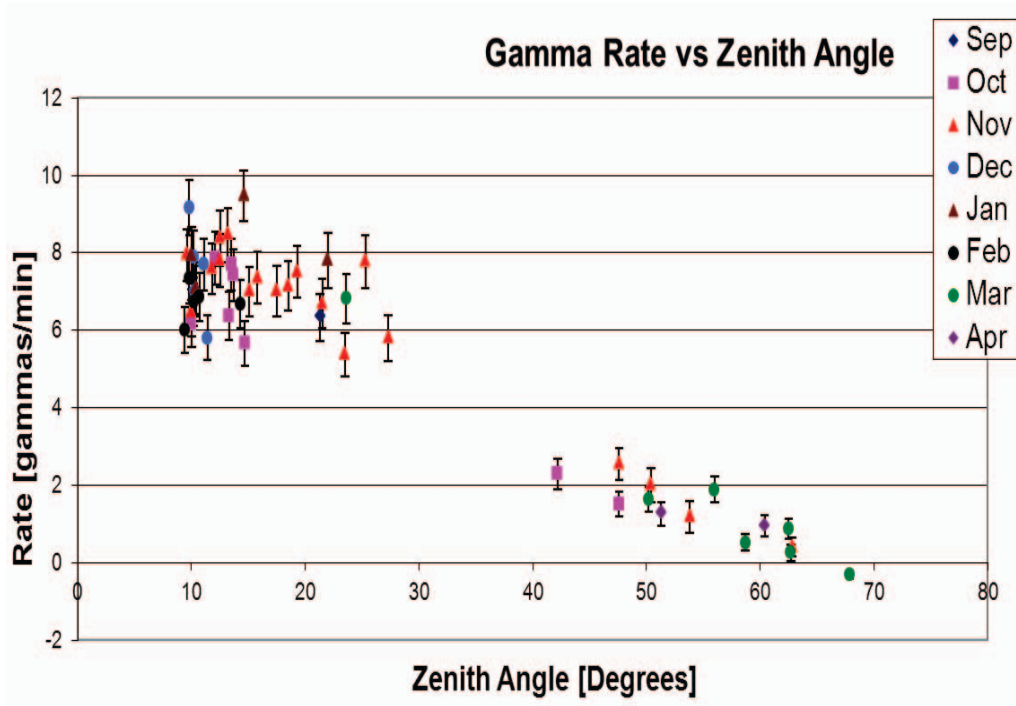
Figure 4.8: Crab gamma ray rates as a function of zenith angle for the 2007-2008 observation season.
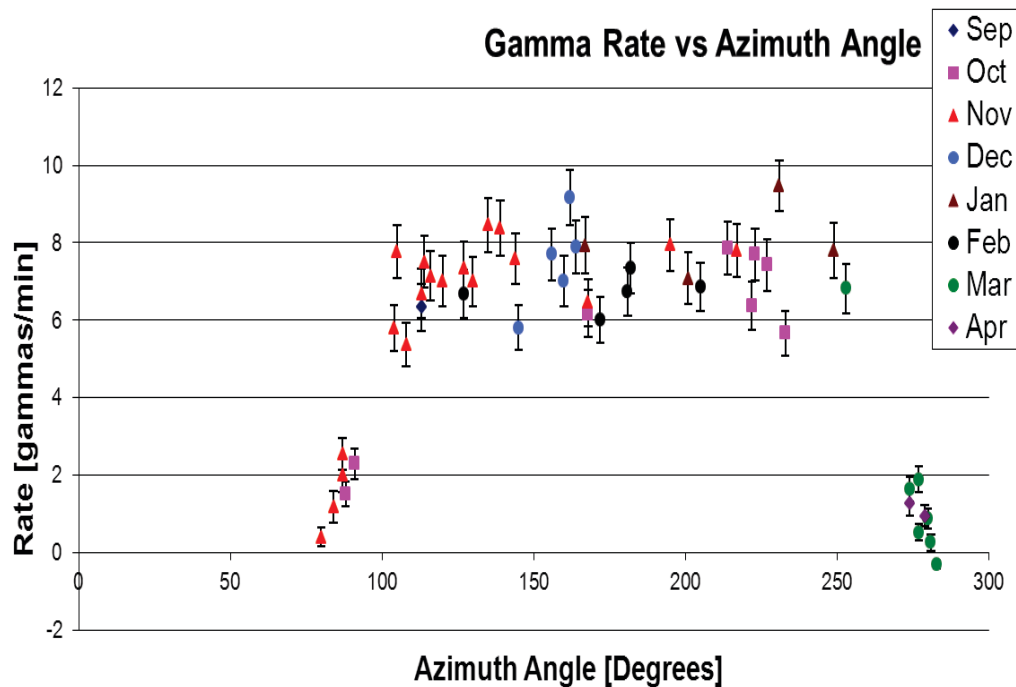
Figure 4.9: Crab gamma-ray rates as a function of azimuth angle for the 2007-2008 observation season. The geographical pointing directions of the telescopes and their corresponding azimuth angles are North (0°), South (180°), East(90°) and West (270°).

CHAPTER 5

GEOMAGNETIC FIELD EFFECTS ON
THE IMAGING TECHNIQUE

In 1953 Guiseppe Concc
oni stated that broadening effects of the geomagnetic field on the lateral development of electron-positron air shower in the atmosphere due to the Lorentz force cannot be negligible in comparison to the displacement due to Coulomb scattering [49]. Thus we seek to investigate how the light sampled by the telescope is affected by the GF.

In this section Monte Carlo simulations are presented to find out the impact that the GF has on the analysis methods used to extract γ-rays from a VHE gamma ray source. First we present a discussion of the models and physics of the Earth's magnetic field followed by plots of the width and length parameters as a function of zenith and azimuth angles and with and without a GF present.

5.1   The Earth's Magnetic Field

The geomagnetic field is a complex and dynamic vector quantity varying both in space and in time. The total observed magnetic field is characterized by three parts $\mathbf{B}_m(\mathbf{r}, t)$, $\mathbf{B}_c(\mathbf{r})$ and $\mathbf{B}_d(\mathbf{r}, t)$ [50]. $\mathbf{B}_m$ is referred to as the main field component and accounts for 95 % of the total field. The main field is created through a dynamo process and it is located in the liquid outer core of the Earth's crust, see Figure 5.1. The $\mathbf{B}_c$ component is sometimes referred to as the lithospheric field. It comes from magnetic minerals in crustal rocks mostly micrometers in size and varies only on geological timescales [51]. The $\mathbf{B}_d$ contribution arises from currents flowing in the ionosphere and magnetosphere regions. The solar wind, a magnetized plasma of charged particles with speeds of about 400 km/s and energies of about 1 keV, is ejected from the upper atmosphere of the sun and is the main contributor to the many charged particles found in these two regions [52]. The solar wind also shapes the Earth's magnetic field by compressing field lines going towards the sun, while stretching field lines on the opposite side that form the so-called Earth's magneto tail. Fortunately for life on Earth, the GF acts like the Earth's shield by bending and inhibiting charged particles from penetrating the atmosphere and reaching the Earth's surface.
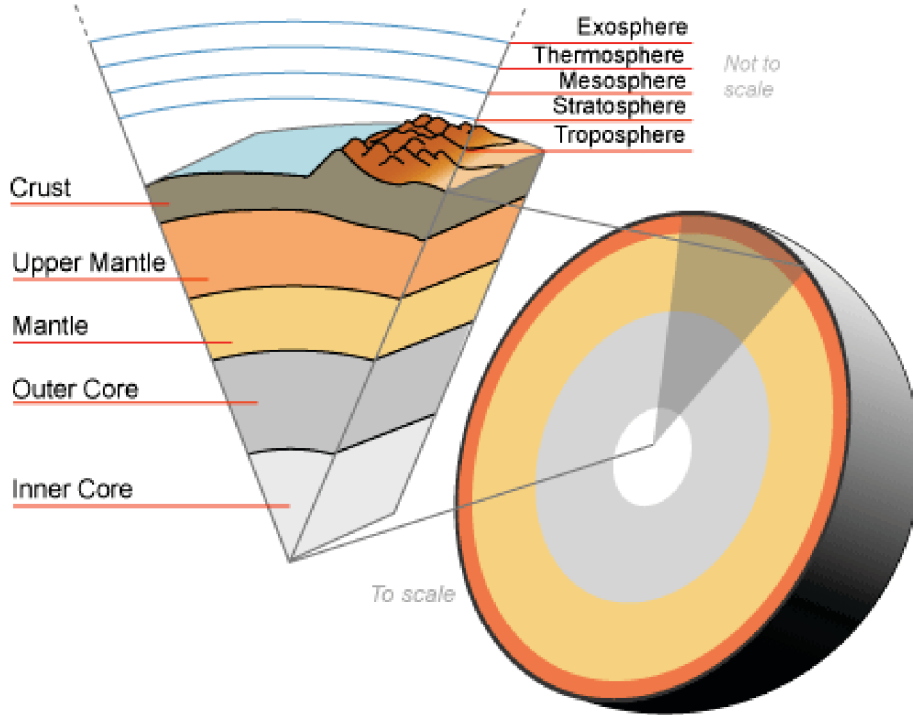
Figure 5.1: An interior slice of the Earth. The main field accounting for 95% of the Earth's magnetic field is found in the outer core of the crust. The two other smaller contributions are found in the crustal rocks and in the atmosphere [53].

In the simplest model, the geomagnetic field can be visualized as a dipole magnet with the magnetic north pole located at the geographic south pole and with its dipole axis tilted from the spin axis of the Earth by about 11 degrees, see Figure 5.2. However, the dipole center does not coincide with the center of the Earth and the magnetic field flips its direction about every 200,000 years. The intensity of this main field can vary from 22 μT to 67 μT according to the US/UK World Magnetic Model (WMM) [50]. Since the magnetic field is a conservative field, it can be derived from the gradient of a magnetic scalar potential V. The spherical symmetry of the GF allows us to express the scalar potential V in terms of spherical harmonics as follows:

$$V(r, \lambda, \varphi) = r_E \sum_{n=1}^{N} \sum_{m=0}^{n} (\frac{r_E}{r})^{n+1} P_n^m(\sin \varphi)(g_n^m \cos(m\lambda) + h_n^m \sin(m\lambda)) \tag{5.1}$$

where r_E is the mean radius of the Earth (6371.2 km) and (r, λ, φ) are the radius, longitude and latitude components in spherical coordinates. g_n^m, h_n^m are the Gauss coefficients and P_n^m is the associated Legendre Functions.

This main field is believed to be generated by a "self excited dynamo" in the liquid part of the outer core [54]. Many simulations of the Earths dynamo have been carried out to understand
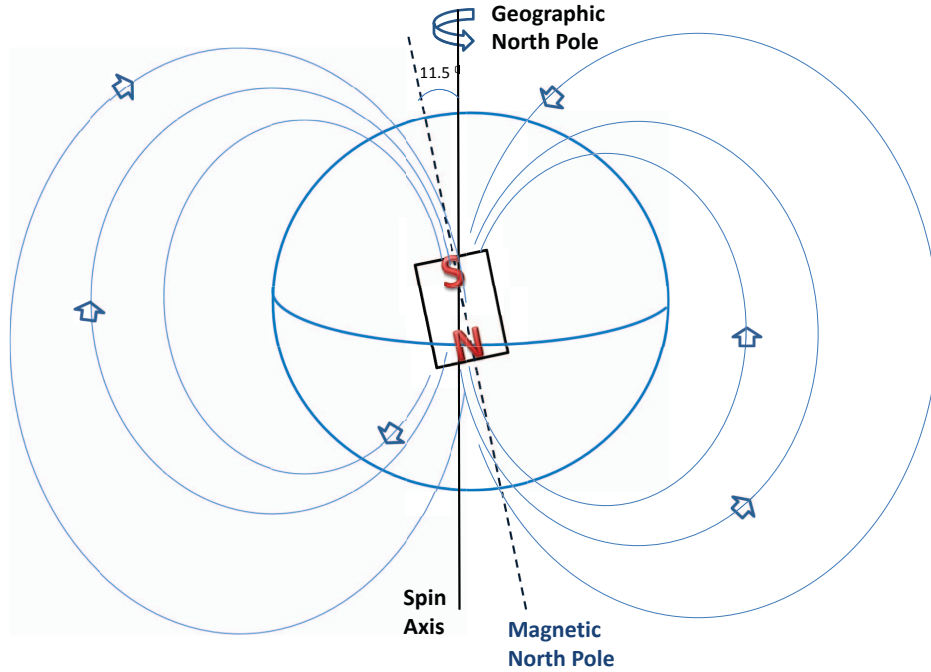
Figure 5.2: A simple model for the geomagnetic field representing it as a dipole magnet. The geographic north pole is located near the magnetic south pole and the spin axis of the Earth is about 11 degrees from the dipole axis.

how it functions but the complexity of the region has forced many of the region's parameters to be set far from the real ones. This is due to the lack of turbulence models for fluids that are both fast rotating and strongly interacting with a magnetic field [55]. The complicated mechanics of this dynamo continues to be an active area of research.

The geomagnetic field vector can be described by the following parameters; total intensity F, X component (northerly intensity), Y component (easterly intensity), Z component (vertical intensity, positive downwards), inclination (or dip) I and declination D. The inclination angle I is the angle between the horizontal plane and the field vector measured positive downwards, as such it is the angle under which the magnetic field lines dip into the surface of the Earth. D is the horizontal angle between true north and the field vector, considered positive east of geographic north and negative when it is west of geographic north. Figure 5.3 shows the decomposition of the GF into total intensity F, north, east and vertical components, X, Y and Z. Various relations can be computed from these variables and angles, some of the most commonly used are found below.

$$F = \sqrt{X^2 + Y^2 + Z^2} = \sqrt{H^2 + Z^2} \tag{5.2}$$

The inclination and declination angles can be calculate as :
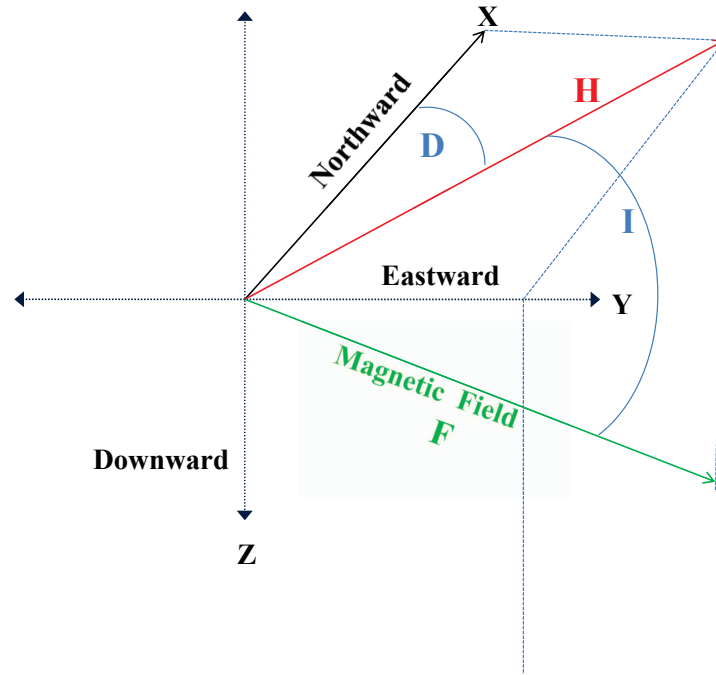
Figure 5.3: The decomposition of the GF into its various components, with total intensity F and north, east and vertical components, X, Y and Z respectively in the WMM reference frame.

$$I = \arctan \frac{Z}{H}, \qquad D = \arctan \frac{Y}{X} \tag{5.3}$$

The north, east and vertical components can be calculated from H and D by :

$$X = H \cos D, \quad Y = H \sin D, \quad Z = H \tan I \tag{5.4}$$

Where H is called the horizontal intensity and points to the magnetic south, while its projection onto the x-axis, X, points to geographic north.

The GF is computed from models that use ground and satellite observations of the total field intensity at many different locations through out the Earth. The two most widely used models are the WMM and the IGRF (International Geomagnetic Reference Field). In the case of the WMM, the GF from 1 km below the Earth's surface to 850 km above the surface can be obtained. Using the WMM's magnetic calculator (2010-2015 epoch), which agrees well with the IGFR model, we can get values for GF at the VERITAS location $(31°40'30''\text{N}, 110°57'07''\text{W})$ and 1268 m a.s.l.. In Table 5.1 we can see the various components and angles associated with the GF for the VERITAS site. The inclination angle of about 58 degrees

Table 5.1: The GF components at the VERITAS site.

WMM	
Northward	24,496.2 nT
Eastward	4476.9 nT
Vertical	40,198.4 nT
H	24,902nT
Total Field	47,286.6 nT
D	$10°21'$
I	$58°13'$

along with the main components of Earth's magnetic field tell us that the GF goes approximately south to north and into the ground.

5.1.1   The Effect of the GF on EAS

The secondary charged particles produced in an EAS are acted on by the Lorentz force due to the GF. These particles give rise to most of the Cherenkov photons in gamma-ray initiated showers and are composed mainly of electron/positron pairs. As the Lorentz force acts on oppositely charged particles the GF is expected to laterally broaden the EAS as it modifies the electron and positron distribution around the core of the shower. Thus the distribution of Cherenkov photons on ground will also be changed. The Lorentz force depends on the zenith and azimuth angles of the gamma-rays's shower direction and the various magnetic field components. KASCADE's coordinate system uses a ground coordinate system with z(down), y(South) and x(East). Since the telescope points to the opposite azimuth direction to the particle momentum direction, the telescope pointing directions N,E,S,W correspond to azimuth angles of 180°, 90°, 0° and 270°, respectively, in the KASCADE coordinate system, see Figure 5.4.

$$\vec{F} = q(\vec{v} \times \vec{B}) = \frac{q}{m}(\vec{p} \times B) \propto \vec{B}_\perp \tag{5.5}$$

$$\vec{B}_\perp = B_z \sin(\theta)\sin(\phi)\hat{\mathbf{i}} + [B_x \cos(\theta) - B_z \sin(\theta)\cos(\phi)]\hat{\mathbf{j}} - B_x \sin(\theta)\sin(\phi)\hat{\mathbf{k}} \tag{5.6}$$

Here $\vec{B}_\perp$ is the component of the magnetic field strength perpendicular to the direction of movement of the particle, $\vec{p}$ denotes the momentum of the particle, θ and ϕ correspond to the azimuth angle and the zenith angle under which the particle is traveling. We can explore which directions will be affected the most by plotting $\vec{B}_\perp$ as a function of zenith and azimuth angle. From Figure 5.5 we see that the maximum influence of the GF on EAS occurs when the telescope points to the north (azimuth angle equal to 180 degrees) and for zenith angles ranging from 50° to 75°, while the minimum effect occurs when the telescope points to the south (azimuth angle equal
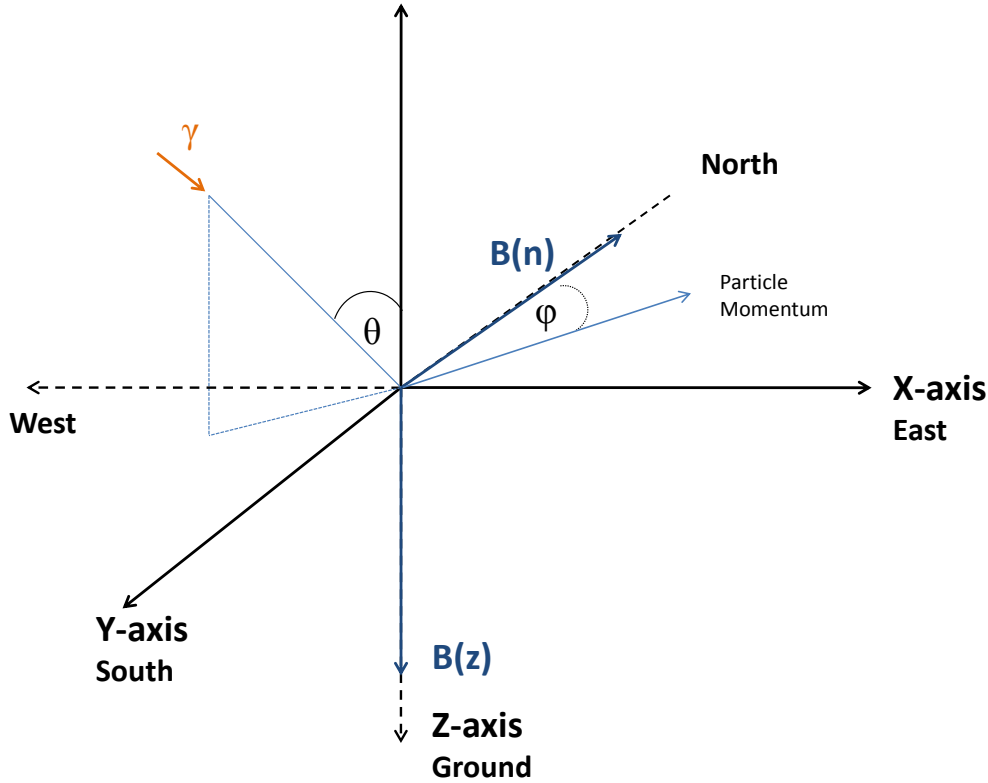
Figure 5.4: Coordinate system of the Earth's magnetic field (B) together with the KASCADE and the WMM reference frame.

to zero degrees) and for zenith angles ranging from 25° to 35°. When the telescope points close to zenith there is barely any difference in the $\vec{B}_\perp$ strength between the different azimuth directions. An interesting feature of this plot is that the $\vec{B}_\perp$ is symmetric in azimuth angle. Furthermore, large zenith angle observations are not necessarily more affected by the GF than observations carried out at low zenith angles. Thus we will search for the maximum and minimum effect at the two pointing directions of north and south. However, matters are complicated by the fact that image parameters suffer from a geometric effect due to different zenith angles that will have to be separated from the GF effect in our analysis. In order to make matters simpler the reference frame is usually chosen such that the y-component of the GF vanishes. This leaves us with two components; the horizontal component H (north component X) and vertical component Z.

5.2   The Monte Carlo Simulations

All simulations were done using the program KASCADE (KArlsruhe Shower Core and Array DEtect) [56]. The KASCADE atmospheric shower production code uses Monte Carlo methods
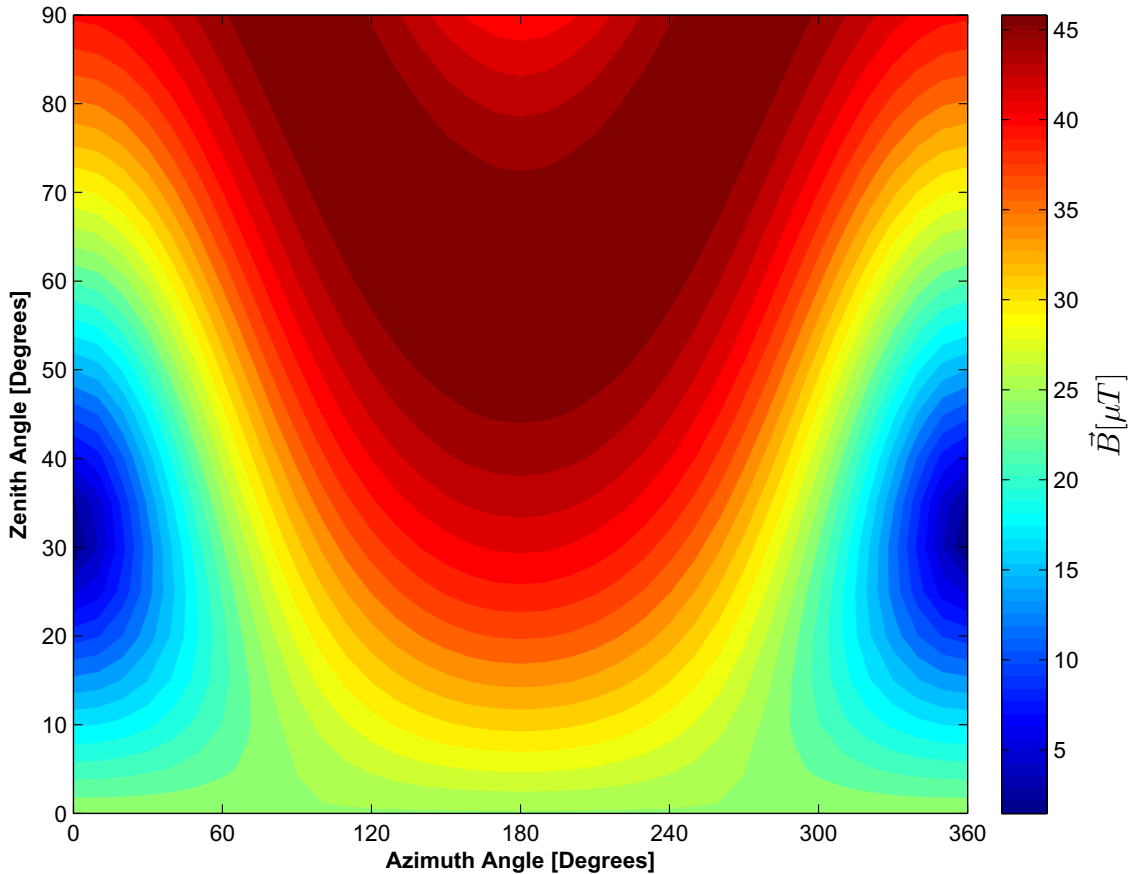
Figure 5.5: This contour plots shows the component of the GF perpendicular to the direction of movement of the particles as a function of zenith and azimuth angles. It shows that the maximum and minimum effects of the GF occur for azimuth angles equal to and near to 180° and 0° respectively . This corresponds to telescope pointing directions of north and south.

to initiate and analyze EAS produced by different gamma-ray primaries of varying energies with different incoming directions as well as producing showers embedded in an atmosphere with or without a magnetic field. Kascade uses a ground coordinate system with z(down), y(South), and x (East) where the x-axis is perpendicular to the Earth's magnetic field. The input file kascade.pilot allows you to change the various reconstruction parameters such as particle type (including gamma-rays), minimum and maximum energy of the primary particle, threshold energy in MeV, total number of shower, a magnetic field option and others.

MC simulations were used to produce several different kinds of plots of the length and the width cut parameters in the presence and absence of a GF. Plots were made for various zenith angles, azimuth angles and primary gamma-ray energies. The zenith angles were varied from 10 degrees to 50 degrees in increments of 5 degrees. The azimuth angles were varied from 0 degrees

to 180 degrees in increments of 45 degrees. The energies of the primary gamma-ray used were 400 GeV, 800 GeV, 1.6 TeV, 3.2 TeV and 6.4 TeV. This sensitivity study then resulted in a correction to the length and width parameters due to variations in zenith angle.

5.2.1   Simulations with No Geomagnetic Field

First simulations with no GF were generated to see how the length and width parameters behave without the effect that the GF has on the charged particles of the shower. For each of the five gamma-ray primary energies we fixed the azimuth angle, due to the isotropic nature of the shower development in the absence of a magnetic field with respect to azimuth angle, and varied the zenith angle as described above for a total of 45 simulations. At each energy level length and width plots were made as a function of zenith angle. The function $p1 * Cos(\theta) + p0$ was found to fit well the graphs produced from the simulations with no GF. Each simulation was ran with 20,000 showers and with a maximum impact parameter of 500 meters. The impact parameter is measured from the center of the array in a plane perpendicular to the direction of the source. The minimum impact parameter was always set to zero meters. In all simulations the telescope axis is parallel to the shower axis. Figures 5.6 to 5.10 show simulations with no magnetic field and the corresponding fit parameters for the width and length of the image as a function zenith angle. One can see that the fit works well for energies up to 1.6 TeV afterwards the fits run into the problem of large error bars due to low statistics.

Another feature of the simulations with no GF is that the width and length parameters increase with energy for the same zenith angle. This is a phenomenological effect generated by the fact that higher primary gamma-rays initiate EAS closer to the ground, which in turn produce shower maximums closer to the telescopes. This increases the angular size of the shower images, hence giving larger width parameters. Furthermore, higher primary gamma-ray initiated EAS produce more secondary particles. This increases the longitudinal extent of the EAS, thus resulting in larger length parameters. The overall decrease in the length and width parameters as the zenith angle increases is due to a geometric effect. As the zenith angle increases the line-of-sight distance to the shower maximum increases which decreases the projected dimensions of the (length and width) image parameters. This effect is particularly strong at larger zenith angles (greater than 30 degrees) as depicted in Figure 5.11. This can also bee seen by observing that when the telescopes points straight up the projection of the images on the ground coordinate system is that of a circle, whereas when the zenith angle increases the projection becomes that of an ellipse. Another interesting feature of the graphs is that the width and length parameters decrease more rapidly for lower energy primaries (400 Gev and 800 Gev) than for the remaining, higher energy primaries. An overall pattern is not clear from the graphs but there does seem to be individual patterns in
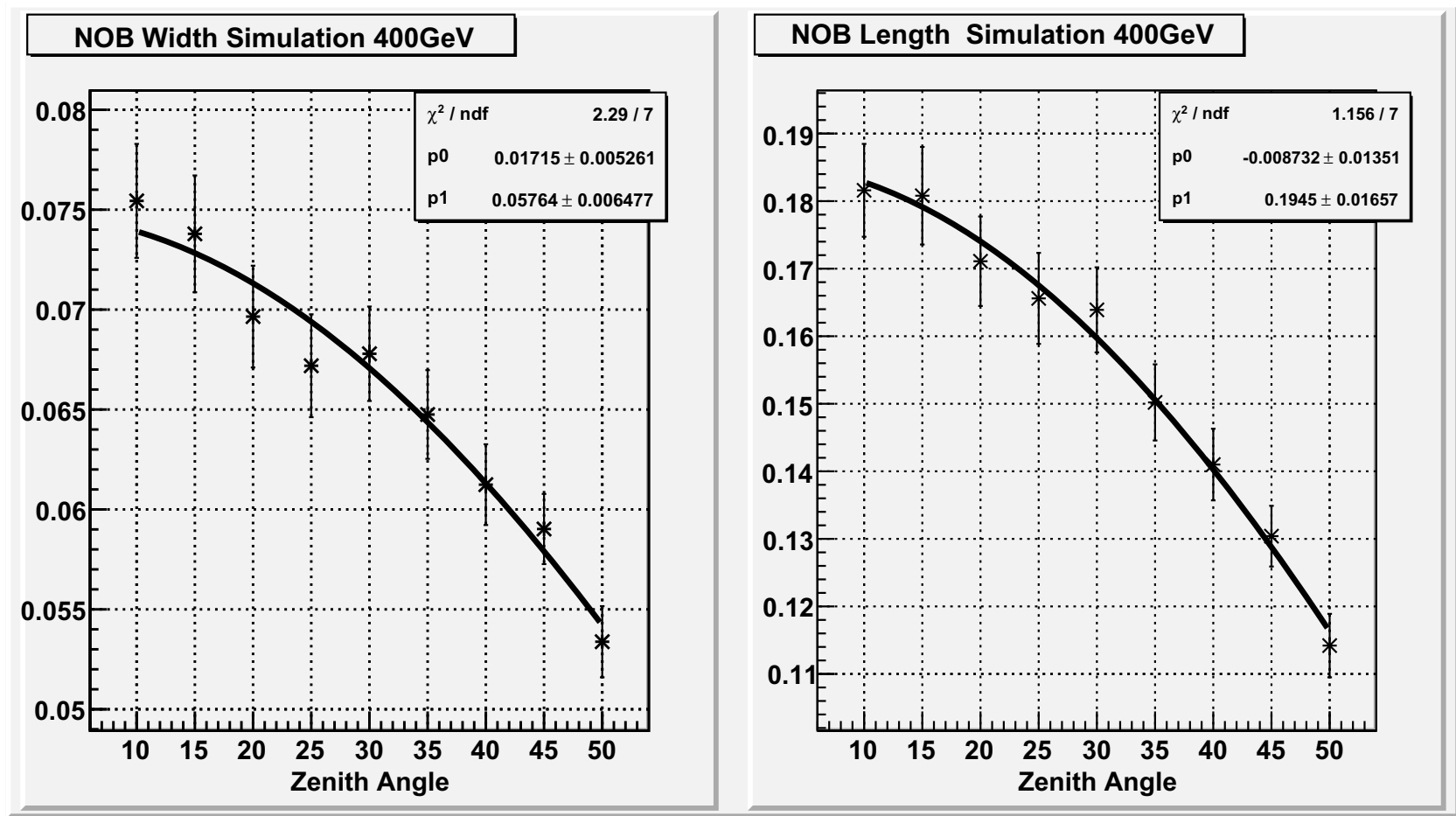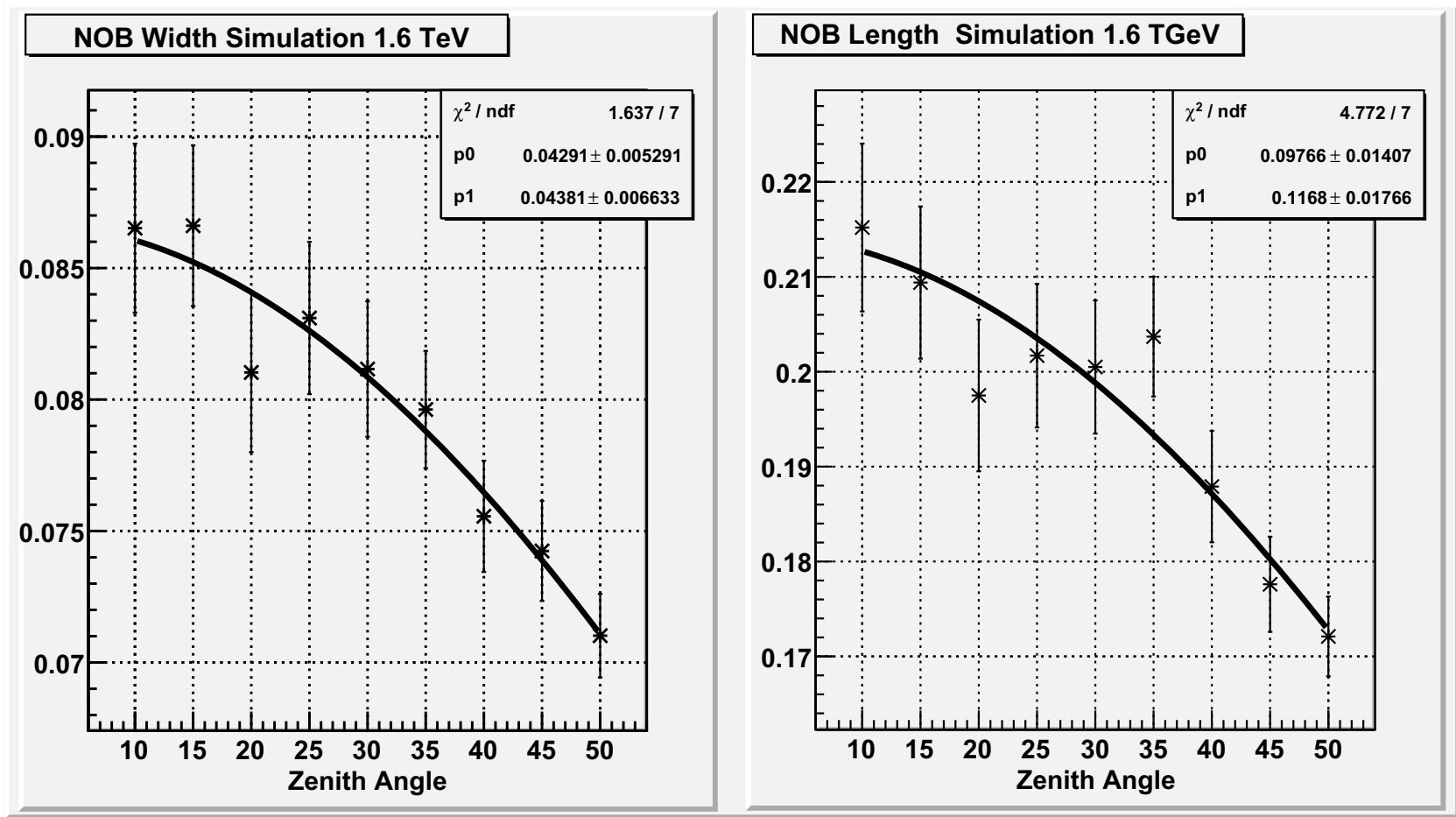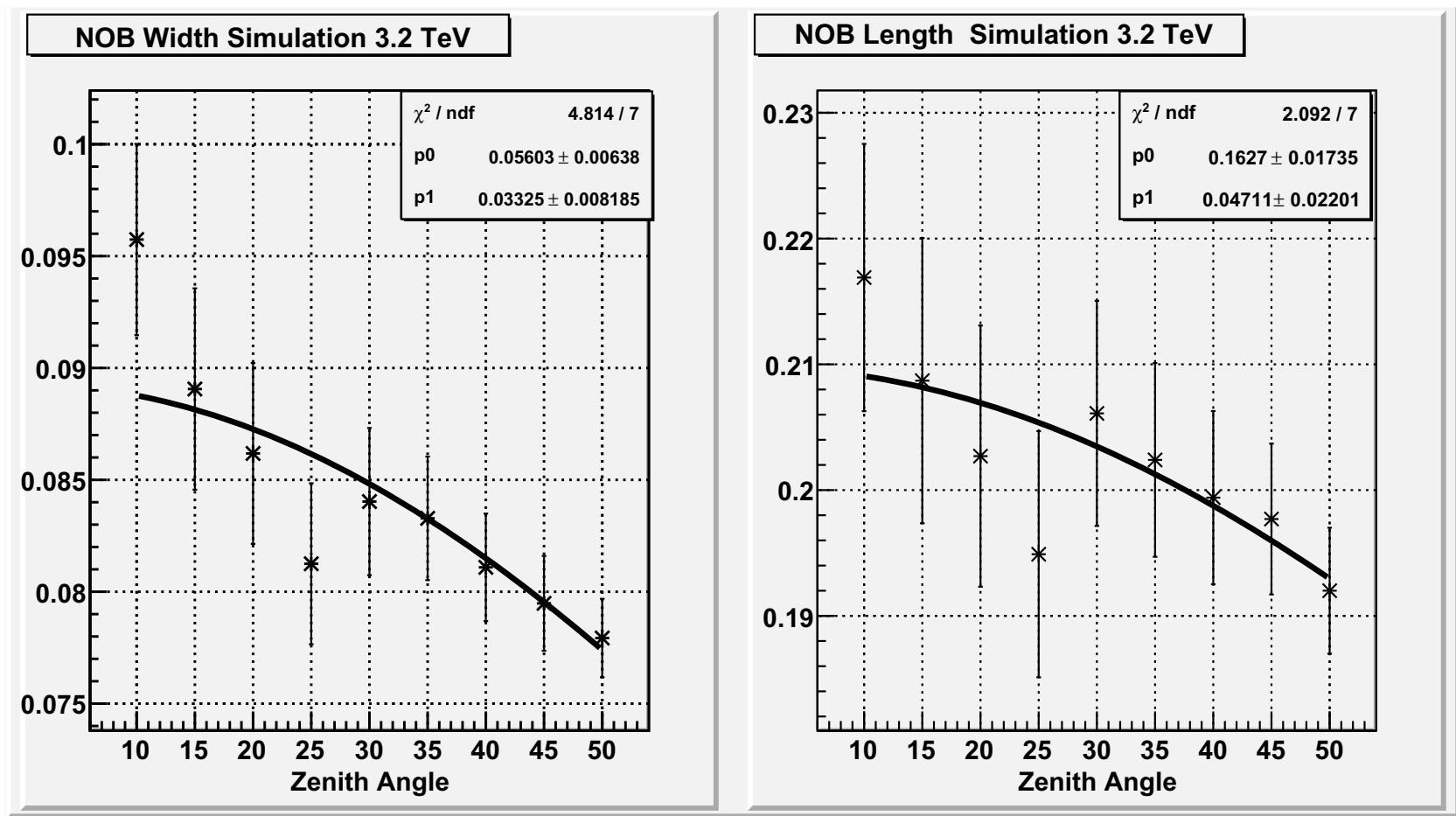
Figure 5.6: The width (left) and length image parameters as a function of zenith angle with no GF present. The primary gamma-ray had an energy of 400 GeV.
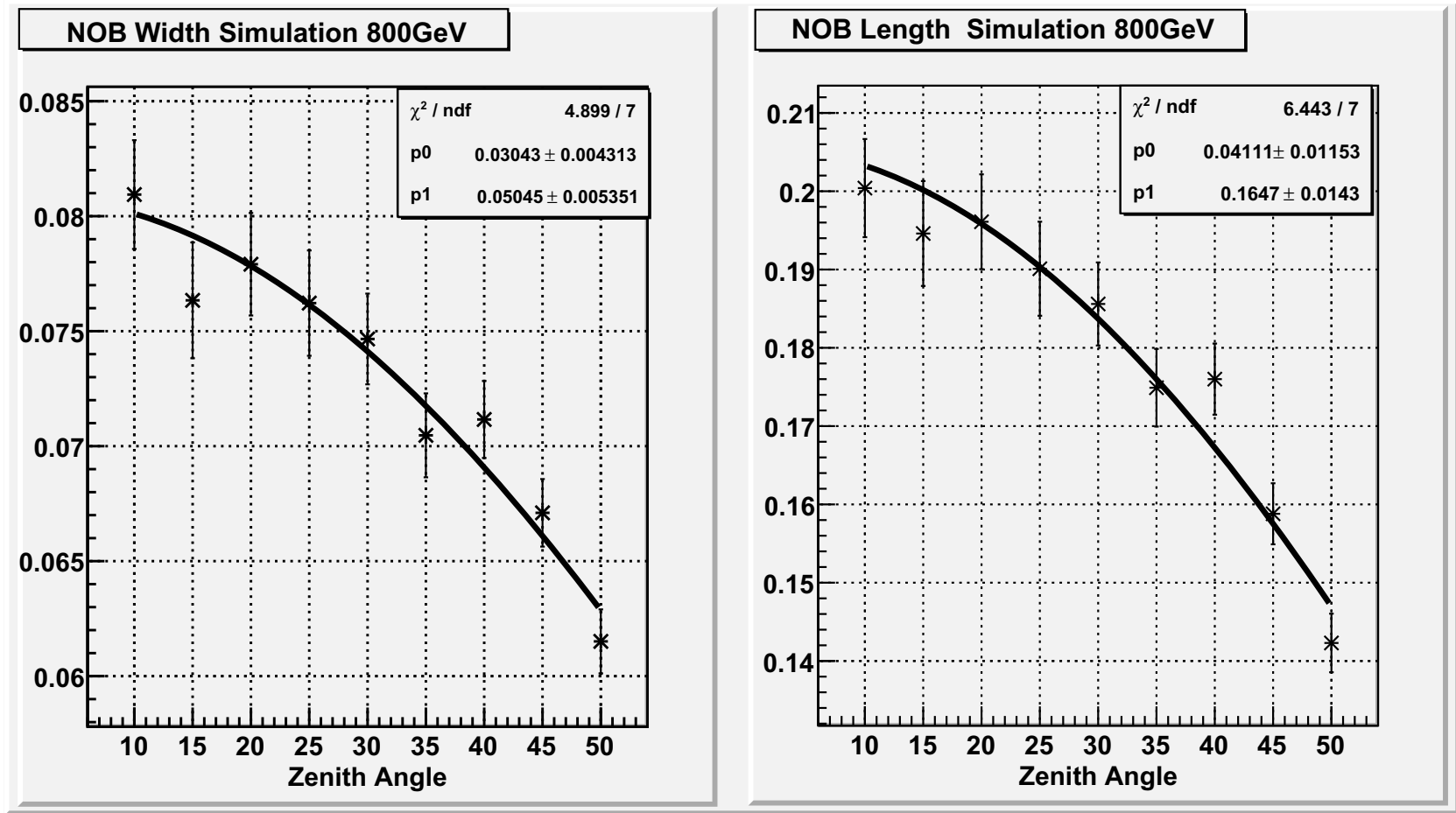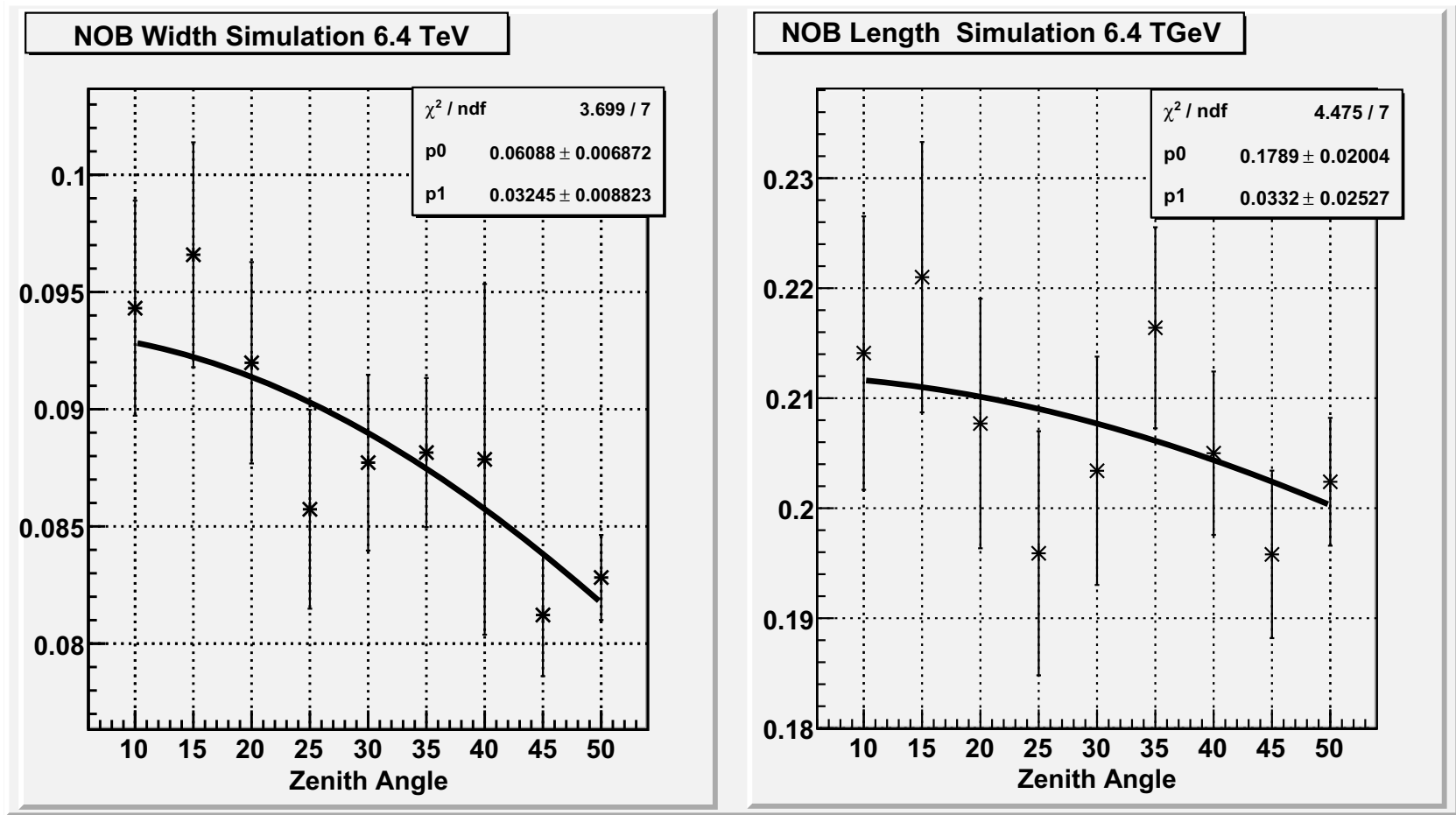
Figure 5.7: The width (left) and length image parameters as a function of zenith angle with no GF present. The primary gamma-ray had an energy of 800 GeV.

Figure 5.8: The width (left) and length image parameters as a function of zenith angle with no GF present. The primary gamma-ray had an energy of 1.6 TeV.

Figure 5.9: The width (left) and length image parameters as a function of zenith angle with no GF present. The primary gamma-ray had an energy of 3.2 TeV.

Figure 5.10: The width (left) and length image parameters as a function of zenith angle with no GF present. The primary gamma-ray had an energy of 6.4 TeV.

each of the two graphs of the width and length parameter as a function of zenith angle at each primary energy. For the 400 GeV and 800 GeV cases and for the length parameter there is a faster and smoother decrease with increasing zenith angle when compared to primary energies above 1600 GeV. These higher energy primaries tend to have a small decreasing trend accompanied by larger fluctuations. As for the width parameter, the lower energy primary energies of 400 GeV and 800 GeV also have a decreasing and somewhat smooth trend like in the case of the length parameter, but the decrease is less dramatic. The higher primary energy width parameters have a decreasing trend and a smoother behavior than for the length parameters. The lack of an overall pattern and the erratic behavior occurring at each of the primary energies, especially at primary energies greater than 800 Gev, are consisted with intrinsic fluctuations in the EAS. In general at the lowest energies, the images are control by the camera's F.O.V and so they can be seen at a larger distance. At higher energies, the image falls outside of the F.O.V and is not trigged. Thus you expect there not to be much of a zenith angle dependence at higher energies and as all the showers will be at about the same distance.

Correlations between the length and width parameters can be explored in the graph of the ratio of width to length. The error bars for the graph are rather large, due to the additive property of errors, but some overall trends do appear. In the case of lower energy levels, 400 GeV and 800 GeV, the width and length change approximately identically for zenith angles equal to 30 degrees or less. For zenith angles equal to 35 degrees and higher the ratio gets a bit larger indicating that the image is becoming less elongated because the length parameter is decreasing at a faster rate than the width parameter. In the case of 3.2 TeV and 6.4 TeV the ratio of the parameters tends to decrease slightly whereas the 1.6 TeV energy level seems to remain constant for the smaller zenith angles and increase for larger zenith angles (greater than 35 degrees). Therefore, it can be concluded that the geometric effect is greater for larger zenith angles, greater than 30 degrees, and it affects the length parameter more than the width parameter for the higher zenith angles. Visually this is shown by the jump in values of the width/length parameters at zenith angle equal to 35 degrees as seen in Figures 5.11 and 5.12.

5.2.2   Simulations with a Geomagnetic Field Present

In the simulations with a GF present a total of 225 simulations were generated. The azimuth angle was varied in increments of 45 degrees from 0 degrees to 180 degrees. Each simulation was ran with 1,000 showers, with a maximum impact parameter of 500 meters and the minimum impact parameter was set to zero meters. The correction function $p1 * Cos(\theta) + p0$ obtained at each of the five primary energy simulations with no GF was applied as a correction factor to its corresponding primary energy simulation with a GF present. Plots of simulations with a GF, employing the
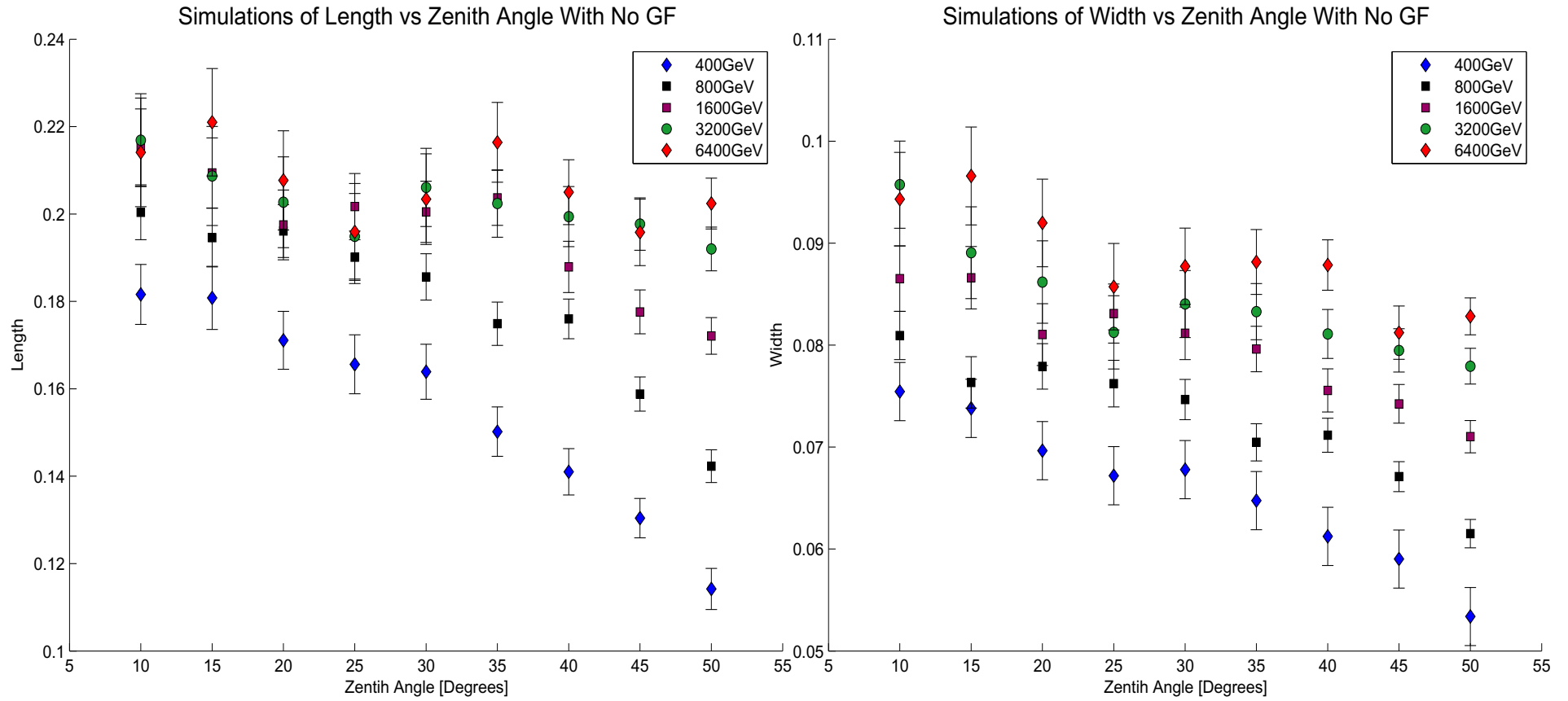
Figure 5.11: These two graphs show the changes in length (left) and width (right) as a function of zenith angle at each of the five energy levels.
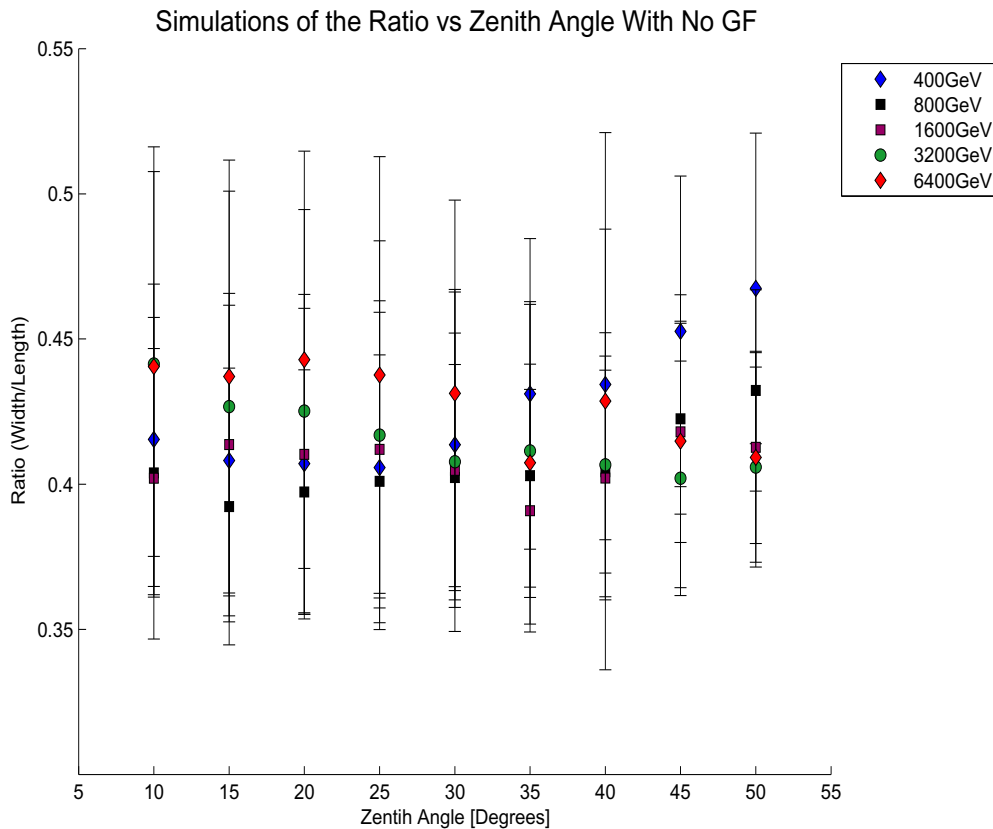
Figure 5.12: A graph of the ratio of width to length as a function of zenith angle for the various energy levels.

correction factor, were compared with plots with no GF to look for additional GF induced effects. Plots of the width and length parameter as a function of zenith angle with and without a magnetic field were superimposed to examine the dependence of the image parameters as a function of azimuth angle.

The first set of Figures 5.13 to 5.17 combines the simulations of the width and length parameters with a GF and without a GF. These plots were made for a fixed energy level and all azimuth angles were plotted in one graph in order to show in which direction (azimuth angle) the image parameters length and width are affected most by the GF. For the lowest primary energy (400 GeV) it is clear that the showers originating in the south (azimuth angle = 0) are affected the least: the GF simulations are almost identical to the simulations with no GF. Showers originating from other directions exhibit substantial changes in average length and width when compared to simulations with no GF. This result is in agreement with the fact that the magnetic field has a global minimum
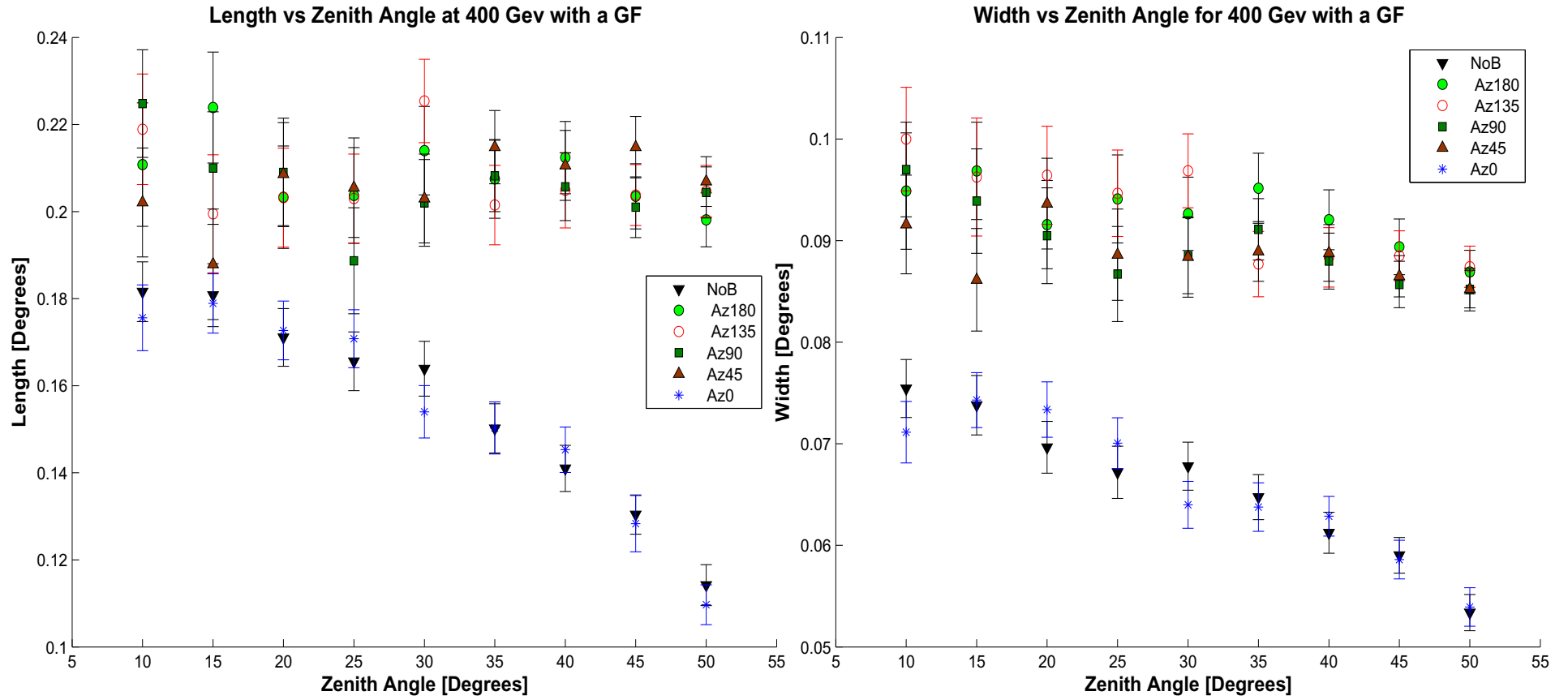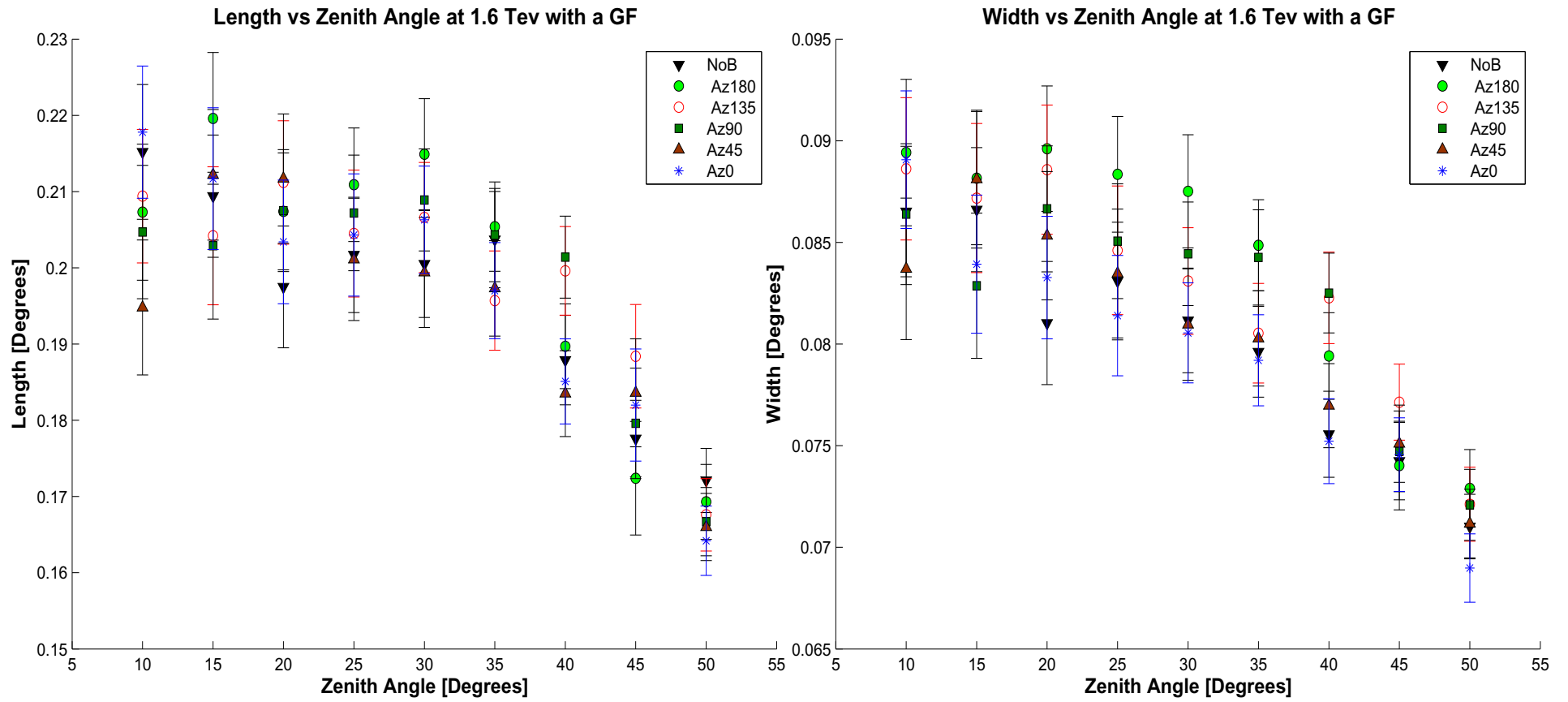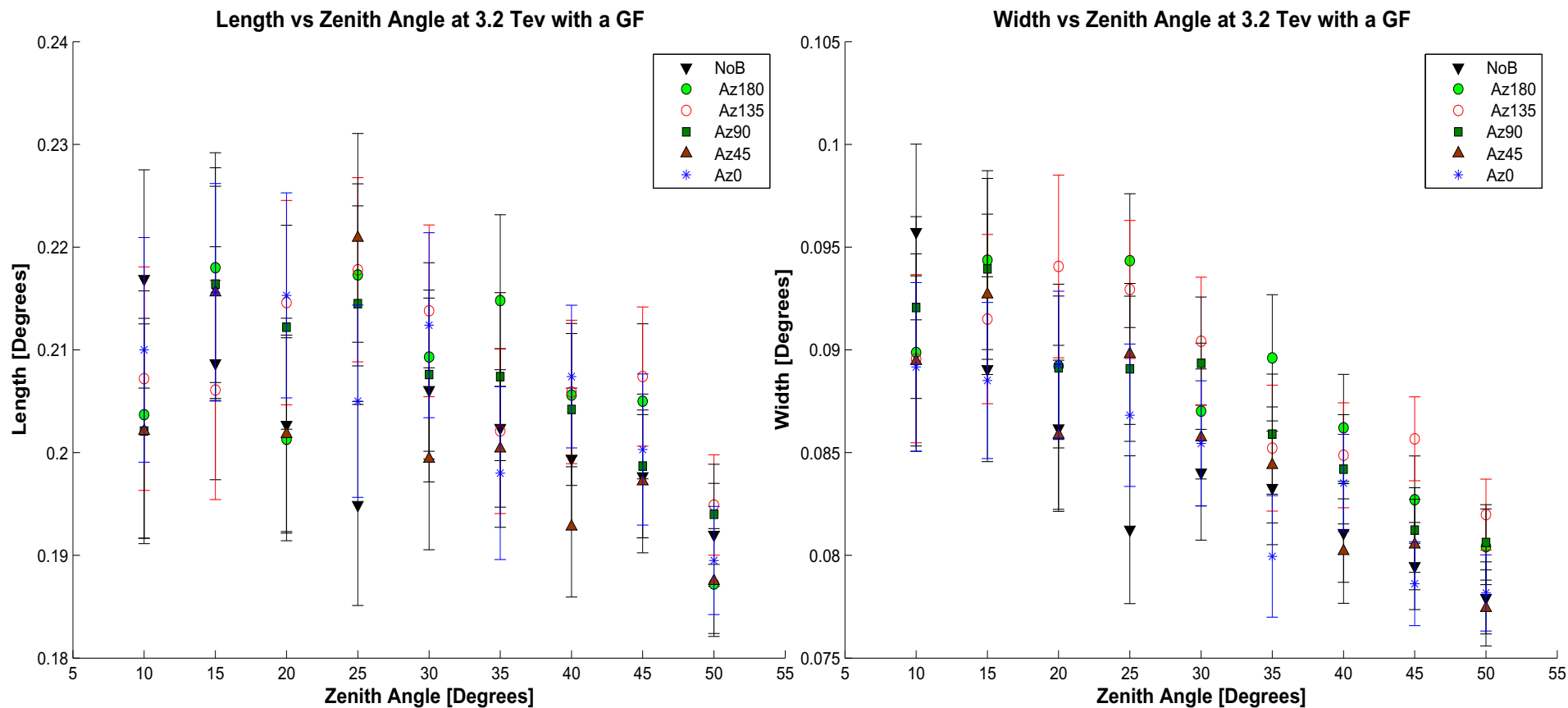
Figure 5.13: These graphs of the length (left) and width parameter versus zenith angle show both the simulations with the GF and without the GF for a fixed energy level, in this case 400 GeV, and all azimuth angles.
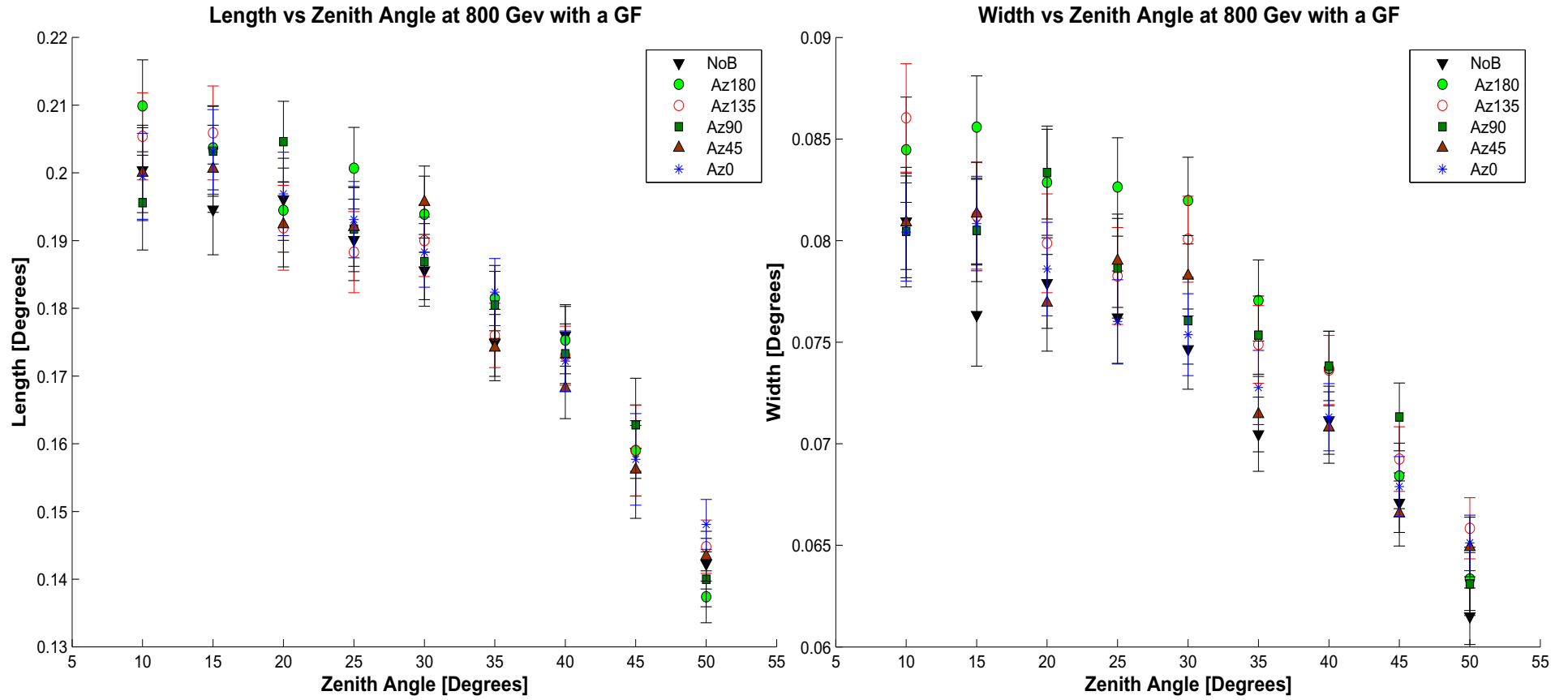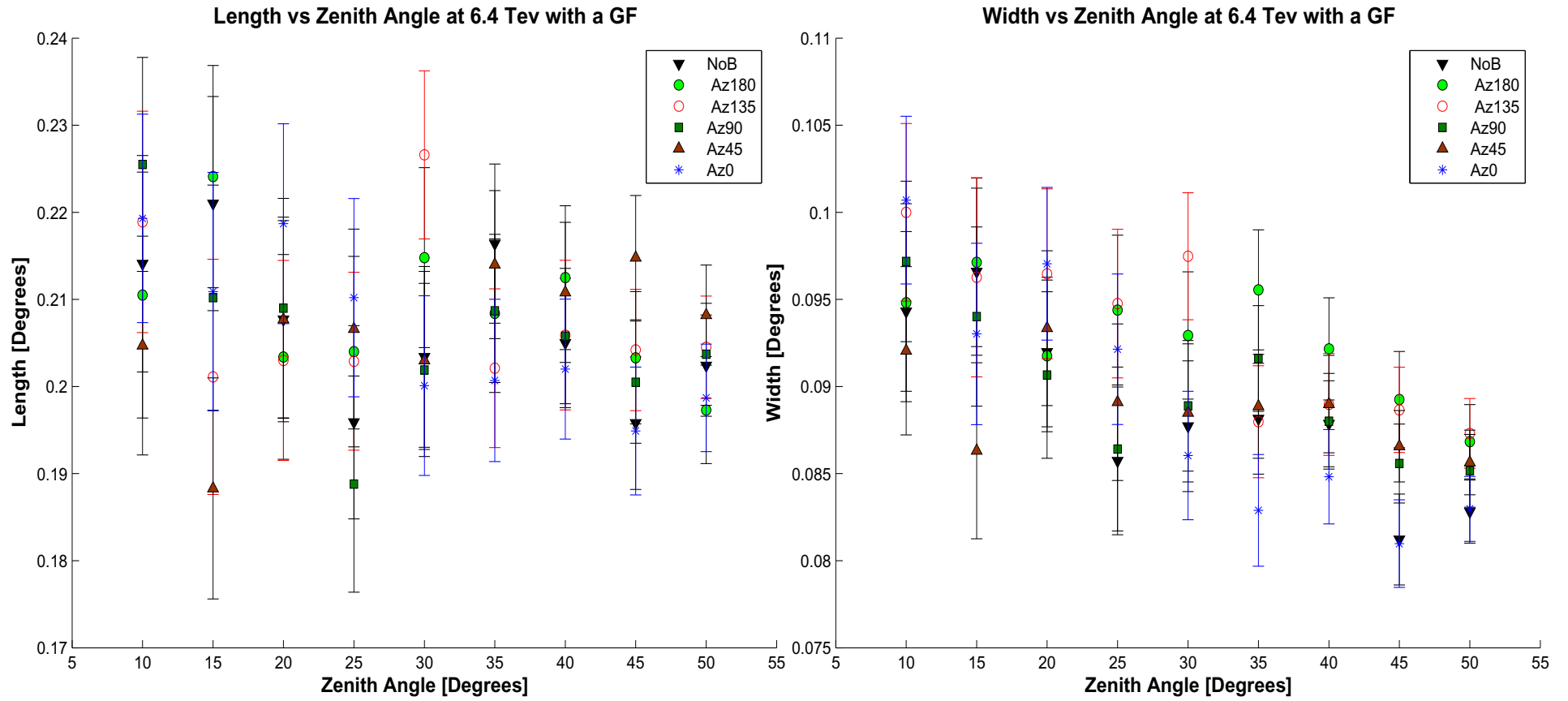
Figure 5.14: These graphs of the length (left) and width parameter versus zenith angle show both the simulations with a GF and without a GF for a fixed energy level, in this case 800 GeV, and all azimuth angles.

Figure 5.15: These graphs of the length (left) and width parameter versus zenith angle show both the simulations with the GF and without the GF for a fixed energy level, in this case 1.6 TeV, and all azimuth angles.

Figure 5.16: These graphs of the length (left) and width parameter versus zenith angle show both the simulations with a GF and without a GF for a fixed energy level, in this case 3.2 TeV, and all azimuth angles.

Figure 5.17: These graphs of the length (left) and width parameter versus zenith angle show both the simulations with a GF and without a GF for a fixed energy level, in this case 6.4 TeV, and all azimuth angles.

and local minimums at azimuth angle equal to zero degrees for any given zenith angle as seen in Figure 5.5.

In the case of 800 GeV the length parameter does not change much due to GF effects, but the width parameter is somewhat more affected. The width parameter changes most for azimuth angle equal to 180 degrees but only for zenith angles less than 35 degrees. For zenith angles greater than 35 degrees the geometric effects dominate the GF effects. Thus simulations with and without a GF for 800 GeV are similar for zenith angles greater than 35 degrees, but the values of the width parameters are systematically higher for cases with a GF. As for the higher (greater than 800 GeV) primary energy simulations the length and width parameters for the case of azimuth angle equal to 180 degrees are larger in value than for other azimuth angles. However, all values of the length and width systematically fall within the error bars of the simulation with no GF. The observed milder dependence may be due to two factors. First is that higher energy primary gamma-rays initiate EAS closer to the ground thus giving the GF less time to act on the secondary charge particles. The low simulation statistics from EAS initiated by higher energy primary gamma-rays also increases the error bars.

For 1.6 TeV and higher primary energy simulations and zenith angles equal to 10 and 15 degrees, the simulations with no GF tend to have a systematically larger width/length than those with a GF. For the other zenith angles ($\theta > 15°$) the simulations with no GF tend to be systematically smaller than those with a GF. This again is probably due to the fact that showers initiated at larger zenith angles traverse more atmosphere than those with smaller zenith angles thus giving the GF more time to spread out the EAS particles.

In Figures 5.18 to 5.22, graphs of the width/length parameter versus zenith angles for fixed azimuth angles and for all primary energy simulations were made to illustrate how the GF effects varied with energy. As we see in these figures, the GF effect is strongest for azimuth angle equal to 180° and weakest for azimuth angle equal to zero degrees. This effect is particularly strong at 400 GeV for the simulations of azimuth angle of 180°. The mean percent difference for the width and length are 34% and 30% respectively for azimuth angle equal to 180°. The width mean percent difference for simulations with and without a GF for azimuth angles equal to 0°, 45°, 90° and 135° are 3%, 30%, 31%, 34%, respectively. For the length the mean percent difference for simulations with and without a GF for azimuth angles equal to 0°, 45°, 90° and 135° are 3%, 29%, 29%, 29% respectively. Although these numbers are almost equal to the ones for the width parameter it is worth noting that the largest contribution to the mean percent difference came for zenith angle of 50 degrees which give percent differences between 50% and 57% for all azimuth angles with the exception of azimuth angle equal to zero degrees. As for the width parameter the differences are
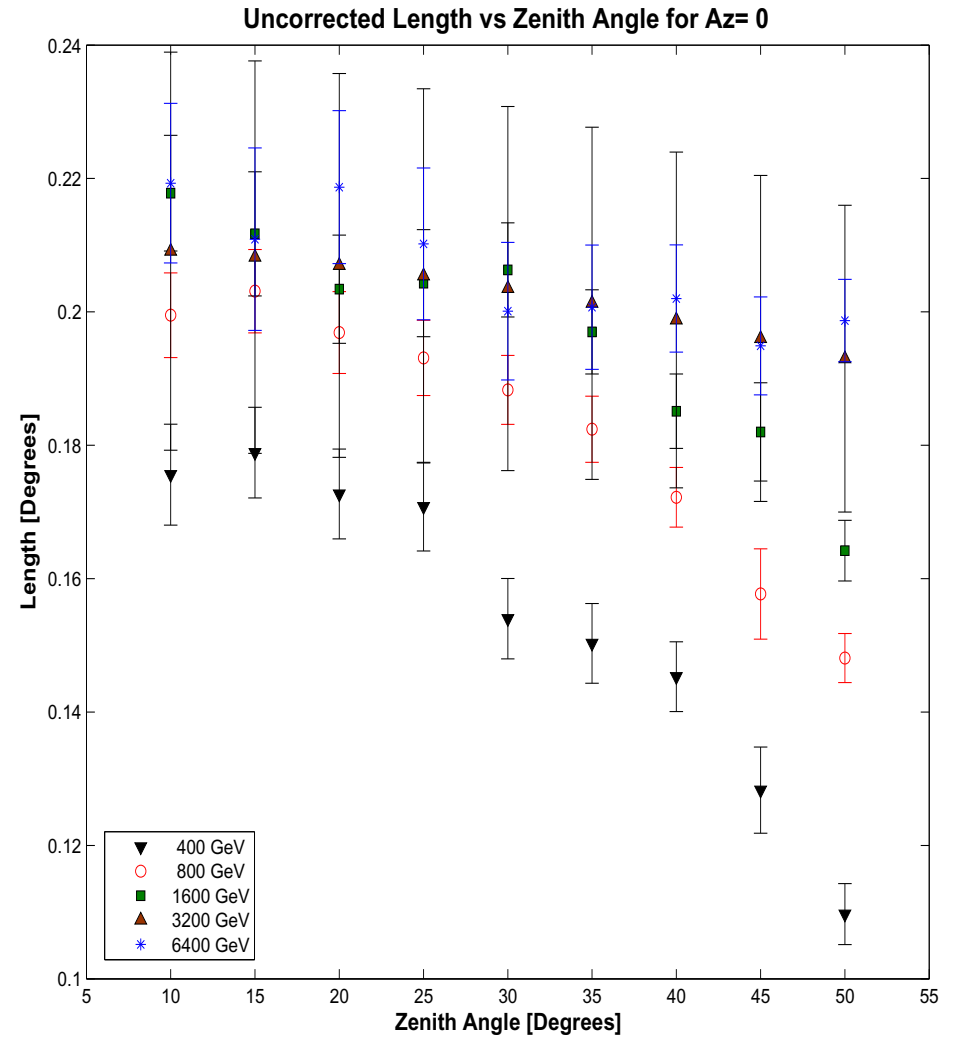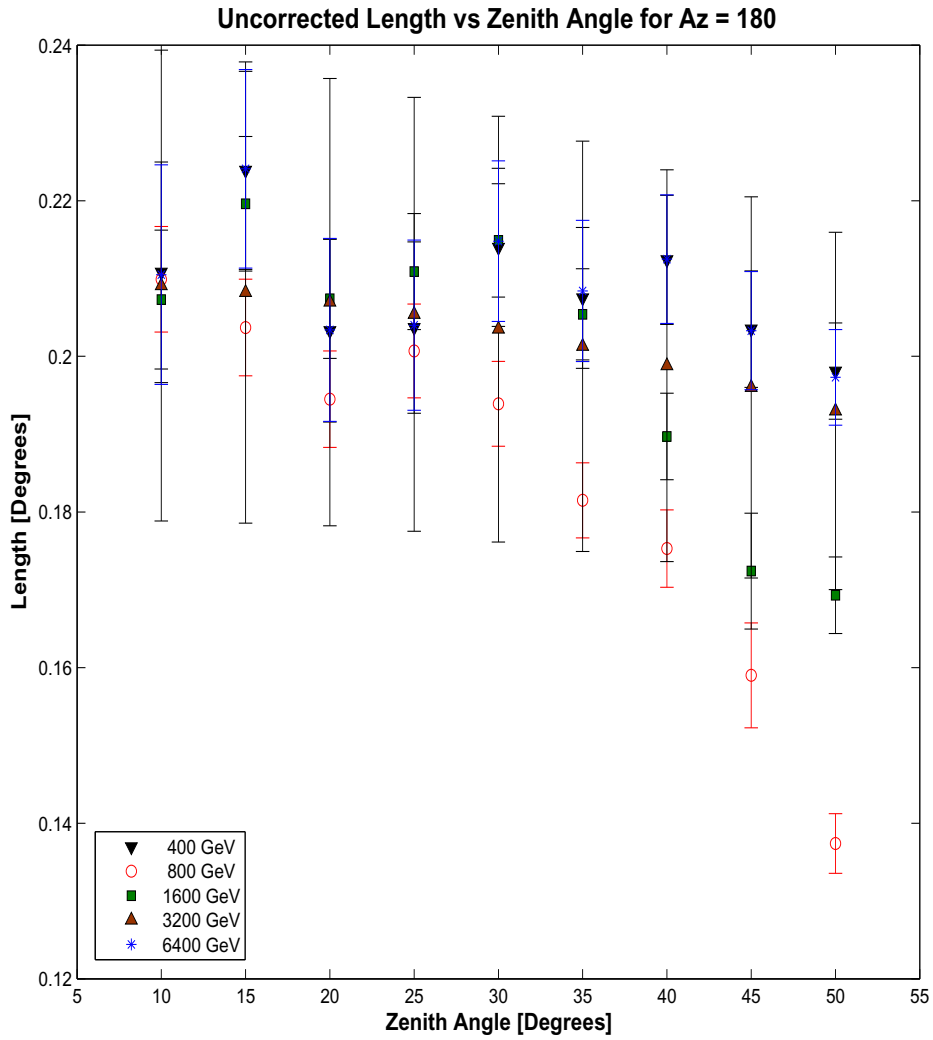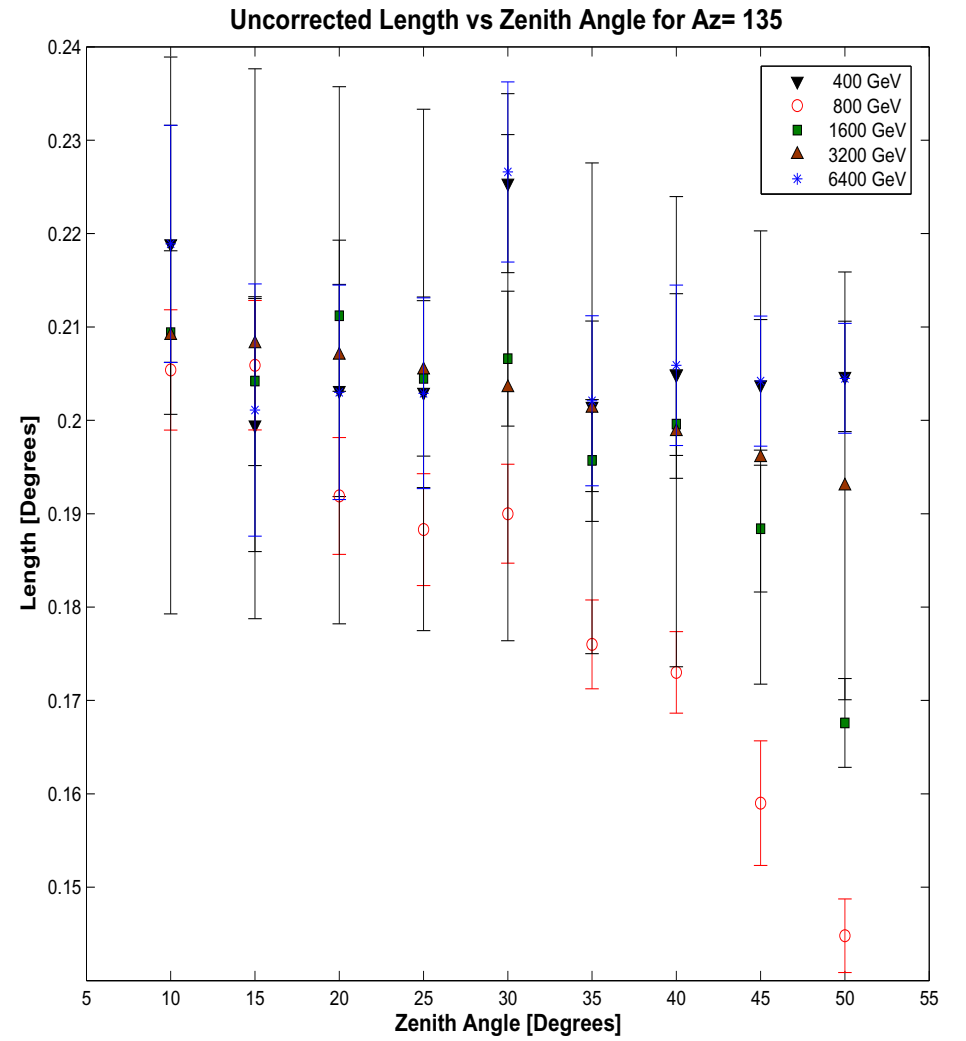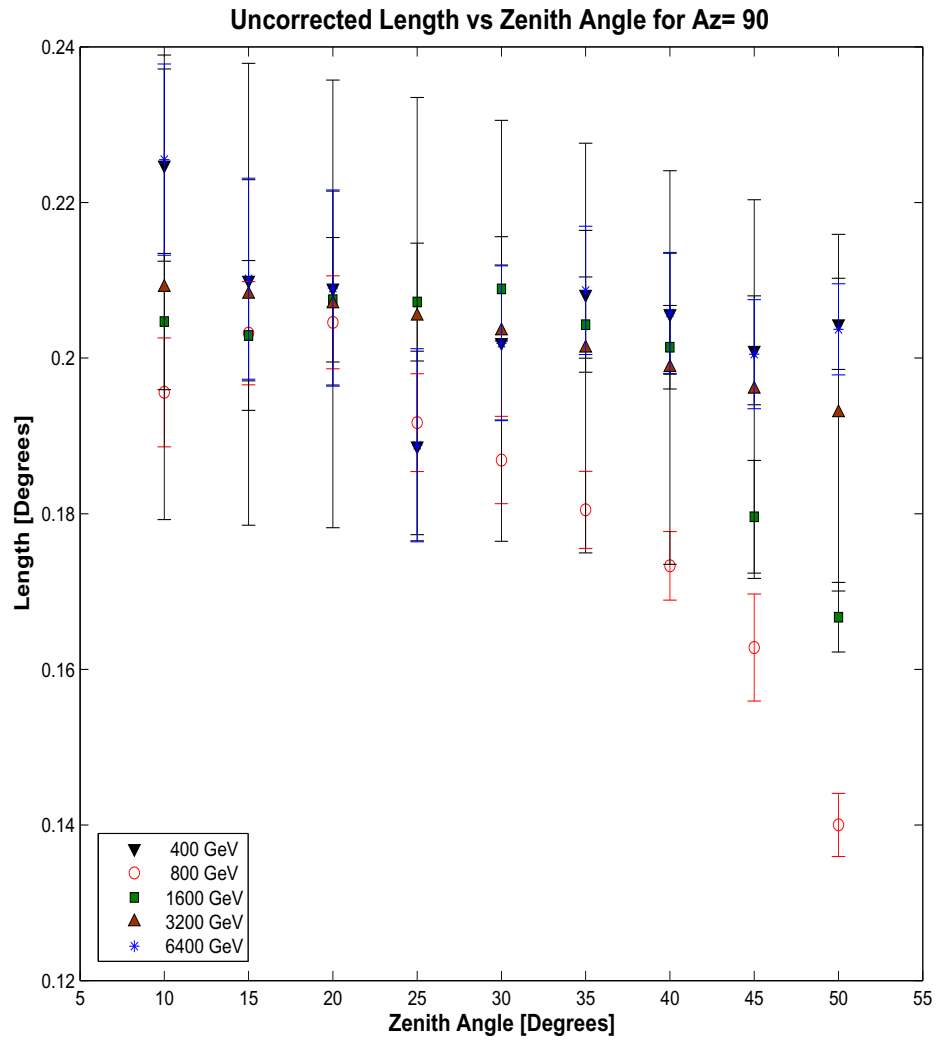
Figure 5.18: These two graphs show the changes in length as a function of zenith angle at each energy level for azimuth angles of 180° (left) and 0° (right) and with the GF present.
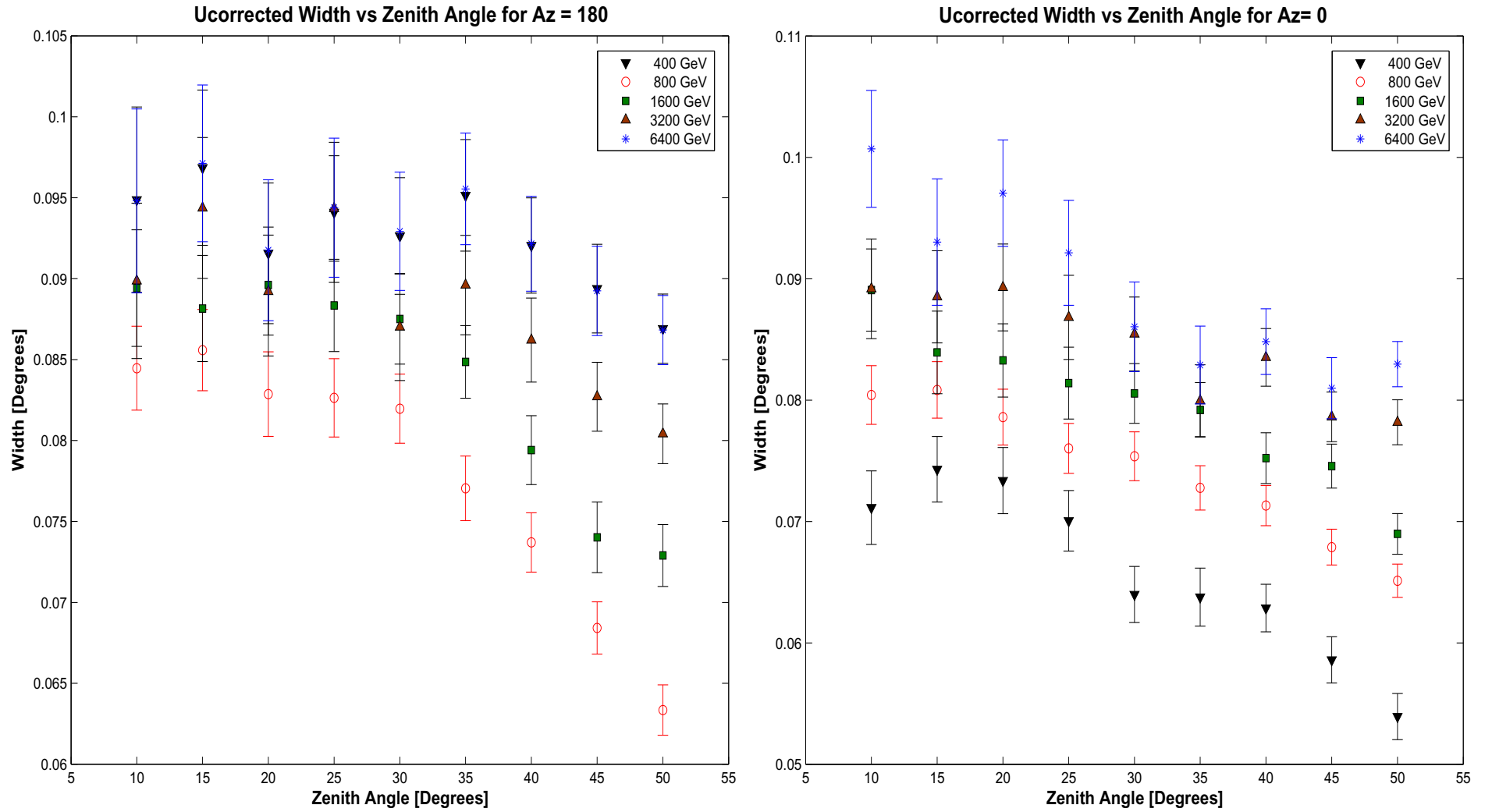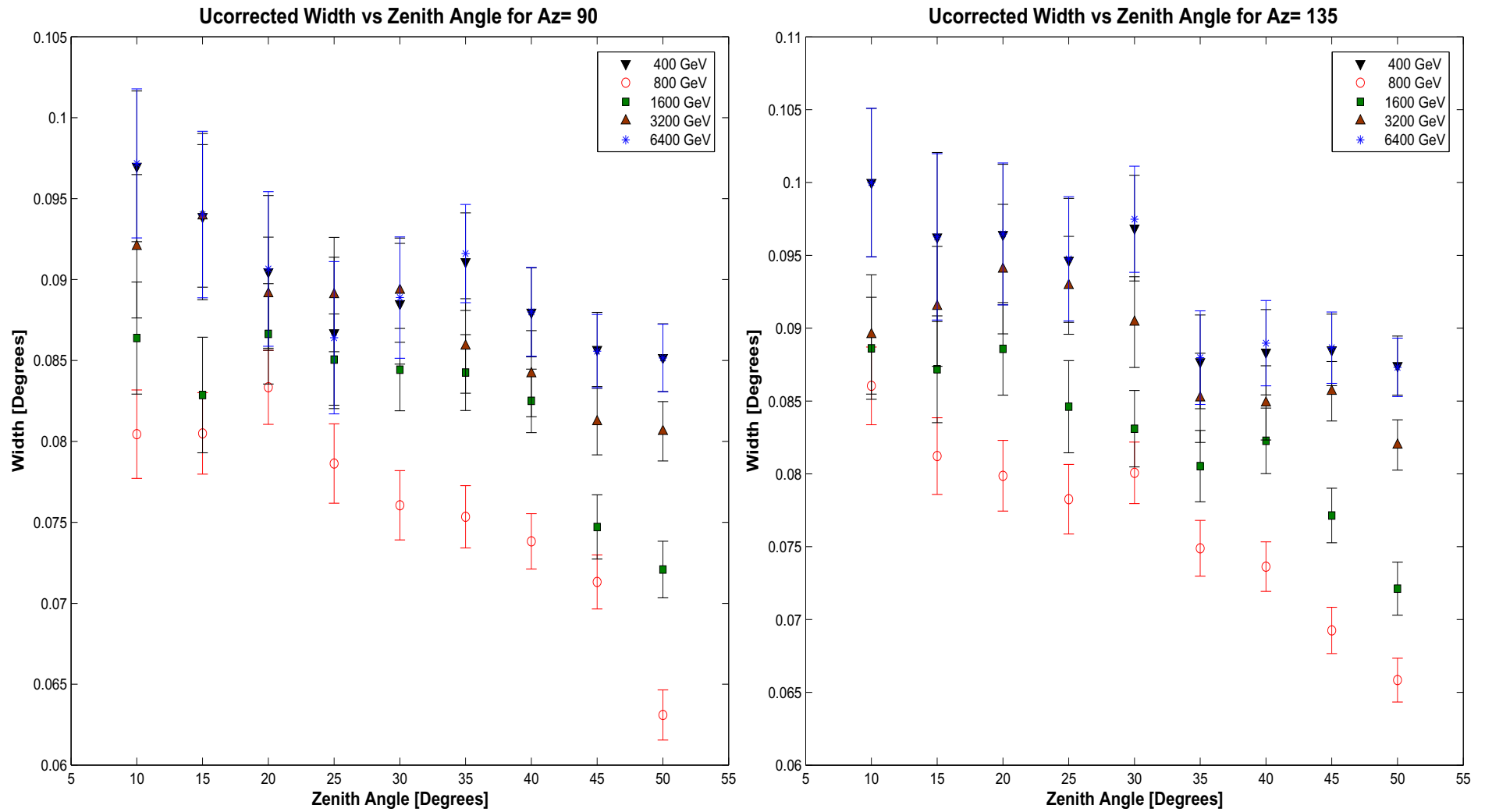
Figure 5.19: These two graphs show the changes in the width parameter as a function of zenith angle at each energy level for azimuth angles of 180° (left) and 0° (right) and with the GF present.

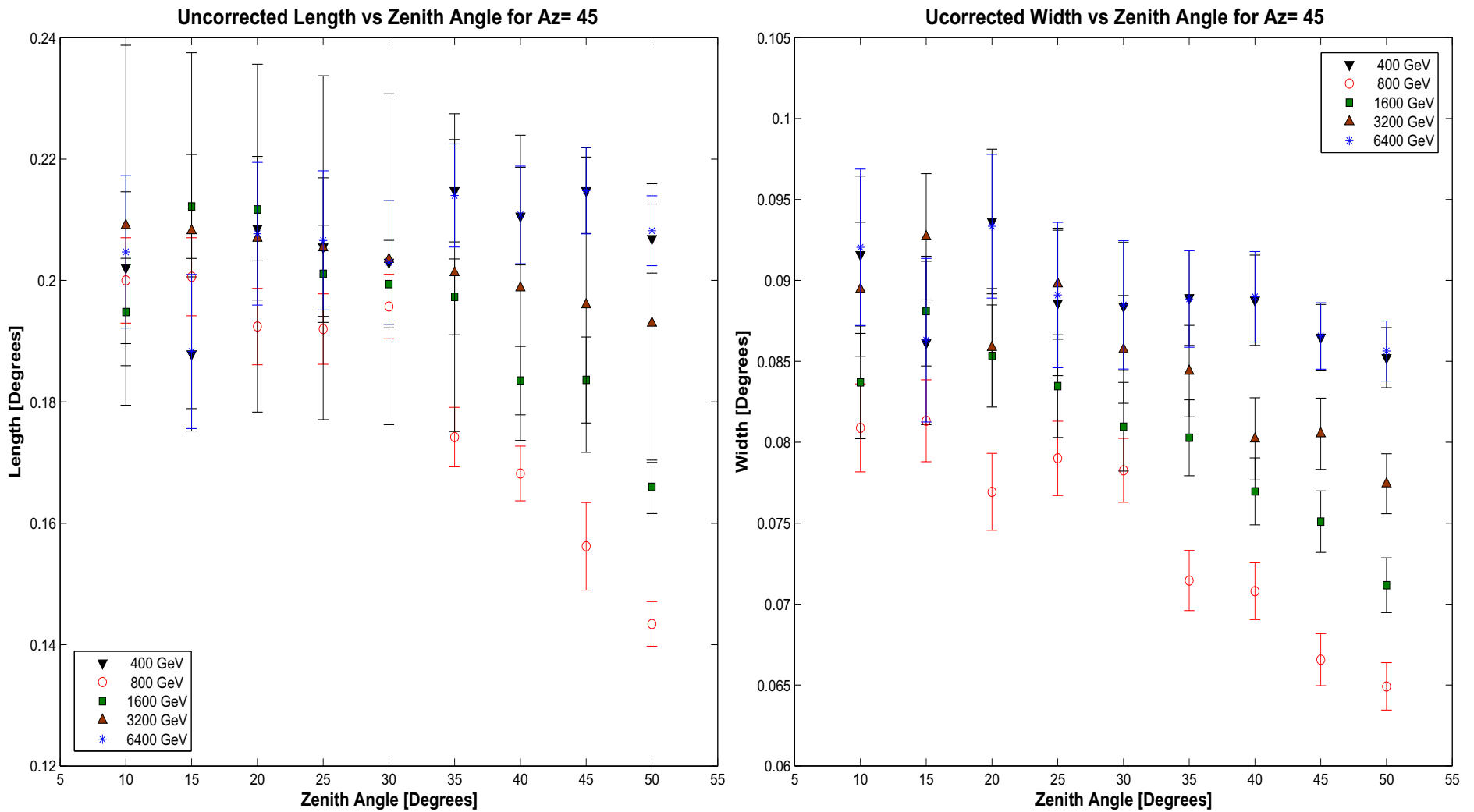**Figure 5.20**: These two graphs show the changes in length as a function of zenith angle at each energy level for azimuth angles of 90 degrees (left) and 135 degrees (right) and with the GF present.

Figure 5.21: These two graphs show the changes in width as a function of zenith angle at each energy level for azimuth angles of 90 degrees (left) and 135 degrees (right) and with the GF present .

Figure 5.22: A graph of the changes in length and width as a function of zenith angle at each energy level for azimuth angle of 45 degrees and with the GF present.

much closer to the mean. Thus we conclude that the image length and image width systematically increase as you move clockwise from south (az = 0°) to north (az = 180°) and that this is due to the GF. One can also see the geometric effect intensify at larger zenith angles. At low energies (400 GeV) this is visible only for az = 0° where the GF effect is small. For other azimuth angles in this energy range, the geometric effect is negated by the GF effect which increases the size of the length and width. For energies greater than 400 GeV, the geometric effects dominates at all energies.

In the next set of Figures 5.23 to 5.25 graphs of the ratio of width to length were made to investigate the eccentricity of the images. When we look at the min and max directions of the GF (az = 0° and az = 180° respectively) we see very different trends. We shall look at the two cases of 400 GeV and 6.4 TeV which show very distinct trends in the ratio. The ratio of the simulations for 400 GeV, with a GF and azimuth angle of zero degrees are very similar to those plots of the ratio for simulations with no GF. This is expected since at an azimuth angle of zero degrees the GF has a minimum value. However, when when we look at azimuth angle equal to 180° things are very different. The plots with a GF have a significantly higher ratio than those plots without a Gf and the trend in the graphs has changed. The steady ratio of 0.41 has been replaced by a more sinusoidal pattern for zenith angles less than 35° and the steadily increasing ratio has been replace by a constant ratio of about 0.43 for the higher zenith angles. This behavior can be explain as competing effects between the geometric effect and the GF. The geometric effect causes the image cut parameters width/length appear smaller as the EAS is initiated farther away as the zenith angle increases. While the GF causes a broadening of the image cut parameters. The GF steadily increases from zenith angle of 10° to 50°, reaching its maximum value at about 45° as seen in Figure 5.5. In the 6.4 TeV plots we see that the plots for azimuth angle = 0° match the plots with no GF with ratios being about the same for all zenith angles except for zenith angle = 10°. For the simulations of azimuth angle = 180° the ratio changes erratically so as to be sometimes bigger and sometimes smaller than the ratio for simulations with no GF. Thus indicating that he width and length parameters are affected more by the GF at lower energies.

In Figures 5.26 to 5.30 the correction function $p1 * Cos(\theta) + p0$ obtained from simulations with no GF at the various energy levels was applied to all simulations with a GF. This correction would take into account the geometric effect and correct for it in the data thus leaving us only with the GF effect. Since the percent difference for azimuth angle equal to 0° was only three percent, the correction function was not applied to this data. As we see after the correction has been applied we can still see a difference in length and width parameters for different azimuth angles but only for primary energy of 400 GeV. The percent difference now is 1.6%, 16%, 15%, 14%, 16%, for
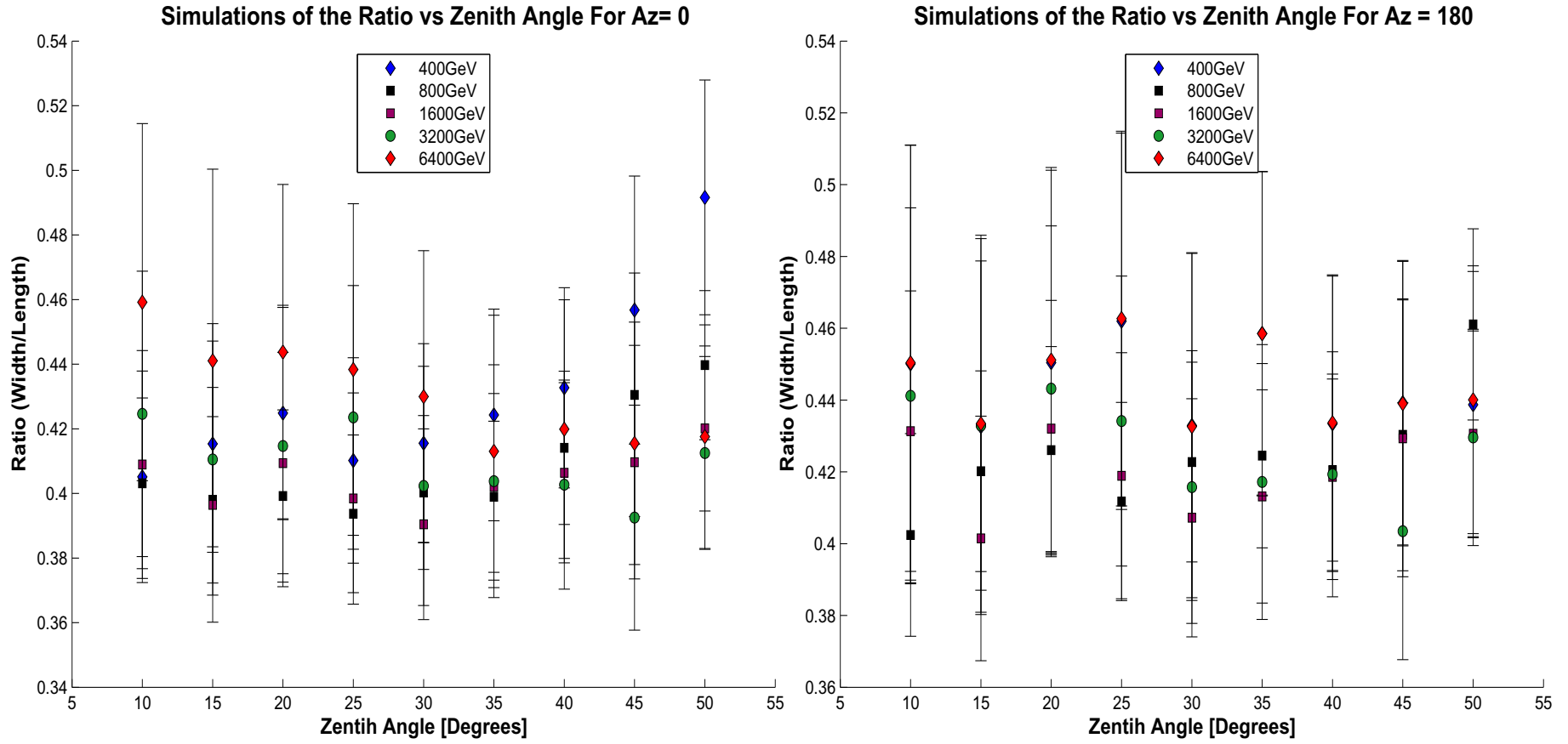
Figure 5.23: These two graphs show the ratio of the width to length for 0 degrees (left) and 180 degrees (right) for all the energy levels and with the GF present.
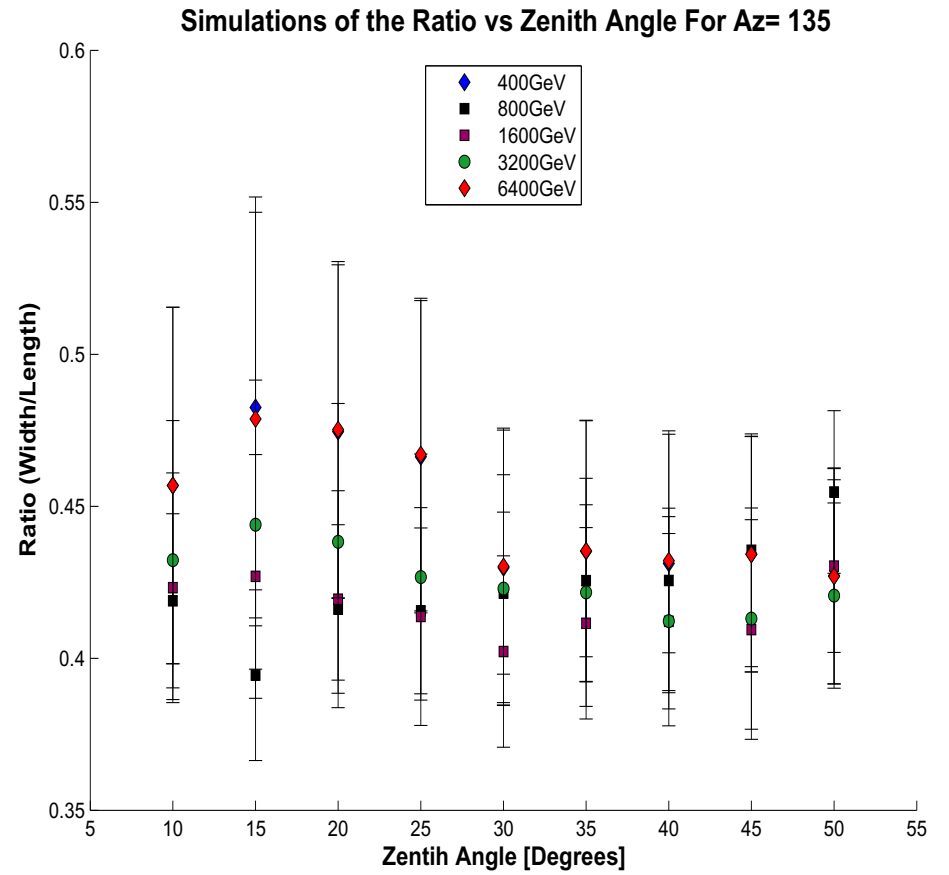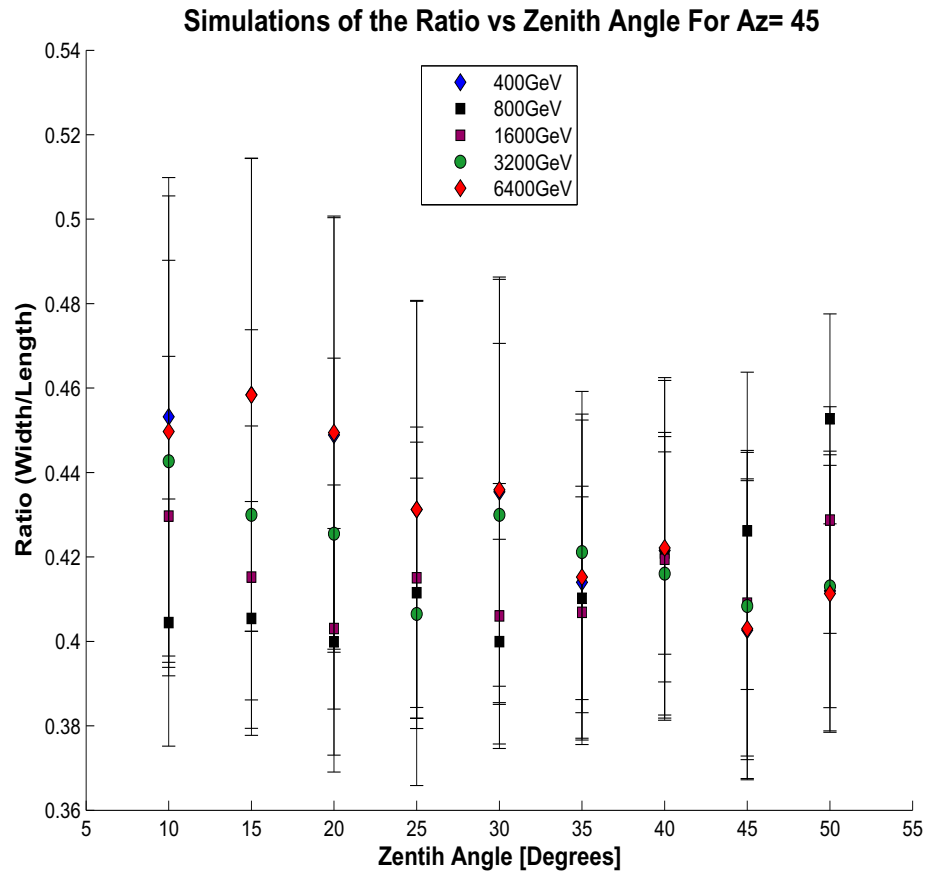
Figure 5.24: These two graphs show the ratio of the width to length for 45 degrees (left) and 135 degrees (right) for the five energy levels and with the GF present.
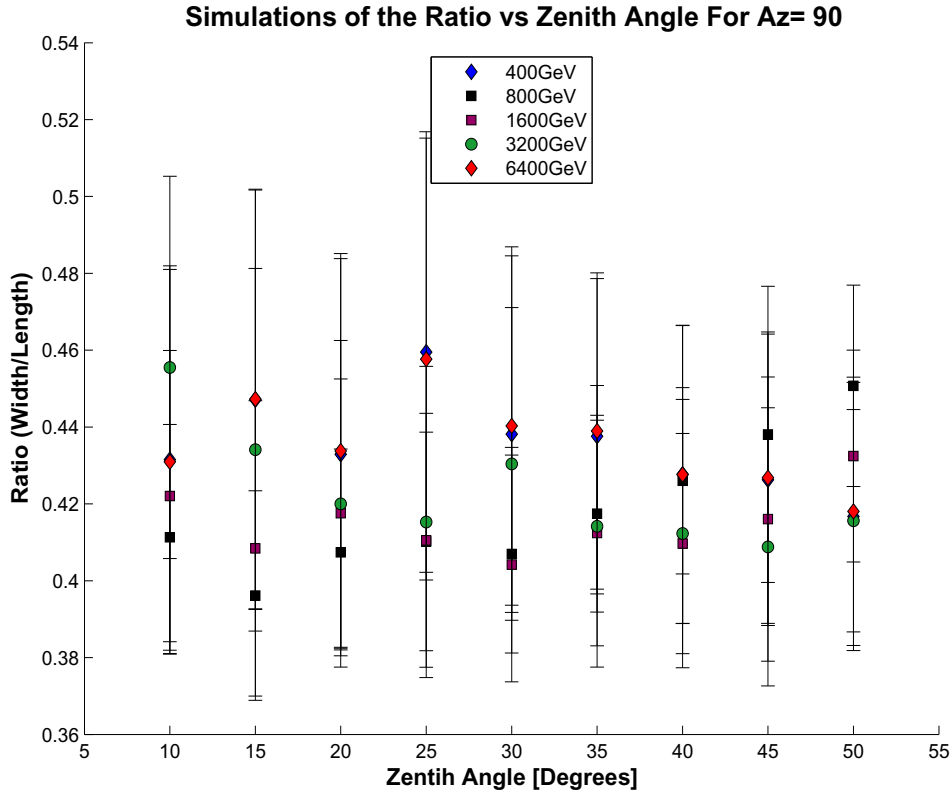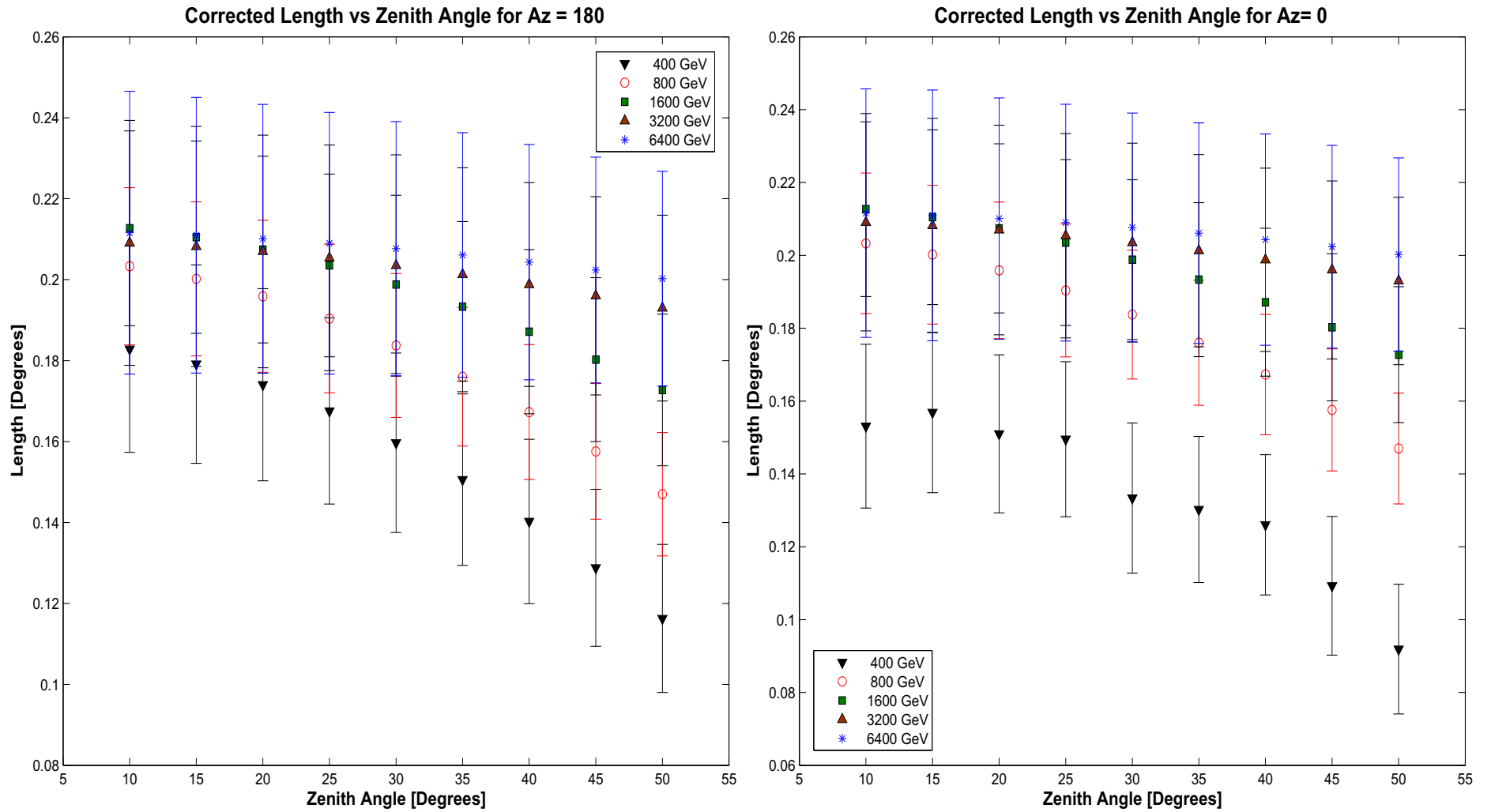
Figure 5.25: These two graphs show the ratio of the width to length for 90 for all the energy levels and with the GF present.

azimuth angles equal to 0°, 45°, 90°, 135° and 180°, similarly for the length. Thus we conclude that the GF and the geometric effect each causes the width and length parameters to change by about 15% on average over zenith angles ranging from 10° to 50° for primary energy of 400 GeV. Thus the GF effect is only significant for primary energy of 400 GeV, while the geometric effect dominates for all higher primary energy levels. These results are consisted with similar simulations carried out by [57] for the MAGIC collaboration where it was found that GF effects where significant for primary energies less than 100 GeV. It is worth mentioning that the MAGIC site has a GF that is about 20% smaller in magnitude than the GF located at the VERITAS site. Thus the GF affects on the charged particles of the EAS would be felt at lower primary energies for the MAGIC site than for the VERITAS site.

5.2.3 Observed Geomagnetic Field Effect on Crab Data

In this section we search for differences in the gamma-ray rates in the 47 quality Crab runs selected from the 2007-2008 observation season of VERITAS. Since no observations were made at

Figure 5.26: These two graphs show the changes in length as a function of zenith angle at each energy level for azimuth angles of 180 degrees (left) and 0 degrees (right) and with the correction function applied .
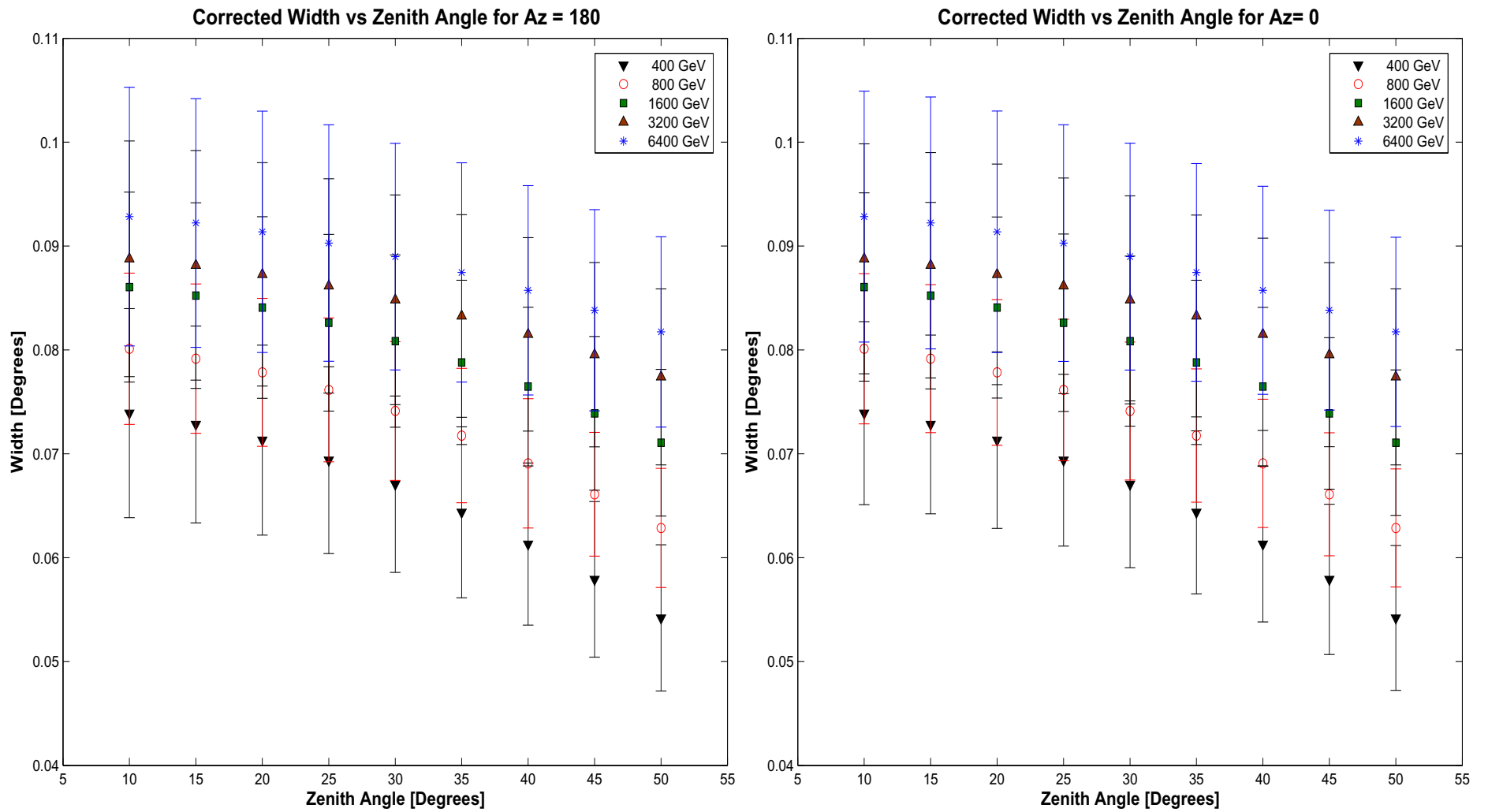
Figure 5.27: These two graphs show the changes in the width parameter as a function of zenith angle at each energy level for azimuth angles of 180 degrees (left) and 0 degrees (right) and with the GF present.

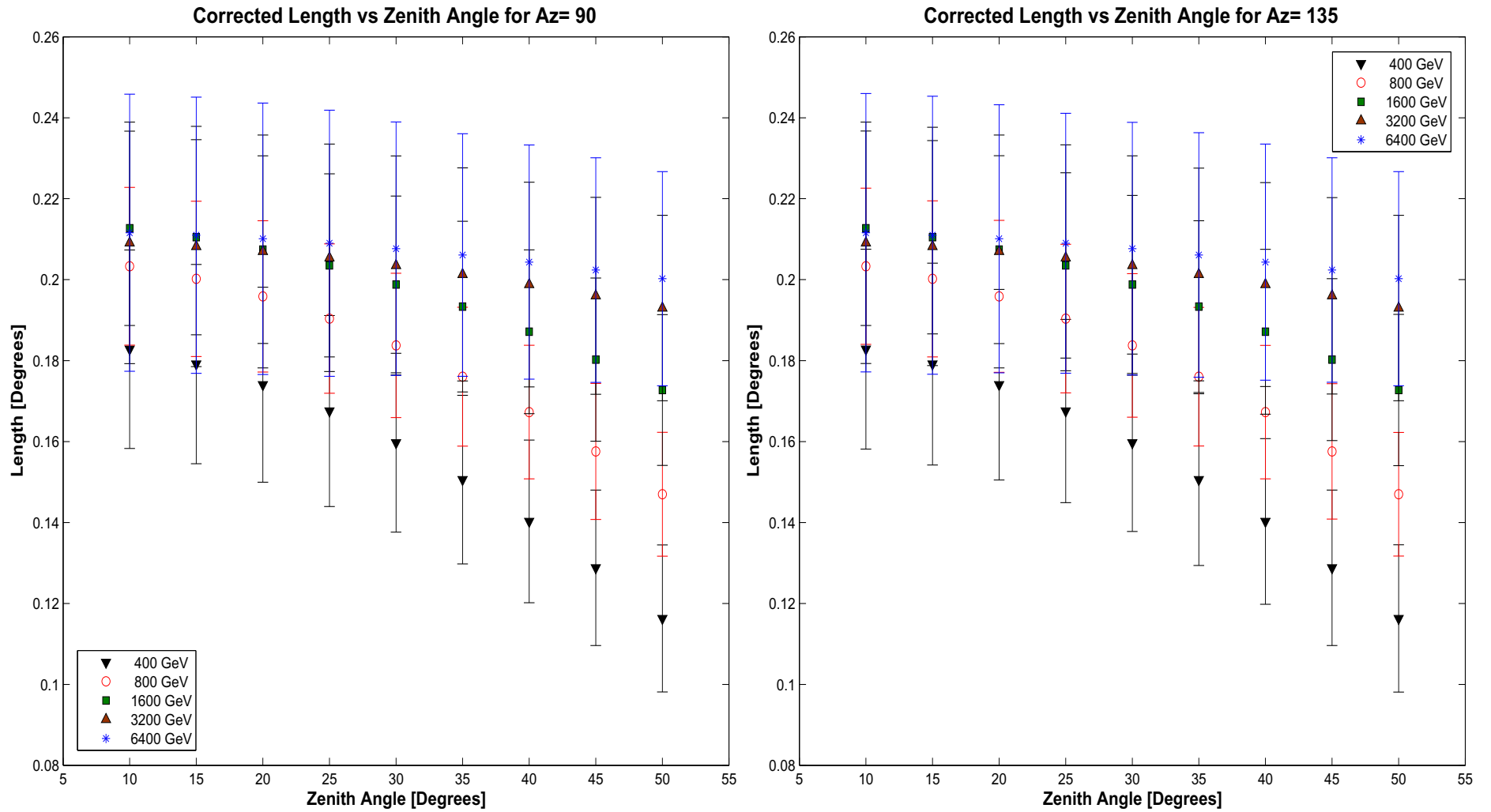**Figure 5.28**: These two graphs show the changes in length as a function of zenith angle at each energy level for azimuth angles of 90 degrees (left) and 135 degrees (right) and with the GF present.
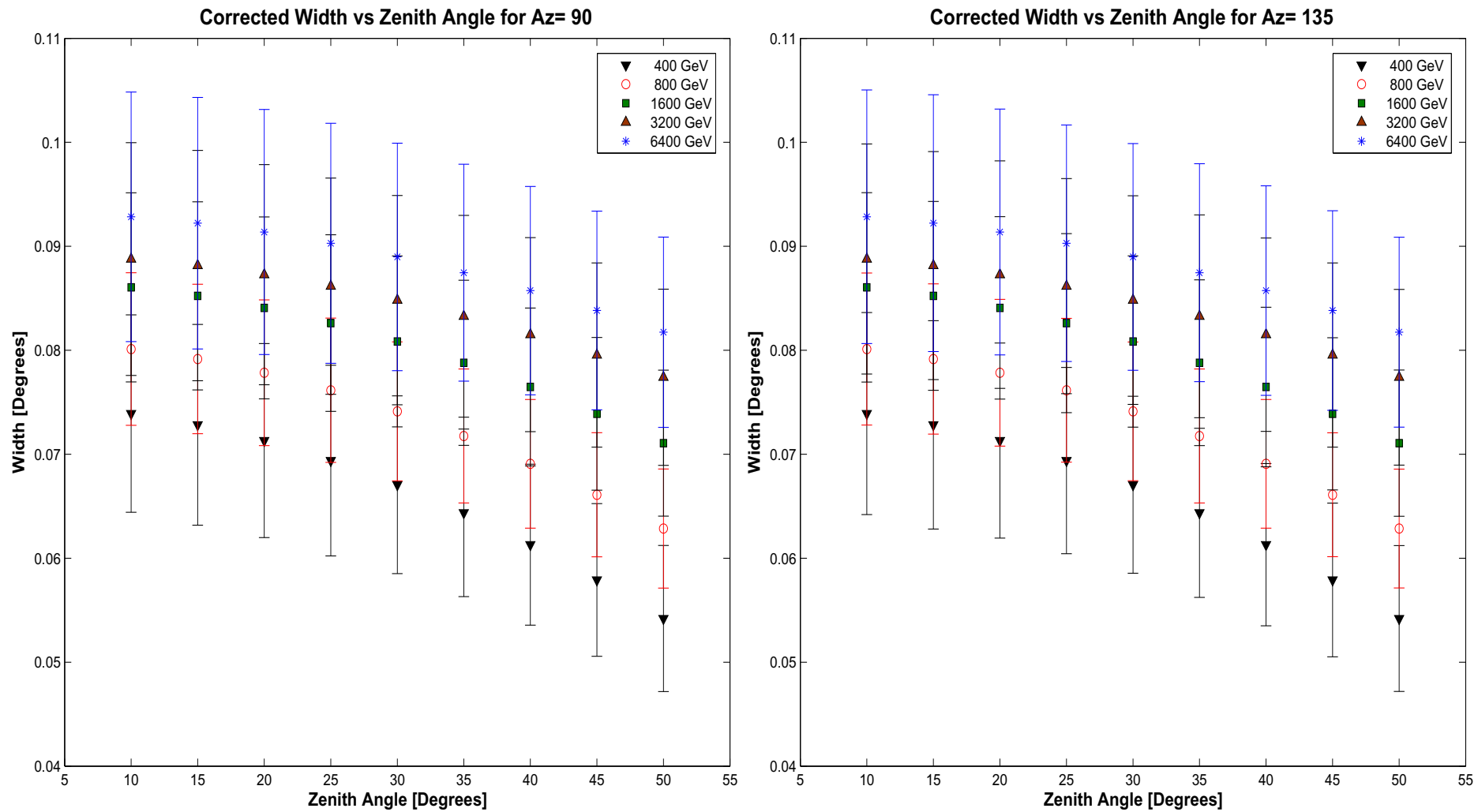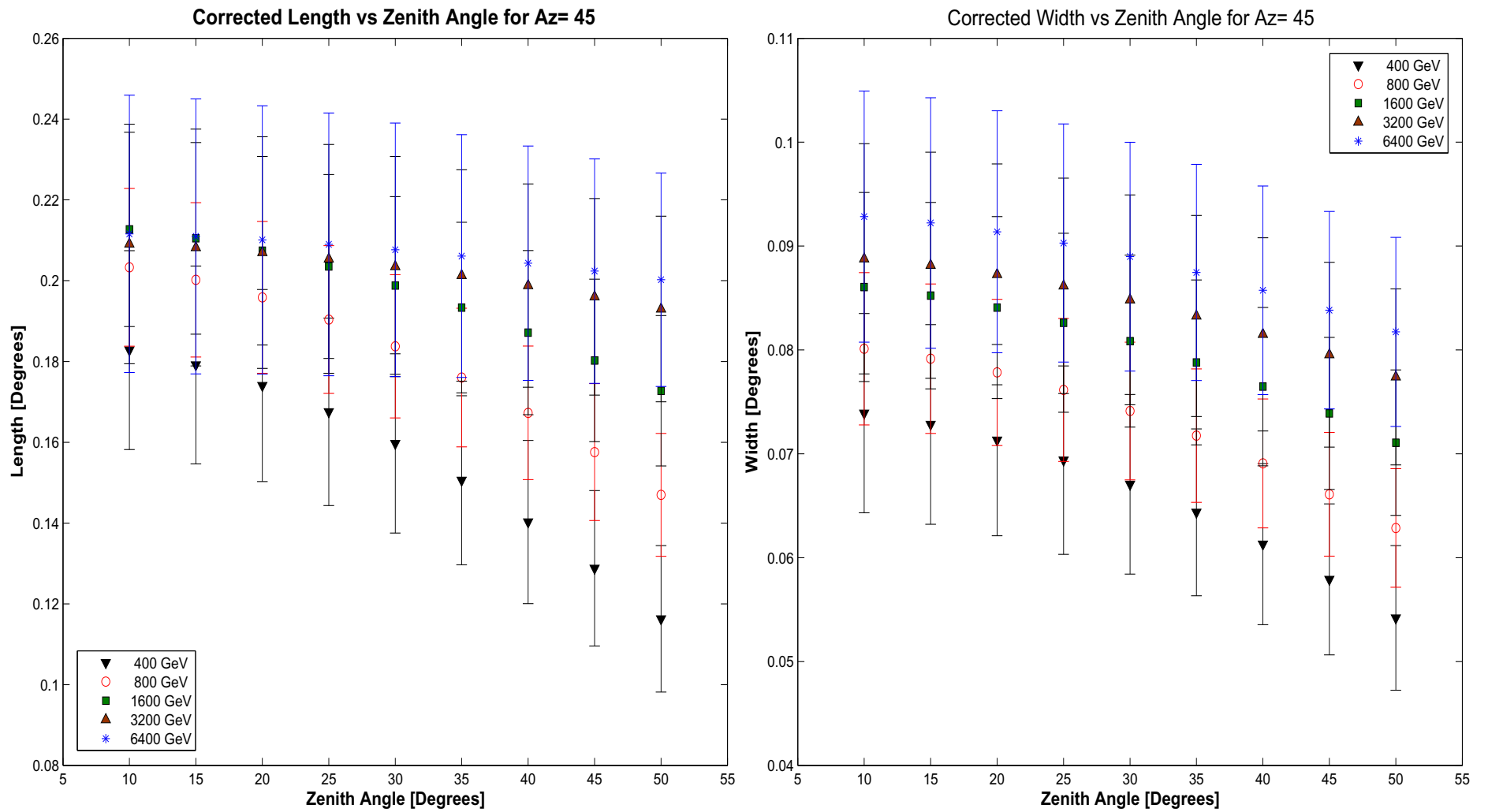
Figure 5.29: These two graphs show the changes in width as a function of zenith angle at each energy level for azimuth angles of 90 degrees (left) and 135 degrees (right) and with the GF present .

Figure 5.30: A graph of the changes in length and width as a function of zenith angle at each energy level for azimuth angle of 45 degrees and with the GF present.

the exact azimuth angles pertaining to observation directions of north, east, south and west, data was selected that is plus or minus 15° from the corresponding azimuth angle for those observation directions. Using this information Table 5.2 and Figure 5.31 were created. The first graph in Figure 5.31 shows that the highest rates are located for the south pointing direction as expected. Unfortunately, no good quality runs were found towards the north pointing direction which is expected to have the lowest rates. In this data set the lowest rates were found towards the west pointing direction (azimuth angle equal to 270°). The bottom graph of Figure 5.31 shows that the lowest rates occur where there are high values of $|\vec{B}_\perp|$. In fact the values of $|\vec{B}_\perp|$ found towards the west pointing direction are at worst 13% from the maximum value of $|\vec{B}_\perp|$. The higher values of the GF would cause a broadening of the shower which would increase the number "OFF" events and decrease the number of "ON" events and thus the gamma-ray rates would go down. Thus we conclude that high values of $|\vec{B}_\perp|$ are positively correlated with low values of gamma-ray rates for the Crab Nebula for the reasons discussed before.

As talked about above, its clear that there is a correlation between gamma-ray rates and observation direction for the Crab data set chosen. The question now is how to proceed with our analysis given the cuts on the width and length and parameters. The datareader pilot file used for the analysis of this data set was ran with the following cuts: CUTTS 1 0.16 4 325 0.04 0.115 6.5 1.8 8. 0.15. Where "$CUTTS$" defines the cuts parameters in the following order:

* mode (0: just theta2 cut, 1: standard cut, 2: spectrum cut, 3: user cut)

* theta square cuts (deg2)

* min pixel number (pxl)

* min image size (dc)

* min image width (deg)

* max image width (deg)

* min ratio p3/ntub (dc/pxl)

* min $dist_I T$/length (m/deg)

* max $dist_I T$/length (m/deg)

* radical cut of the image width (deg)

Since the simulations for the width parameter for all energies fall well within the cut values for the image min and max in the analysis we are left to conclude that although a GF effect is present it will not be detectable by our analysis. However, we do see that our cuts for the width parameter are rather large. We conclude that given our analysis of the width parameter tighter cuts can be made on the width parameter that would improve our signal to noise ratio.

Table 5.2: This table has Crab data for the four pointing directions plus or minus 15° since observations at those exact azimuth angles corresponding to the four pointing directions were not taken.

Pointing Direction	Zenith Angle [Degrees]	Rate γs/min	Azimuth Angle [Degrees]	$|\vec{B}_\perp|$ μT
East	47.6	2.7	93	39.4
East	27.3	6.2	76	27.5
East	25.3	7.8	75	26.6
South	10	6.1	12	17.8
South	10	6.5	12	17.8
South	10	7.7	13	17.8
South	9.4	5.9	8	18.1
South	9.6	7.5	345	18.2
South	10.2	6.8	359	17.4
South	9.8	7.5	358	17.7
West	58.7	0.52	263	43.6
West	62.5	0.87	260	44.9
West	50.2	1.6	266	40.5
West	51.3	1.3	266	40.9
West	60.4	0.94	261	44.3
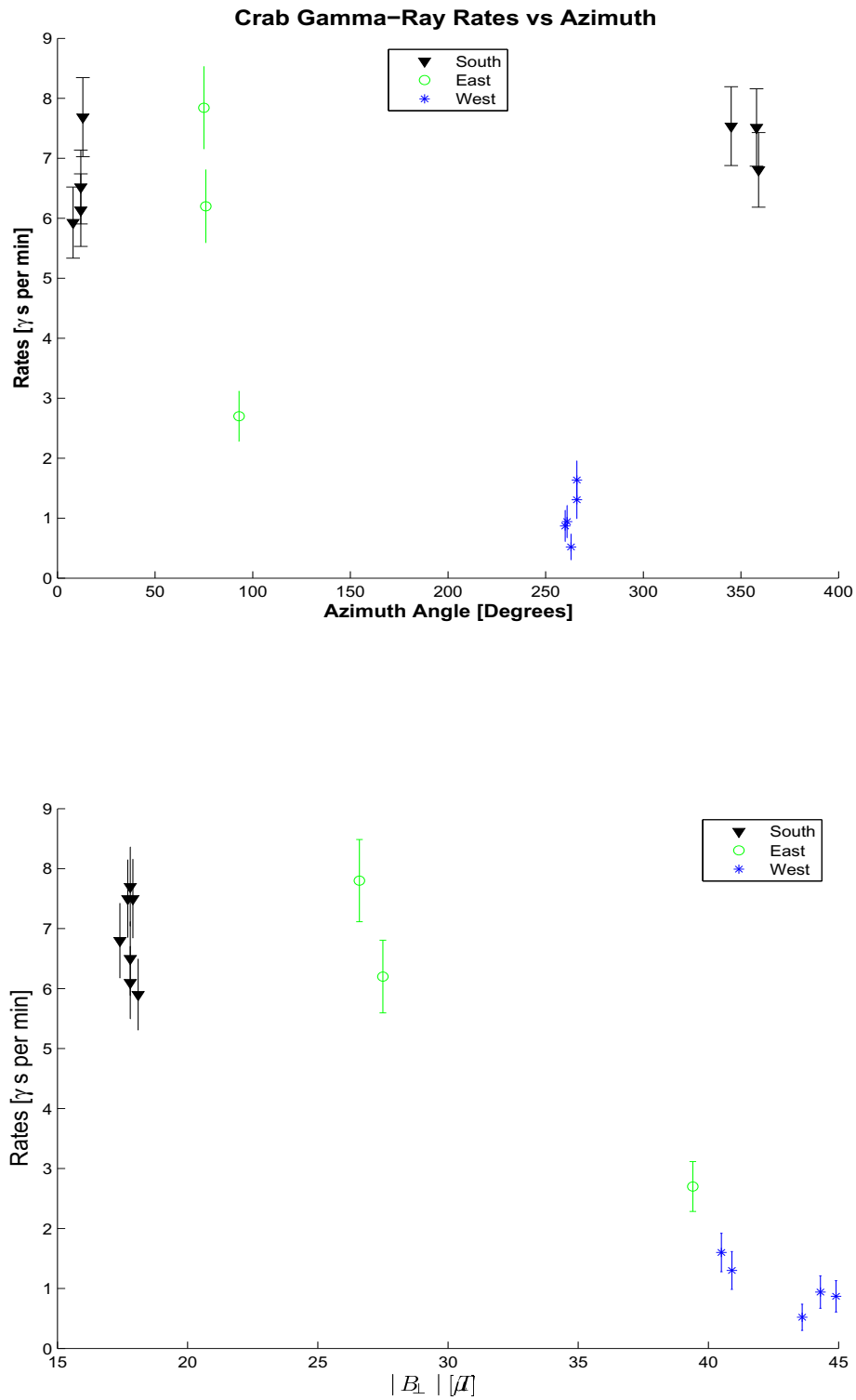
Figure 5.31: The first graph of gamma-ray rates vs azimuth angles shows how the rates depend on observation direction. As shown observations made towards the south result in the highest rates, while observations made towards west result in the lowest rates for this data set. The bottom graph of gamma-ray rates vs $|\vec{B}_\perp|$ shows that there is a positive correlation between low $|\vec{B}_\perp|$ values and high gamma-ray rates and vice versa.

REFERENCES

[1] V. F. Hess. Physikalische Zeitschrift vol 13 pgs 1084-1091, 1913.

[2] M.S. Longair. *High Energy Astrophysics: Volume 1 Particles, photons and their detection.* Cambridge University Press, 2 edition.

[3] J. Blumer, R. Engel, and J. R. Horandel. *arXiv:0904.0725v1 [astro-ph.HE]*, (2009).

[4] The Pierre Auger Collaboration. Science 9 November 2007: 938-943.

[5] R. U. Abbasi et al. ApJ 10 April 2010 713 L64.

[6] D. Ringo. *http : //upload.wikimedia.org/wikipedia/commons/8/8a/electromagnetic − spectrum.png.*

[7] H. Deirdre. PhD thesis ,The University of Leeds School of Physics and Astronomy, 2001.

[8] Buckley et al. arXiv:0810.0444 (astro-ph), 2008.

[9] T. Padmanabhan. *Theoretical Astrophysics volume 1: Astrophysical Processes.* Cambridge University Press, 2000.

[10] A.M. Hillas. J. Phys. G: Nucl. Part. Phys., 2005.

[11] B.J.Williams. *PhD thesis ,North Carolina State University*, 2010.

[12] V Bosch-Ramon. arXiv:1008.0561v1 [astro-ph.HE], 2010.

[13] R. Wagner. *http : //www.mpp.mpg.de/ rwagner/sources/.*

[14] C.J. Ryan. PhD thesis ,York University University, 2009.

[15] Ackermann et al. arXiv:1005.2141v1 [astro-ph.HE], 2010.

[16] B. D. Metzger et al. arXiv:1012.0001v2 [astro-ph.HE], 2011.

[17] J. Kildea. PhD thesis , University College Dublin, 2002.

[18] J.V. Jelley. *Cerenkov Radiation and its Applications.* Pergamon Press LTD., 1958.

[19] J.V. Jelley. *Br. J. Appl. Phys.*, **6**:227, 1955.

[20] T.C. Weekes. *Very High Energy Gamma Ray Astronomy.* Institute of Physics Publishing LTD., 2003.

[21] K. Bernlöhr. *arXiv:astro-ph/9908093v1 [astro-ph.HE]*, 1999.

[22] K. Takahashi, Y. Matsumi, and M. Kawasaki. *arXiv:astro-ph/9908093v1,[astro-ph.HE]*, 1999.

[23] A.M. Hillas. In *Proc. 19th (I.C.R.C.)*, Bangalore,India, 1985.

[24] Weekes et al. ApJ vol 342, 1989.

[25] A.N Otte. *arXiv:0907.4826v1 [astro-ph.IM]]*, 2009.

[26] J. Holder. Status and performance of the first VERITAS telescope. In *In Proc. 29nd I.C.R.C.*, Pune,India, 2005.

[27] J.M. Davies and E. S. Cotton. *Solar Energy Sci. Eng*, **1**:16–22, 1957.

[28] A. McCann, D. Hanna, and M. McCutcheon. An alignment system for imaging atmospheric cherenkov telescopes. In *In Proc. 31st I.C.R.C.*, Lodz,Poland, 2009.

[29] Toner et al. Bias alignment of the VERITAS telescopes. In *In Proc. 30th I.C.R.C.*, Merida,Mexico, 2007.

[30] O. Çelik. PhD thesis ,University of California Los Angeles, 2008.

[31] Weekes et al. *Astropart. Phys*, **17**:221–243, 2002.

[32] Nagai et al. Focal plane instrumentation of VERITAS. In *Proc. 30th I.C.R.C.*, Merida,Mexico, 2007.

[33] A. MacLeod. Master thesis ,McGill University, 2007.

[34] Schroedter et al. A topological trigger system for imaging atmospheric-cherenkov telescopes. In *In Proc. 31st I.C.R.C.*, Lodz,Poland, 2009.

[35] A Weinstein. The veritas trigger system. In *In Proc. 30th I.C.R.C.*, Merida,Mexico, 2007.

[36] A.W. Smith. PhD thesis ,The University of Leeds School of Physics and Astronomy, 2007.

[37] E Hays. Veritas data acquisition. In *In Proc. 30th I.C.R.C.*, Merida,Mexico, 2007.

[38] P. Cogan. PhD thesis ,University College Dublin, 2006.

[39] Crab Nebula. Encyclopaedia britannica online. *Encyclopedia Britannica, 2011.*

[40] J. Arons. arXiv:0708.1050v1 [astro-ph], 2007.

[41] VERITAS Collaboration. arXiv:1108.3797 [astro-ph.HE], 2011.

[42] L. Maxim, N. Otte, and A. McCann. arXiv:1108.3824v1 [astro-ph.HE], 2011.

[43] F.A et al Aharonian. ApJ, Vol. 614, 2004 October 20.

[44] A.A Abdo. Science, VOL 331 , February 11 2011.

[45] M. Tavani. Science, VOL 331 , February 11 2011.

[46] S. S. Komissarov and M. Lyutikov. arXiv:1011.1800v2 [astro-ph.HE], 2011.

[47] M.K. Daniel. arXiv:0709.4006v1 [astro-ph], 2007.

[48] T.P. Li and Y.Q. Ma. ApJ vol 272 pgs 317-324 , 1983.

[49] G. Concconi. *Phys. Rev*, **95**:1705, 1953.

[50] S. McLean, S. Macmillan, S. Maus, V. Lesur, A.Thomson, and D. Dater. Technical Report 1, NOAA, 2004.

[51] K.H. Glameier, S. Heinrich, and F.W. Negendank. *Geomagnetic Field Variations (Advances in Geophysical and Environmental Mechanics and Mathematics).* Berlin: Springer, 2009.

[52] C.T. Russell. *Solar wind and interplanetary magnetic field: a tutorial.* American Geophysical Union, 2001.

[53] J. Kemp. Wikipedia, The Free Encyclopedia. Wikimedia Foundation, Inc., 21 October 2010. Web. 09 Januanry 2005.

[54] W.H. Campbell. *Introduction to Geomagnetic Fields.* Cambridge University Press, 2 edition, 2003.

[55] F. Stefani, A. Gailitis, and G. Gerbeth. *ZAMM*, **88**:925, 2008.

[56] C. Duke and S.L. LeBohec. Grisu(tah) analysis package. *http://www.physics.utah.edu/gammaray/GrISU/GrISU2009September17/Documentation/,* 2010.

[57] R. Lopez. PhD thesis ,Universidad Complutense de Madrid, 2008.